CONSTRUCTION OF A PHYSICS-BASED BRAIN ATLAS AND ITS APPLICATIONS

AVIJIT ROY

B.Sc Eng. (BUET), M. Eng. (NUS)

A THESIS SUBMITTED FOR THE DEGREE OF DOCTOR OF PHILOSOPHY

DEPARTMENT OF MECHANICAL ENGINEERING
NATIONAL UNIVERSITY OF SINGAPORE
2007

ACKNOWLEDGEMENTS

I am deeply grateful to my supervisors Professor Francis Eng Hock Tay and Professor Wieslaw L. Nowinski for providing me the necessary guidance, insight, encouragement and independence to pursue a challenging project. I still remember the day when Prof. Tay, my supervisor of National University of Singapore kindly introduced me to Prof. Nowinski, the director and principal scientist of Biomedical Imaging Lab (BIL) of ASTAR three years ago. This is when I got an opportunity for the first time to know about *Cerefy* Brain atlas, the famous product of BIL, and arguably one of the best existing atlases in the world. I was overwhelmed, and later decided to incorporate the atlas in my research. Not only this, in spite of his busy schedule, Prof. Nowinski has always been eager to listen and solve any kind of problem related to my project and gave a proper direction. He also gave me his kind permission to use all his lab facilities as a research student of BIL for the successful accomplishment of the project. Prof. Francis Tay, on the other hand, made a parallel track of my work though the weekly meetings and by giving unbounded guidance, advice and counsel in the course of my research project. In fact their contributions to this work were so vital that they cannot be described here in words.

I am also especially grateful to Thirunavuukarasuu, my colleague of BIL for the encouragement and technical support and fruitful discussion about the project. Thanks to Zhang Yanzhong of Biomechanics Lab of Bioengineering department of NUS for setting up the test facility for my experimental work on porcine brain. Thanks to Su Huang, Chunping, Jimin, Weili other friends and colleagues of BIL and NUS who are directly or indirectly involved to make the project successful.

I would like to express my special thanks to Bonna for inspiring me from USA to devote myself in studies and research work. I would also like to extend my deepest gratitude to my parents for their complete moral support.

TABLE OF CONTENTS

SUMMARY

The human brain is a most complex, multifunctional system that serves as the primary physical interaction between the body and the environment and directs an organism's behavior and actions. Even though the brain has been widely studied for centuries by various groups such as anatomists, physiologists, biochemists, geneticists, surgeons, neurologists, psychologists, human brain mappers, bioengineers and many others, no physics-based atlas is constructed yet. As the interest in the computer-aided, quantitative analysis of medical image data is growing, the need for accurate modeling techniques of brain is also increasing. Today the finite element method (FEM) provides a powerful tool for investigating the biomechanics of brain deformation particularly when used in conjunction with experimental studies. In this dissertation a finite element biomechanical modeling approach has been proposed to build a physics-based atlas of the human brain from an anatomical brain atlas called *Cerefy*.

All the attempts for developing various types of atlas in the past were based on capturing anatomy, function, and vasculature. There was not any significant attempt to build any physics-based 3D human brain model on any atlas. For the first time based on hyperviscoelastic polynomial strain energy density function a complete 3D *physics-based atlas* (PBA) has been developed that contains fully meshed 43 major anatomical structures and brain connections. This is the original contribution compared to other previous research in the current field. The novelty of the work over the other existing model has been described. The proposed model has shown the ability to simulate the deformation for the whole brain as well as individual sub-cortical structures during neurosurgical procedures (the strain rate between $0.001s^{-1} – 1.0s^{-1}$). The limiting stress relaxation for infinitesimally small loading has also been obtained (the shear modulus

reaching 194.62 Pa) exhibiting similarity with a hydrocephalic condition. In addition, a macroscopic, primary brain tumor growth is simulated incorporating the biological and biochemical factors that affect the meshed model.

To facilitate model validation, an in-vitro indentation experiment on porcine brains was conducted using the facility in Biomechanics Lab of National University of Singapore (NUS), in accordance with ethical guidelines on animal experiments. The experimental result suggests brain tissue accounts for strong nonlinear stress-strain relationship and the hyper viscoelastic FEM modeling approach was best suited for such analysis. The predication from the meshed model and experimental results also agree well. The model was also validated by geometric matching 2D cross sections with axial atlas images, studying mesh convergence and estimating nodal error. This atlas has a potential to predict brain deformation in surgical loading and in future may be well-incorporated into image-guided or computer-assisted surgery. Its other potential benefits include increased accuracy of modeling, visualization and surgical simulation, intraoperative computations, patient specific operation planning or prognosis of various diseases like hydrocephalus or tumor growth. This atlas can also be incorporated in various education or training program.

This dissertation also introduces a framework of a Meshed Atlas Visualization Toolkit (MAVT), an automated mesh generator that can construct the virtual anatomy model and visualize the meshed model in a Java platform. In addition to generating automated mesh using atlas data, the toolkit's added benefit lies in facilitating successful collaboration between geographically dispersed CAD users. The toolkit can be used for medical study, simulation purposes and in other virtual reality applications.

LIST OF FIGURES

LIST OF TABLES

LIST OF ABBREVIATIONS

S/N	ABBREVIATION	TERMS
1.	CT	Computed Tomography
2.	MRI	Magnetic Resonance Imaging
3.	3D	Three Dimensional
4.	2D	Two Dimensional
5.	1D	One Dimensional
6.	FE	Finite Element
7.	FEM	Finite Element Method
8.	FEA	Finite Element Analysis
9.	PDE	Partial Differential Equation
10.	MAVT	Meshed-Atlas Visualization Toolkit
11.	VDS	Virtual Design Studio
12.	OO	Objected-oriented
13.	OOP	Object-oriented Programming
14.	XML	Extended Markup Language
13.	HTML	Hypertext Markup Language
14.	TT	Talairach- Tournoux (brain atlas)
15.	SW	Schaltenbrand–Wahren (brain atlas)
16.	CSF	Cerebrospinal fluid
17.	CAD	Computer Aided Design
18.	CAM	Computer Aided Manufacturing
19.	CAS	Computer Assisted Surgery
20.	CASP	Computer Assisted Surgery Planning
21.	DBS	Deep brain Stimulation
22.	VB	Visual Basic
23	VR	Virtual Reality
24	PB	Physics-based / Physically based
25.	PBA	Physics-based Atlas

Chapter 1

INTRODUCTION

1.1 Background

Brain atlas can be an invaluable source of finite element models of the human structure. However, this rich resource is grossly overlooked especially in realistic physics-based modeling of human brain. Even though the usefulness of various atlases is gaining a great deal of attention each and every day especially in medical imaging, which is significant in several applications, including computational anatomy, functional image analysis, image-guided neurosurgery, and model-enhanced neuroradiology as well as in biomechanics, not very significant effort has been observed to build any physics-based model using atlas data. Numerous types of brain atlases have been developed in last fifty years to fulfill various needs; the formats include MRI-based, cryosection-based, Visible Human derived, surface-based, and probabilistic (surface-based, anatomical, and functional), in addition to the stereotactic printed atlases and their electronic versions. However, most of these atlases rely on capturing *anatomy* (Talairach and Tournoux et al, 1993; Nowinski et al, 1998a, 1998b), *function* (Nowinski et al, 2001a, Nowinski et al, 2003c), and *vasculature* (Szikla et al., 1977; Nowinski et al, 2005) etc., whereas the growing need and demand for a physics-based atlas (PBA)[1] has always been ignored (Roy et al, 2006a). The reason might be overemphasis on 'patient specific' solution and for having various

[1] Physics-based modeling, commonly called physically based modeling, employs laws of Physics to construct models. Physics-based Atlas (PBA) is a biomechanical 3D model constructed from Atlas data which leads to physically realistic simulation and animation.

uncertainties in brain biomechanics (in terms of proper identification of structures, material properties and boundary conditions etc) to obtain a more generic solution. However, recent advancement in brain-biomechanics, bioengineering, image analysis and particularly information technology, has paved the way for the researchers to acquire more knowledge and unveil various 'uncertainties' and 'mysteries' which was not possible to resolve in last couple of decades. Moreover, Finite element Method (FEM) has emerged as a very powerful computational method, which makes it obligatory to incorporate various physics-based (PB) techniques in anatomical discipline to build a complete 3D meshed model. In this project, an electronic brain atlas known as *Cerefy* Brain Atlas (Nowinski et al, 1997, 1998, 2001b, 2000c, 2002a, 2004) has been selected for the construction of a 3D human brain model for the investigation of biomechanics of the brain. The atlas has three major components: image data, anatomical index, and supporting tools. It is derived from four classic stereotactic printed brain atlases (Schaltenbrand and Wahren, 1977; Talairach and Tournoux, 1988; Ono et al, 1990; Talairach and Tournoux, 1993). The *Cerefy* electronic brain atlas database is now the standard in stereotactic and functional neurosurgery, and has already been adopted by several companies, hospitals and research centers specializing in image-guided surgery. This justifies the choice for using it as a prime source of anatomical and geometrical information for the model development. The other important factors that influenced us to choose this particular atlas were its use in clinical, research and educational practice.

The Physics-based FEM brain atlas model has been developed based on the assumption of large deformation of non-linear hyperviscoelastic material with quasi-static behavior (Roy et al, 2004a, 2004b, 2005b, 2006a; Miller, 2002a). A nearly

incompressible material behavior is assumed for the brain tissue as the bulk modulus of the brain was found million folds higher than the shear modulus. 10-node parabolic (quadratic) elements are used in tetrahedral mesh generation as they yield better mathematical approximations and better-curved boundaries compared to linear ones. The developed multistructured nonlinear 3D meshed model have advantages over other existing sigle phase homogeneous models using elastic (Bajcsy, 1989; Ferrant et al, 1999, Kyriacou, 1999), poroelastic (Miga, 2000, Paulsen 1999), viscoelastic (Miller, 1999, Mendis, 1995) and viscous fluid deformation models (Christensen, 1996; Bro-Nielsen, 1996).

The investigation of the material properties of the brain to construct an accurate PB model for deformation analysis is very crucial. An in-vitro indentation experiment was conducted on five porcine brains utilizing the facility of Biomechanics Lab in National University of Singapore (NUS). Such experiments with soft tissue are also helpful to validate the developed meshed atlas (PBA) and its underlying assumptions. The experimental result suggests brain tissue accounts for strong nonlinear stress-strain relationship and choice of hyper viscoelastic material in FEM was well-justified. The experimental results are compared with the recent research work of other researchers and discussed. The model is also validated by geometric matching 2D cross sections with axial atlas images, studying mesh convergence and estimating nodal error.

To illustrate the usefulness of the PBA, two specific biomechanical situations (specifying constitutive laws and boundary conditions) are simulated. In the first situation, the brain tissue behavior was studied due to the forces acting on the top of the brain by surgical tools. The brain is assumed to be submerged in cerebrospinal

fluid and the bottom part of the brain did not move during surgery. The proposed model has shown the possibility to simulate the deformation for the whole brain as well as individual sub-cortical structures during neurosurgical procedures (strain rate between $0.001s^{-1}$ – $1.0s^{-1}$). The limiting stress relaxation for infinitesimally small loading has also been obtained (shear modulus reaching 194.62 Pa). In the second situation, a macroscopic, primary brain tumor growth is simulated incorporating the biological and biochemical factors that affect the meshed model. The 3D model of the tumor from segmented pathological data is constructed and the deformation due to pore pressure distribution within the brain is calculated.

Mesh generation has always been a challenging issue in biomechanical models since there is high variability and uncertainty in human anatomies; thus, mesh generation has to be handled with proper care. In addition, the human brain has many intricate and complicated morphological details that need collaboration in designing and modeling to a great extent. A framework of an automated mesh generator, MAVT (Meshed Atlas Visualization Toolkit) has been illustrated that can successfully construct the virtual anatomy model and visualize the meshed model. The toolkit has been developed using JAVA™ and its 3D API JAVA3D™, thus its platform independency and object oriented features enable it to work in hybrid and dynamics research and educational environments. The design and implementation of MAVT emphasize the reusability and flexibility for 3D visualization and interactive simulation. The scope of the tool has also been expanded to develop a collaborative CAD environment through a virtual design studio (VDS) that facilitates synchronous dynamic collaboration between geographically dispersed users. By the synchronous CAD collaboration through VDS, it is possible to distribute the entire design work to various users depending upon their

domain knowledge. This is a sharp advancement over the automatic or semi automatic mesh generation software packages provided by Ferrant et al. (2000), Miga et al. (1998), and Hartmann and Kruggel (1999) or even other existing professional meshing (FEM) software. The presented concept is expected to provide a new insight in clinical applications, research, training and educational practices.

1.2 Scope and Motivation of Research

Mechanical properties of soft and living tissues form a central subject in Biomechanics for centuries. In particular, the properties of the muscular-skeletal system, skin, lungs, kidney, liver, brain, blood and blood vessels have attracted much attention recently. However, to the best of our knowledge, in spite of various researches in medical imaging and bioengineering, currently *no 3D meshed Atlas*[2] is available on detailed anatomy and structures. Many researchers (such as Ruan et al, 1994b; King et al, 1995; Zhou et al, 1996; Mendis et al, 1995; Al-Bsharat et al, 1999; Brands et al, 2004; Horgan and Gilchrist, 2003, 2004) constructed physics based model, but their models required investigation of a very fast strain rate, as their primary focus was not neurosurgical procedure but solely impact. Moreover their model had very few subcortical structures and not constructed from any atlas data. Thus, the main

[2] A notable exception is WSUBIM (Wayne State University Brain Injury Model). Starting from late 80's, it has offered several versions (such as ver. 1993, ver. 1995, ver. 2001) and has been in continuous improvement. However, the model till date has meshed only few subcortical structures (the grey matter, the white matter, the brainstem, the CSF and the ventricles) inside the brain. Moreover, the model was not built from any of the existing atlas data and the main purpose of their research was motivated by modeling traumatic brain injury only, and hence its brain materials considered strain-rates larger than those appropriate for other applications such as modeling surgery, hydrocephalus or tumor growth etc.

motivation of this work is to develop a complete meshed atlas (physics-based atlas) showing detailed anatomy of the brain.

The modeling of deformable soft tissue is, in particular, of great interest for a wide range of medical imaging and bioengineering applications, where the realistic interaction with virtual objects is required. Especially, computer assisted surgery (CAS) applications demand the physically realistic modeling of complex tissue biomechanics. Previous research on the mechanical properties of the brain and brain tissue was motivated by traumatic injury prevention, e.g. automotive accident etc. which require investigation of very fast strain rate. Very less effort has been provided for closer examination of mechanical properties of brain tissue at moderate and low strain rates which are relevant to surgical procedures. The goal of the present thesis is to develop a biomechanical model of brain tissue tailored to the particular needs of surgery planning and simulation research that can model and simulate deformable materials for application requiring real-time interaction. To build such a physically-based deformable model, the following steps are followed:

1. Identify major anatomical structures from *Cerefy* for the physics-based atlas.
2. Extract the *feature points* of each structure from the 2D atlas plates to form *point clouds*.
3. Build 3D surface and solid models from the extracted point clouds.
4. Systematic study of anatomy of head and brain, especially of brain tissue material to investigate material properties and to compare the findings with the deformation analysis that is previously made.

5. Derive an equilibrium equation for a continuum with the best suited material properties.
6. Select the appropriate finite elements and corresponding interpolation functions for the problem.
7. Generate high quality mesh elements (more than 6 node nonlinear tetrahedral elements) and subdivide the object into the elements.
8. All relevant variables on each element have to be interpolated by interpolation functions.
9. Assemble the set of equilibrium equations for all of the elements into a single system.
10. Choose a suitable biomechanical constitutive law of the material keeping in mind that material property (including conductivity, viscoelasticity, stress-strain relationship from layer to layer) of the brain tissue progresses continuously.
11. Implement the given boundary constrains.
12. Generate result according to the specified criterion
13. Validation of the model.
14. Visualization of the meshed model in a known platform.

The complete flowchart has been shown in following figure (Figure 1.1):

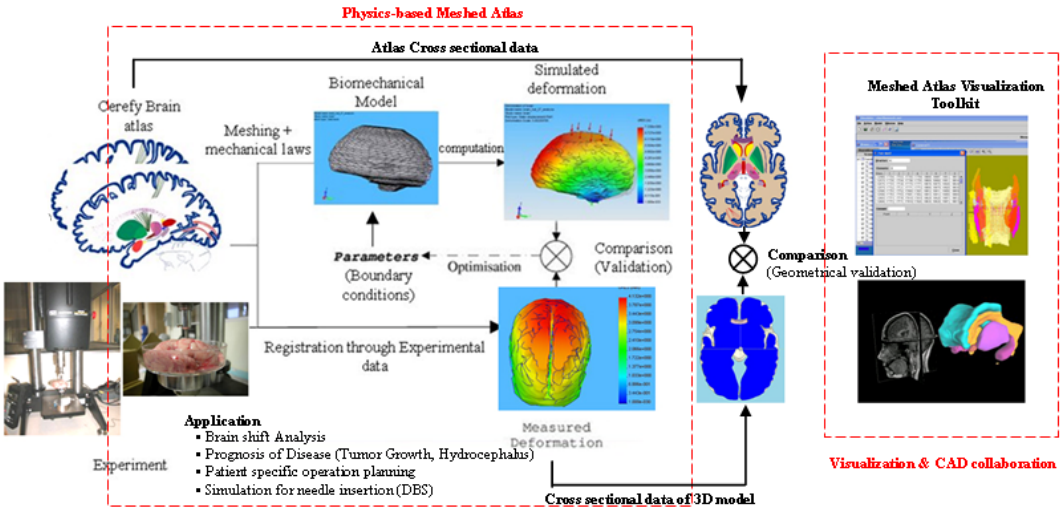

Figure 1.1 Flowchart of the proposed model

1.3 Anatomy of the Human Head and Brain[3]

Head is considered one of the most critical parts of the body. A general knowledge of the anatomy and physiology of the head is helpful in understanding the protective mechanisms of the brain and the study of the deformation, prognosis of various diseases (such as tumor growth, hydrocephalus) and intraoperative simulations. Brain is the control center of the body, including automatic control as well as sensory perception and motor function. Different tissue layers such as the scalp, skull bone, dural, arachnoidal and pia membranes as well as cerebrospinal fluid (CSF) cover the brain.

[3] The description of this section is based on various anatomy text books such as, Gardner et al (1960), Montemurro and Bruni (1981), Truex and Kellner (1948), McMinn, Hutchings and Logan (1994), Gillespie and Jackson (2000), Baggaley (2001) and Perez (2003).

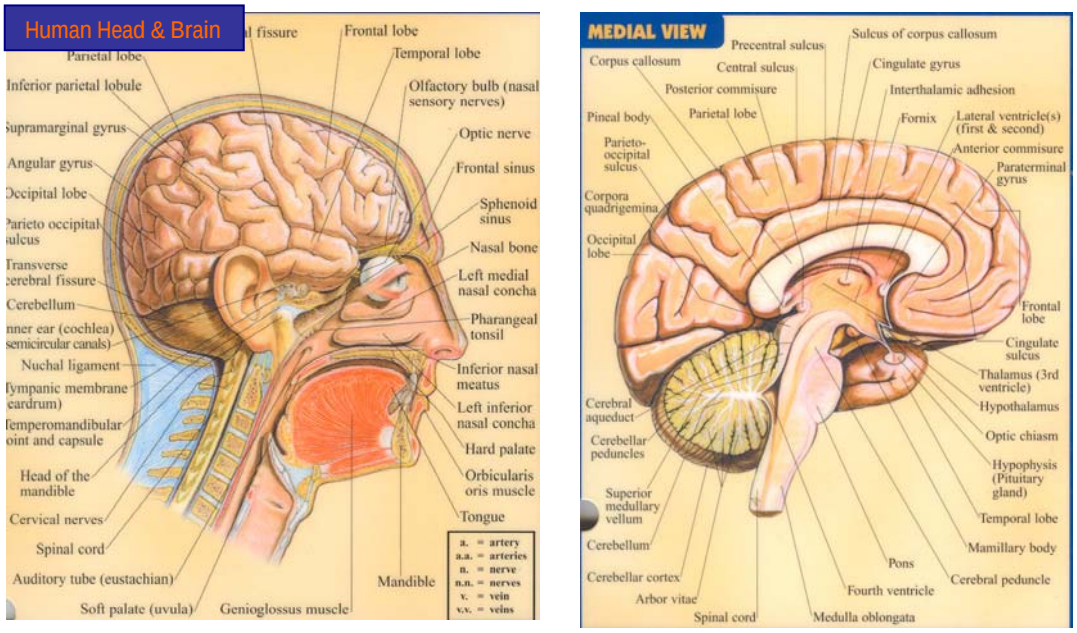

Figure 1.2 a) Human head, brain and neck b) Medial view of Brain (Perez V, 2003)

Figure 1.2 shows the midsagittal view of head, neck and brain (Figure 1.3 shows the sagittal and axial section of MRI image).

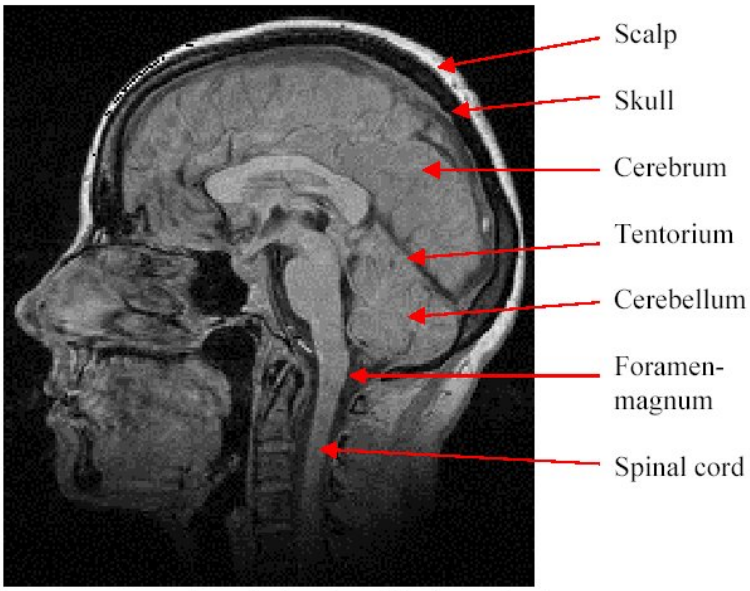

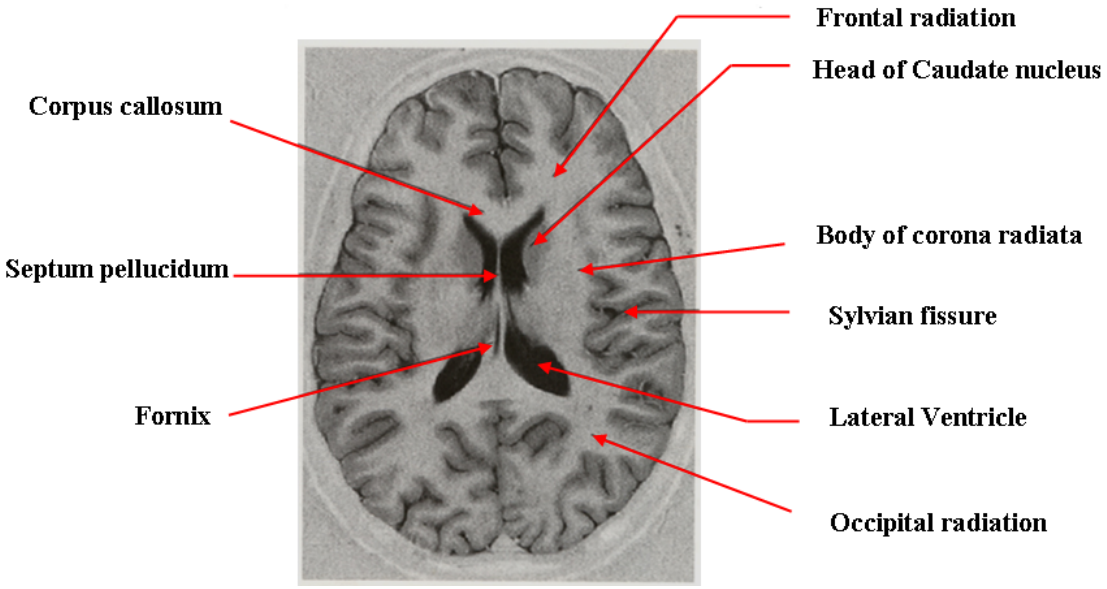

Figure 1.3 MRI scans of (a) sagittal section and (b) axial section of a human brain (Gillespie and Jackson, 2000; labeling is done by the author of this dissertation)

The skullbone can be viewed as a three-layered sandwich structure with an inner and outer table of compact bone and a dipolë of spongy bone sandwiched between them as a core. A sagittal dural partition membrane, the falx cerebri, partly separates the left and right hemispheres of the brain. The lower separating membrane, the tentorium cerebelli, resides on the inferior wall of the skull, and separates the cerebrum from the cerebellum and brain stem. The brain, with its covering membranes and CSF, is connected to the spinal cord through the foramen magnum. The inferior part of the skull base is attached to the neck by articulation through occipital condyles, ligaments and muscles.

1.3.1 Anatomical Planes

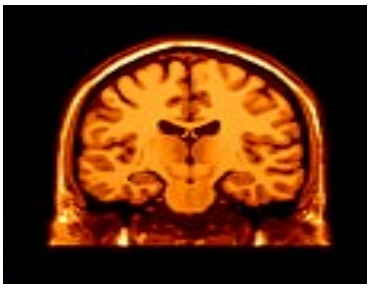

(a) Coronal section

(b) Axial section

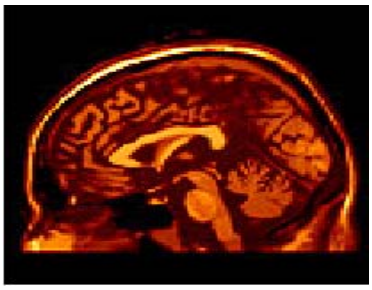

(b) Sagittal section

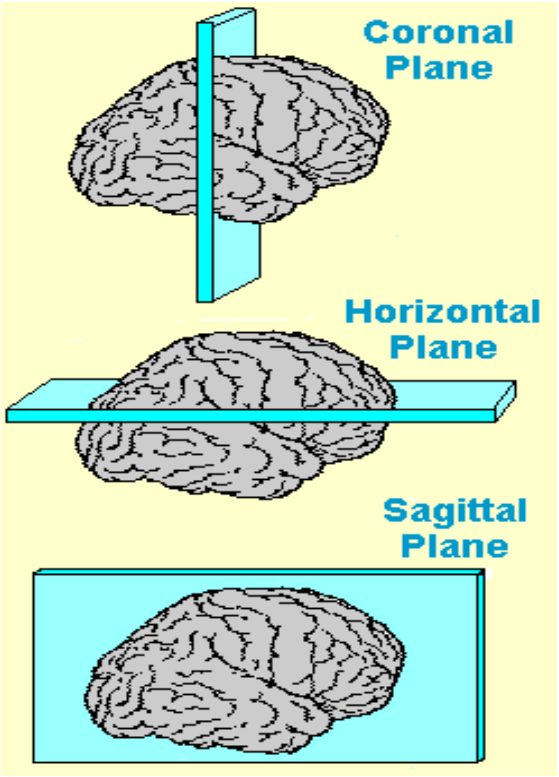

Figure 1.4 Anatomical planes and respective cross sections that provides a reference for the description of the brain and its parts

Particular sections of the brain are often viewed and described from hypothetical mutually perpendicular anatomical planes. In this dissertation, the same terms for the description of human brain parts will be employed. These planes are constructed from imaginary horizontal and vertical lines running through an upright head and body and are also used as a reference for position description. From anatomical point of view, brain can be seen through 3 main anatomical planes *Coronal, Sagittal* and *Axial* planes.

1. **Coronal or Frontal Plane:** A vertical plane running from the left side of the brain to the right side which divides the brain and its parts into anterior (front) and posterior (back) portions.
2. **Sagittal or Lateral Plane:** A vertical plane running from the front of the brain to back which divides the brain and its parts into the medial (right) and lateral (left) portion.
3. **Axial or Transverse Plane:** A horizontal plane which divides the brain and brain parts into superior (upper) and inferior (lower) portions. Axial images of *Cerefy* Brain Atlas (section 1.4) were used to construct physics-based model.

1.3.2 Properties of the human skull and brain

For this dissertation, brain tissue is the sole prime focus in analytical and computational model construction and experimental evaluation. However, since the human head is also composed of numerous different anatomical structures, such as scalp, cranial bones, meninges, dura mater, and cerebrospinal fluid etc, for the purpose of construction of complete physics-based head model in future, for determining material properties of various structures and setting up proper boundary conditions within the skull and brain, a brief discussion on each part will be worthy.

In order to describe the biomechanical behavior of different anatomical structures, various investigations have been carried out (Ommaya, 1968; Estes and McElhaney, 1970; Metz, 1970; Galford and McElhaney, 1970; Shuck and Advani, 1972; Pamidi and Advani, 1978; Schettini, 1988; Walsh, 1984 and 1990; Mendis et al, 1995; Miller et al, 1999, 2000, Farshad et al, 1998; Bilston and Liu, 1997; Donnelly and Medige, 1997; Prange and Marguiles, 2002, Schwartz et al, 2005 etc.). Especially in the case of brain tissue, these investigations led to different descriptions of its mechanical

properties, such as the validity of constructive equations used in previously developed biomechanical models remains unclear (Hagemann, 1999).

It is generally considered that biological materials do not follow the known constitutive relations for common engineering materials. A biological material is often anisotropic, inhomogeneous, nonlinear and viscoelastic. In addition, there is a great variability between different individuals and animals.

1.3.2.1 Scalp

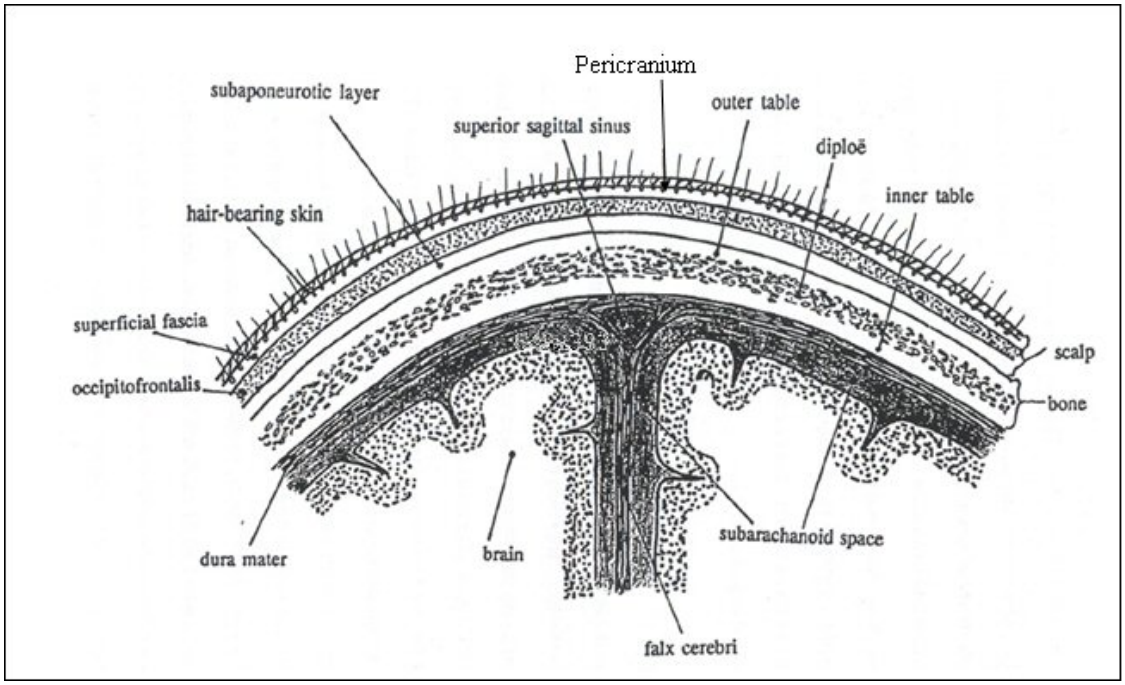

Figure 1.5 Coronal section of the scalp (Ruan, 1994a)

The scalp is 5 to 7 mm thick and consists of five layers: the skin, subcutaneous layer (superficial fascia), aponeurotic layer, subaponeurotic layer and pericranium of the skull. First three layers are closely connected and move as a unit. The skin of the scalp,

consisting of epidermits and corium and usually including hair, is the thickest in the body. The subcutaneous layer consists of dense fatty areolar tissue tightly bound to both skin above and to the next layer below, the galea aponeurotica. While subcutaneous layer is valscularized, the aponeurotic layer is muscular and consists of the epicranial muscle. The subaponeurotic layer is a loose areolar tissue that intervenes everywhere between the galea aponeurotica and the underlying periosteum of the skull. It permits the scalp to move freely upon the skull and also allows blood to spread easily within the substance.

Beneath the scalp there is a loose connective layer plus the fibrous membrane that covers the bones. A limited number of fresh human scalp specimens were tested in compression by Melvin (1970). The material behavior is found almost linearly elastic until strains of 30-40 % were applied. Larger strains give a concave stress-strain curve which is typical of most soft biological tissues. A series of relaxation tests were performed in tension on monkey scalp specimens (Galford and McElhaney, 1970). The specimen was brought to an instantaneous fixed strain and the load was measured over a period of time. A typical viscoelastic stress relaxation behavior for the monkey scalp has been observed.

1.3.2.2 Cranial bones

The thickness of the skull varies between 4 and 7 mm. The base of the braincase is an irregular plate of bone containing depressions and ridges plus small holes (foramen) for arteries, veins, and nerves, as well as the large hole (the foramen magnum) that is the transition area between the spinal cord and the brainstem (Figure 1.5). The bones of the cranium are connected at lines called sutures.

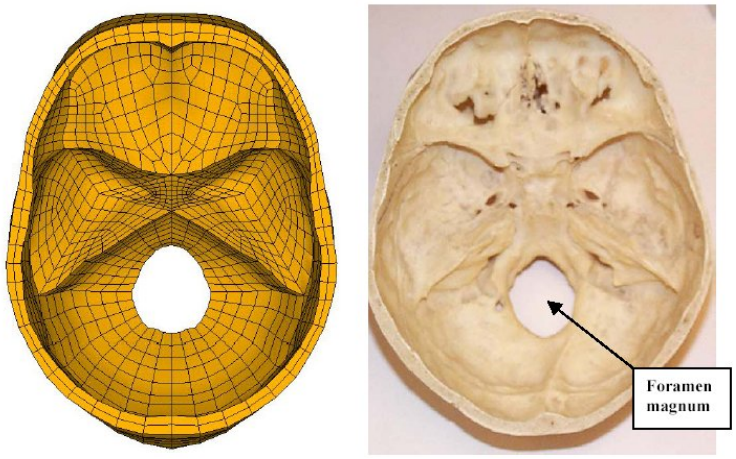

Figure 1.6 Skullbase of the human head (right), and an FE representation of the skullbase using an intermediate element mesh density (left) (Kleiven, 2002).

Several experiments have been performed on human cranial bones. The bones considered in the experiments were the frontal, left and right parietal, and the occipital. In the human, these bones show two well-defined shells of compact bones separated by a core of spongy cancellous bone, called dipolë. Compact bone surrounds and reinforces the sutures. The inner and outer layer of compact bone in the skull can (unlike the long bones) be considered to be isotropic in the tangential direction of the skull bone (transversely isotropic).

This can be explained by the random orientation of the cortical grain structure of the inner and outer table of compact bone. The spongy bone varies in structure with narrow spaces normally ranging from 3 mm in diameter down to microscopic size. This gives a wide range of mechanical responses. In a series of experiments performed on human cranial bones (McElhaney et al., 1970), the modulus of elasticity for tangential compression was found to be more than 2 times larger than that for radial compression. By compression tests, and measurement of the deformation in both the load direction and perpendicular to it the Poisson's ratio was determined for both the

radial direction, υ_r=0.19, and the tangential direction, υ_t=0.22. In general skull bone is a rather rigid material which is brittle and cracks at low strain rates. The stress-strain relationship is considered similar to many engineering materials like steel or aluminum (Fung, 1993), i.e. the stress-strain relationship is a rather linear one thus suggesting that Hooke's law is applicable (Viano, 1986; Fung, 1993). In this work modeling of brain was of area of interest, not the skull itself. Nevertheless, background study of the properties of the skull is important as it is essential to establish correct boundary condition depending on the observed behavior in the later stage. A summary of the properties of the cranial bone determined in different studies can be seen in Table 1-1. below:

Table 1-1 Properties of Cranial bone

Reference	*Ec* *GPa*	σ_{fc} *MPa*	*Et* *GPa*	σ_{ft} *MPa*	τ_{fd} *MPa*
McElhaney *et al.* (1970)	2.4*	73.8	12.4-20.0#	69.0-98.6#	21.4
Barber *et al*. (1970)	0.7	71.5			
Melvin *et al*. (1970)	1.0	32.4			
Robbins *et al.* (1969)	1.4	36.6	14.6	65.5	13.1
Wood (1971)			10.3-22.1#	48.3-127.6#	
Schueler *et al.* (1994)	0.3	130.0			15.0

E_c=Young's modulus in radial compression, σ_{fc}=failure stress in radial compression, E_t=Young's modulus for compact bone in tension, σ_{ft}=failure stress for compact bone in tension, τ_{fd}=failure stress for diploë in shear.

*Results from very porous diploë were removed from the analysis.
#Young's modulus and failure stress depends on strain rate.

1.3.2.3 Meninges

The meninges consist primarily of connective tissue, and they also form part of the walls of blood vessels and the sheaths of nerves as they enter the brain and as they

emerge from the skull. The meninges consist of three layers: the dura mater, the arachnoid, and the pia mater.

Brain tissue, having the consistency of a heavy pudding, is the most delicate of all body tissues. For protection, this vital organ is located in a sealed bony chamber, the skull. To protect it further from the rough bone and from blows and shocks to the head, the brain is enveloped by the meninges. The outermost dura mater is adherent or close to the inner surface of the bone. Beneath the dura mater is the middle covering, the thin and fibrous arachnoid. The third and innermost layer is the very thin, delicate, and capillary-rich pia mater, which is intimately attached to the brain and dips down into the sulci and fissures.

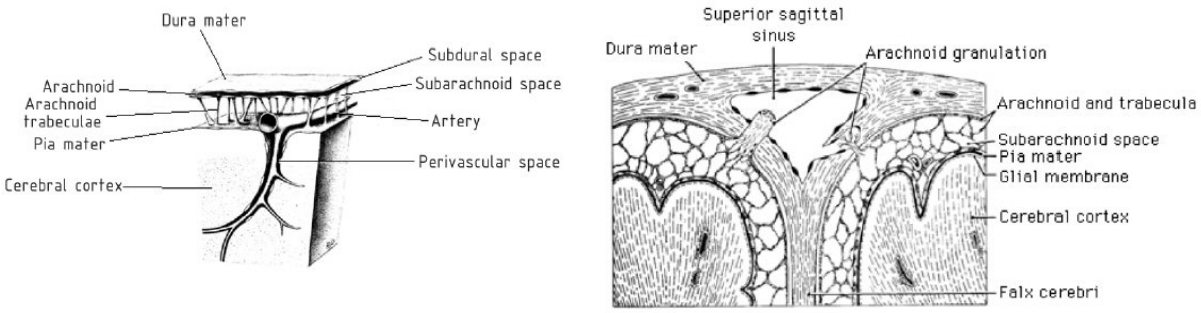

Figure 1.7 Meninges a) 3 dimensional view b) sectional view (Dalhousie University, Department of Anatomy and Neurobiology, 2004)

Between the dura mater and the underlying arachnoid is a narrow subdural space filled with a small amount of fluid that acts as a lubricant, preventing adhesion between the two membranes. Separating the arachnoid from the pia mater is a relatively large gap,

the subarachnoid space, which is filled with Cerebrospinal fluid, commonly abbreviated as CSF. This clear, lymphlike fluid fills the entire subarachnoid space and surrounds the brain with a protective cushion that absorbs shock waves to the head (for detailed discussion check the section 1.3.2.5). As a further means of protection, there are fibrous filaments known as arachnoid trabeculations, which extend from the arachnoid to the pia and help "anchor" the brain to prevent it from excessive movement in cases of sudden acceleration or deceleration.

1.3.2.4 Dura Mater

The dura mater is a tough, fibrous membrane that surrounds the spinal cord and the inner surface of the skull. Folds of the dura mater form the falx cerebri, which projects into the longitudinal fissure between the right and left cerebral hemispheres (Fig. 4 and 5). Another dural fold forms the tentorium cerebelli, a membrane separating the cerebrum from the cerebellum and brain stem.

A theoretical development by Den Hartog (1952) was later used by Magulies (1987) to determine a small strain Young's Modulus from the inflation pressure, followed by the equation:

$$P = \frac{8}{3}\frac{E}{1-\nu}\frac{t}{R}\left(\frac{w}{R}\right)^3 \tag{1.1}$$

Where P = Inflation pressure
E = Young's Modulus
ν = Poisson's Ratio
R = Radius of specimen
w = Center deflection
t = Specimen thickness

In her experiment Magulies placed the samples of dura in a device that clamped the specimens so that one side was exposed to 1.8cm hole. The exposed circular membrane was then inflated by constant (fluid) pressure to use the above equation (1.1). However, the equation holds a linear constitutive properties i.e, a plot of P vs. w^3 would give a straight line.

The Young's modulus of human dura mater was also determined using tensile testing by Melvin (1970). According to his findings the macrostructure of the dura mater appeared to be a membrane with evident directions of fiber reinforcement. However, strain rate effects and biological variability overshadowed the effect of the fiber direction. He found values in the range of 41-55 MPa for the Young's modulus in tension. The results showed that a small amount of initial strain occurs with no load. This can be explained by the fibrous tissue not taking any load during small deformations. It just straightens out, and only the weaker connective tissue takes load. Biological membranes exhibit a significant amount of strain before realizing significant stress had also been confirmed by other researchers (Fung, 1993; Magulies, 1987; Mendis, 1992).

Tensile creep tests were performed by Galford and McElhaney (1970) on human and monkey dura mater to derive viscoelastic parameters. The stress relaxation function of the following form was assumed for the dura:

$$G(t) = G^{\infty} + \Delta G.e^{\frac{t}{\tau}} \qquad (1.2)$$

Where $\Delta G^{\infty} = (G^0 - G^{\infty})$

$G^0 =$ Short term shear modulus

$G\infty =$ Long term shear modulus

$t =$ time

An ideal creep experiment consists of measuring the deformation-time history of a material sample subjected to a constant stress. The creep compliance curves are linear on a semilog graph. Kriewall et al (1983) and Bylski et al (1986) used a strain energy function approach to characterize large strain material properties:

$$W(\bar{I}_1, \bar{I}_2) = \frac{B}{4}\left[\frac{\bar{I}_1^2}{2} + \bar{I}_1 + \bar{I}_2\right] + \frac{C}{8}\bar{I}_2^2 \tag{1.3}$$

Where the first and second strain invariants are defined as,

$$\bar{I}_1 = \lambda_1^2 + \lambda_2^2 - 2$$

$$\bar{I}_2 = \lambda_1^2 \lambda_2^2 - 2$$

And brain material const. B/C ratio = 0.25 (Kriewall et al, 1983)

The ultimate strain for dura mater was determined to lie between 0.130 and 0.181 and the strength to lie between 1.44 and 4.65 MPa in tension by Zhivoderov et al. (1983).

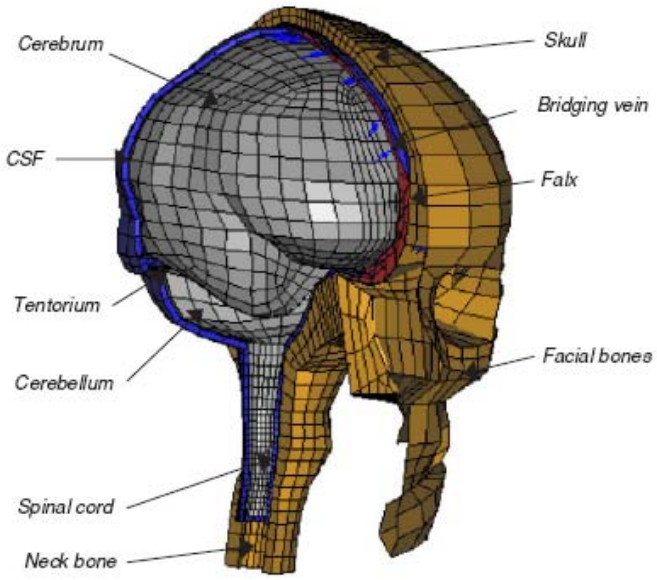

Figure 1.8 Finite element model of internal, separating membranes; tentorium and falx of the human head is shown. An FE representation of the falx and tentorium, including eleven pairs of the bridging veins has been labeled. (Kleiven, 2002)

1.3.2.5 Cerebrospinal fluid

The soft tissues of the brain and spinal cord are protected by the bony casings of the skull and vertebrae; for additional protection the tissues are surrounded by a clear watery fluid called Cerebrospinal fluid (CSF). It is contained in the ventricular system and the subarachnoidal space[4] and is generally taken as an incompressible fluid (Sahay et al, 1992; Tada et al, 1994). This liquid is produced inside the ventricles (chambers) of the brain and is renewed 3-4 times a day. Due to its biomechanical similarity to blood plasma, some researchers assume equivalent physical properties for the cerebrospinal fluid (Hagemann, 2001). Stokes equation which takes into account the fluid incompressibility characteristics can be used to simulate the biomechanical properties of CSF (Hagemann, 2001):

$$\rho\left[\frac{\partial u}{\partial t} + u \cdot \nabla u\right] = -\nabla p + \mu \nabla^2 u \tag{1.4}$$

where u is the fluid (CSF) velocity, ρ the density, μ the viscosity and p the pressure.

1.3.2.6 Brain Tissue

At a microscopic level, the Central Nervous System (CNS) is primarily a network of neurons and supportive tissue functionally arranged into areas that are gray or white in color. Gray matter is composed primarily of nerve-cell bodies concentrated in locations on the surface of the brain and deep within the brain. White matter is composed of myelinated (myelin=a soft white somewhat fatty material) axons that largely form tracts to connect parts of the CNS to each other.

---

[4] Subarachnoidal space is the space between brain tissue and the dura mater.

From the standpoint of engineering material, brain tissue can be likened to a soft gel. Because of the high water content (about 80 %), it is nearly incompressible. This is also confirmed by reported values of the bulk modulus for brain tissue of about K=2.1 GPa (Stalnaker, 1969, McElhaney et al., 1976) which is roughly 10^5 times larger than the shear modulus. Thus, the deformation of brain tissue can be assumed to depend on the shear modulus only. Most of the testing of brain tissue has therefore been performed in shear or torsion.

The brain tissue has been modeled in various ways; one of the recent attempts is using a viscoelastic material model (similar to equation 1.2) with shear relaxation behavior described by (Ruan, 1994a; Zhou, 1995):

$$G(t) = G^{\infty} + (G^{0} - G^{\infty})e^{-\beta t} \tag{1.5}$$

Where G^0 = Short term shear modulus
$G\infty$ = Long term (infinite) shear modulus
β = decay coefficient
t = time

β varies from β=0.035ms^{-1} to 0.145ms^{-1}, the short-time shear modulus G^0 = from 528 KPa to 49KPa and the long-time (infinite) shear modulus from $G\infty$ = =168KPa to G ∞ =16.7KPa.

Mendis et al. (1992, 1995) introduced non-linear constitutive relations for large deformations. Miller (1999, 2002a), and Miller and Chinzei (2000, 2002b) also presented non-linear and hyperviscoelastic models for both compression and tension experiments. Their analyses assume the brain material response function to be completely determined by the existing stored (strain) energy function. The strain

energy function can either be a direct function of the principal stretch ratios W = W($\lambda_1, \lambda_2, \lambda_3$) or a function of the strain invariants W = W($\bar{I}_1, \bar{I}_2, \bar{I}_3$). There are several forms of the strain energy function in the literature. The detailed mathematical formulation will be discussed in the next chapter (section 2.3.5). Various areas of dispute in modeling of brain tissue behavior will be discussed in chapter three (section 3.3).

1.4 Human Brain Atlases

Human brain atlases can be classified from various view points including: medium (print, electronic), type of source material (e.g., cryosections, radiologic images, Visible Human Data), population of source material {low (deterministic atlas), high (probabilistic atlas)}, and content (anatomy, function, vasculature). Similarly, an atlas-based application can be considered in terms of: field (education, research, clinical), functionality (atlas-specific, problem-specific), cost (e.g., a low cost CD versus a high end virtual reality solution), accessibility (web-based, stand-alone, plug-in library) etc.

1.4.1 Printed Atlases

Before the prevalence of Information Technology, numerous excellent *printed brain atlases* had already been available, such as *Photographics* (DeArmond et al, 1989), *Stereo* (Kraus et al, 1994), *Duvernoy* (1988), *Nette*r (1991) etc. In addition, several stereotactic brain atlases including *Talairach-Tournoux* (1988, 1993) have also been constructed. These atlases use to provide very generic and nonspecific information.

Moreover, since they are printed on paper, a major limitation of these atlases is the difficulty in mapping into an individual brain.

1.4.2 Electronic Brain Atlases

Deformable electronic atlases overcome some shortcomings of the print atlases and open new avenues. Its not just a simple "electronic transformation" of printed atlases, rather it describes a complex system consisting 3 major components: Brain model (these can be images, contours, surface, polygonal or volumetric models), Textural Database (the list of structures with their descriptions and related links) and Supporting tools (for operations such as registration, labeling, mensuration, or presentation) along with corresponding data, such as labels (Figure 1.9). In addition to atlas warping, they offer new features not available in print atlases, such as interactive labeling of scans, flexible ways of presentation in 2D and 3D (and generally in nD space), mensuration, searching, integration of knowledge from multiple sources, and aggregation of information from numerous cases.

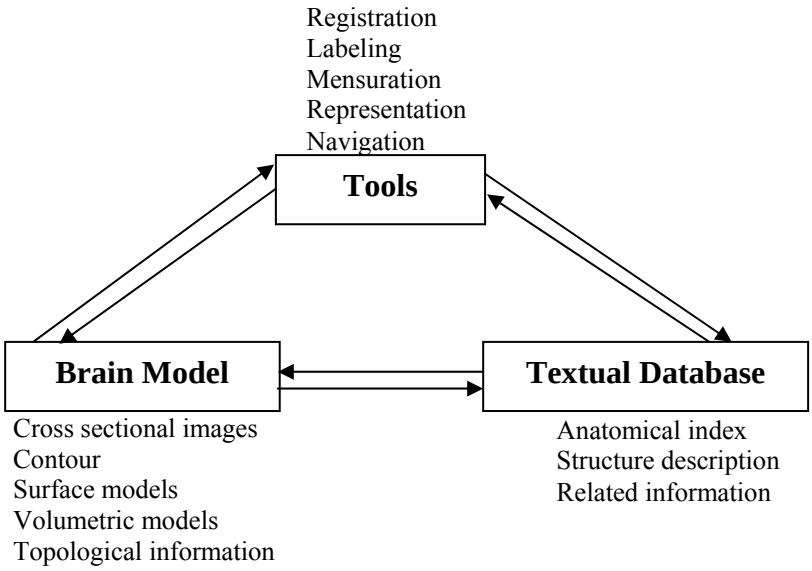

Figure 1.9 Definition of Electronic Brain Atlas (Nowinski, 2002a)

1.4.2.1 Cerefy Electronic Brain Atlas

Combining with the widely accepted stereotactic printed atlases with new features provided by the electronic atlases, many printed atlases have been converted into electronic form. Among them *Cerefy* electronic brain atlas database (Nowinski, 1997; 2001b; 2001c) contains several version of printed brain atlases published by *Thieme* (Schaltenbrand and Wahren, 1977; Talairach and Tournoux, 1988; Ono et al, 1990; Talairach and Tournoux, 1993).

This electronic atlas database with complementary atlases contains gross anatomy, subcortical structures, brain connections, and sulcal patterns. This database consists of two-dimensional and three-dimensional, mutually co-registered atlases with about 1000 structures and 400 sulcal patterns. Their three-dimensional extensions were constructed. In addition, all two-dimensional (2D) and three-dimensional (3D) atlases were mutually coregistered. The electronic atlas images were pre-labeled to speed up structure labeling in atlas-based applications. About 17,000 labels were placed manually for the entire *Cerefy* brain atlas database. Till date about eleven commercial applications[5] have been developed based on this database suitable for neuroradiology, neuroeducation, human brain mapping, and stereotactic functional neurosurgery. The

[5] Applications are in Neuroeducation (Brain Anatomy 1.0, Anatomy 1.0 : Chinese Edition), Neuroradiology (Neuroradiology Atlas 2.2), Neuroscience (Functional Imaging 1.0), Neurosurgery (Clinical Brain Atlas 1.0, Enhanced Edition with Surgical Planning and Intraoperative Support 1.0), Libraries (Geometrical Models 2.0, Brain Atlas Library 1.0, Probabilistic Functional Atlas 1.0, Cerebrovascular Atlas, Blood Supply Territories Atlas) etc. Brain Atlas is now also used extensively by major image-guided surgery companies including Medtronic (USA), BrainLAB (Germany) etc.

commercial applications are available in separate CD-ROMs. The features of the atlas are that made *Cerefy* unique are:

1. It reduces time in image interpretation by providing interactive multiple labeling, triplanar display, higher parcellation than the scan itself, multi-modal fusion, and display of underlying anatomy for functional images;
2. It facilitates the communication of information about the interpreted scans from the neuroradiologist to other clinicians and medical students;
3. It increases the neuroradiologist's confidence; and
4. It reduces time in learning neuroanatomy and scan interpretation.

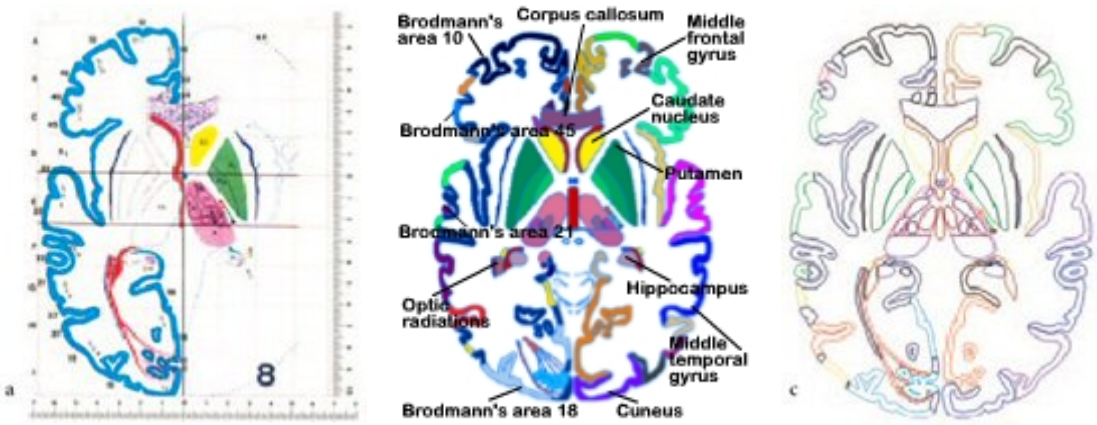

Figure 1.10 Brain atlas. a) Digitized original printed axial plate. b) Derived corresponding electronic image fully color-coded and labeled with subcortical structures, gyri, and Brodmann's areas (full and abbreviated names are used). c) Derived corresponding color-coded contours (Nowinski, 2002 a)

Main focus of the project is to provide atlas-based solutions for clinical practice (intraoperative computation such as brain shift, patient specific operation planning prognosis of various diseases such as tumor growth or hydrocephalus, needle insertion or Deep Brain Stimulation etc.) using the excellent built-in advantages and features of *Cerefy*. It is the task of biomechanical modeling to assign reliable physical properties

to virtual anatomical structures in order to make them interact according to underlying physical laws. For this, realistic representation of virtual structures is the prerequisite. *Cerefy* has given an excellent opportunity to develop virtual brain model with detailed anatomical structures. The more realistic the physical model approaches, the more realistically the simulation result (in predicting soft tissue deformation) can be attained (Gladilin, 2003). This prediction is the central paradigm of the physics-based soft tissue modeling for the atlas-based solution to clinical practices mentioned above.

Cerefy electronic brain atlas database is now the standard in stereotactic functional neurosurgery, and has already been adopted by several companies specializing in image-guided surgery. Therefore, adopting *Cerefy* Brain Atlas to build Finite element brain model for this project is a right choice.

1.5 Summary of the chapter

This chapter describes the author's motivation and scope of the research. A brief overview of *Cerefy* brain atlas with the anatomy of the human head and brain are also provided. The next chapter will discuss the background of biomechanics and soft tissue modeling.

Chapter 2

BACKGROUND KNOWLEDGE ON BIOMECHANICS AND SOFT TISSUE MODELING

2.1 Biomechanics and biomechanical modeling

Biomechanics combines the field of engineering mechanics with the fields of biology and physiology and is concerned with the analysis of mechanical principles of the human body. While studying the living tissue biomechanics, the common practice has always been to utilize the engineering methods and models known from "classic" material science. However, the living tissues have properties that make them very different from normal engineering materials. The first important fact is that all living tissues are open thermodynamic systems. Living organisms permanently consume energy and exchange matter with their environment to maintain the essential metabolic processes. For example, living tissues such as skin etc. have *self-adapting* and *self-repairing* abilities (Gladilin, 2003), which enable wound healing and stress relaxation of loaded tissue. The biomechanical modeling of biological structures requires a comprehensive knowledge of the following major fields of study

- Anatomy
- Continuum mechanics
- Numerical mathematics, in particular, the finite element method.

This chapter is divided in two major sections, the first section covers the basic structure and properties of soft tissue and second section covers the basics of

continuum mechanics which cover issues relevant to the numerical modeling of deformable soft tissue.

2.2 Soft Tissue: Structure and Properties

In this section, we make a brief overview of anatomy and biophysics of brain and other soft tissues with emphasis on their passive mechanical properties.

2.2.1 Anatomy of soft tissue

Soft tissue is a collective term for almost all anatomical structures, which can be named soft in comparison to bones. In this section, we focus on biomechanical modeling of soft tissues like brain, kidney, liver, prostates that do not bear any mechanical load.

Soft tissues are mainly composed of different types of polymeric molecules embedded in a hydrophilic gel called ground substance (Fung, 1993). Basic structural elements of soft tissues are elastin, actin, reticulin, collagen and other polymeric proteins. Biopolymers are organized in hierarchical bundles of fibers arranged in a more or less parallel fashion in the direction of the effort handled (Maurel, 1998).

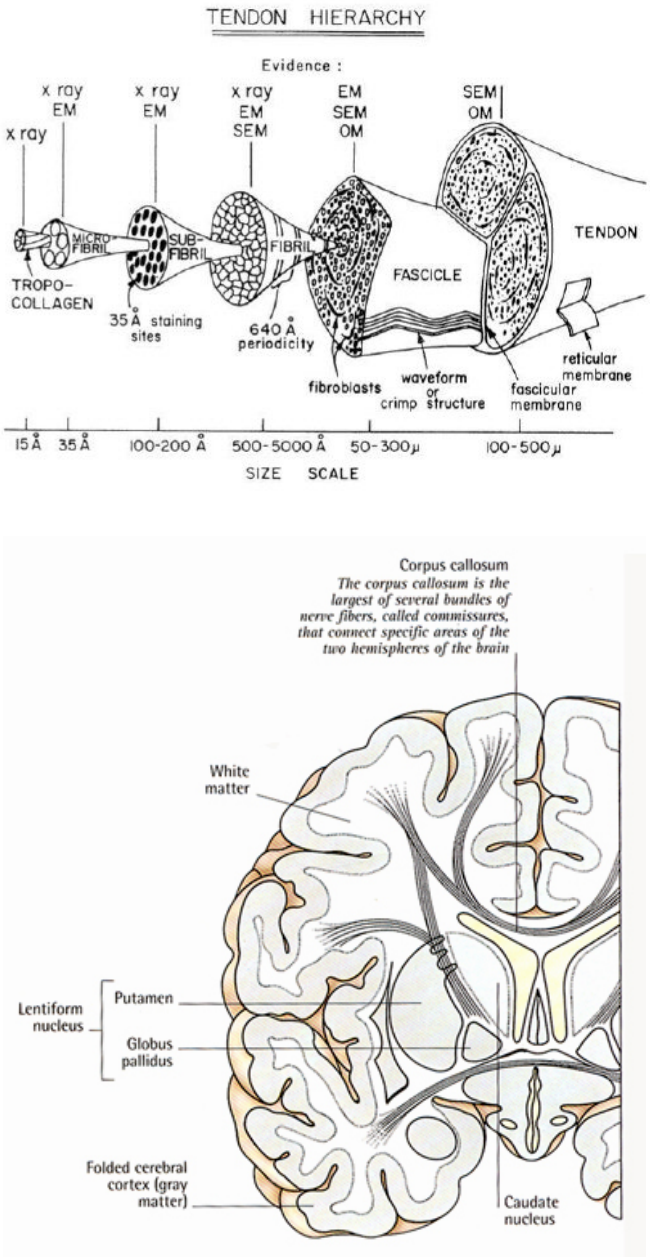

Figure 2.1 (a) Hierarchical organization of fibrous structures in tendon (from Fung, 1993). (b) Structure of gray and white matter inside the brain (Baggaley, 2001)

The human brain is a soft yielding structure that is not as stiff as a gel or as plastic as a paste (Ommaya 1968; Goldsmith 1972; Akkas 1979). It is composed of 77% water, 10-12% lipids, 8% protein and rest consist of organic salts, inorganic substances and carbohydrates. The soft tissue of brain consists of *gray matter*, 2-6 mm thick, containing neuronal cell that is not surrounded by myelin, and *white matter*, containing interconnecting long nerve fibers surrounding by myelin sheath (between areas of gray

matter) that gives the tissue a white appearance (Figure 2.1 b). The tissue is covered by the dura, arachnoid, and pia membranes, with the space between the arachnoid and pia (subarachnoid space) filled with the cerebrospinal fluid (CSF), a clear, colorless fluid. The subarachnoid space communicates with the four ventricles filled with CSF.

Numerous experimental and theoretical studies in the field of tissue biomechanics have been carried out in recent years (Fung, 1993; Maurel et al. 1998, Ozkaya, 1999; Begun et al. 2000). Among the different types of soft tissues, the mechanical behavior of brain tissue was of particular interest for a long time. However, it was little known about the mechanical properties of the central nervous system before late 1960's. Ommaya (1968) gave good review of early studies that were performed in this area (Darvish, 2000). At that time, all studies were carried out in vitro. Elementary rheologic experiments on brain slices taken from rabbits, rats and pigs showed elastic modulli range of 8-15kPa. Till then various experiments have been carried out and several models were proposed. Compared to brain, there is a very little experimental data on the biomechanical properties of liver and kidney is available in the literature. Recently some experimental studies have been conducted by Schmidlin et al (1996) & Farshad et al. (1998) on swine kidney and Liu and Bilston (2000), Schwartz et al (2005) on liver.

Summarizing the facts observed in different experiments with different tissue types, soft tissues generally exhibit *non-homogeneous, anisotropic, quasi-incompressible, nonlinear plastic-viscoelastic* material properties, and nonlinear hyperviscoelastic model is found to be suitable for such analysis which we will briefly describe hereafter.

2.2.2 Non-homogeneity, anisotropy

Soft tissues are multi-composite materials containing cells, intracellular matrix, fibrous and other microscopical structures. This means that the mechanical properties of living tissues vary from point to point within the tissue. Essential for modeling are the spatial distribution of material stiffness and the organization of fibrous structures such as collagen and elastin fibers, which have some preferential orientation in soft tissue like skin. The dependence on coordinates along the same spatial direction is called non-homogeneity. If a material property depends on the direction, such material is called anisotropic. Tissues are both non-homogeneous and anisotropic. However, there are practically no quantitative data about these properties and thus their accurate modeling of tissue is still quite uncertain, though Marguilis and her collaborators (Prange and Margulies, 2002; Gefen and Margulies, 2004; Coats and Margulies et al 2005) have recently provided some important insight on few occasions.

2.2.3 Nonlinearity

The stress-strain relationship, the so-called *constitutive equation* of soft organs like brain, liver, kidney, prostates is nonlinear in nature (Ozkaya and Nordin, 1999). The nonlinear stress-strain curve, shown in Figure 2.2, is usually divided in four unique phases.

- ***Phase I:*** $\varepsilon < \varepsilon_A$ ***:*** At low strains, the response of soft tissue is linear.

- ***Phase II:*** $\varepsilon_A < \varepsilon < \varepsilon_B$***:*** At moderate strains, the straightening of tissue fibers occurs and the stiffness increases in a nonlinear fashion;

- ***Phase III:*** $\varepsilon_B < \varepsilon < \varepsilon_C$*:* at high strains, all fibers are straight and the stress-strain relationship becomes linear again.

- ***Phase IV***: $\varepsilon > \varepsilon_C$ at very high strains, material destruction takes place.

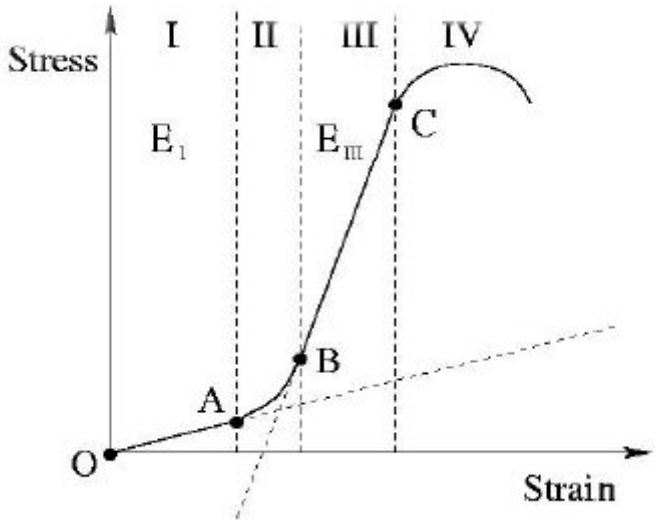

Figure 2.2 Nonlinear stress-strain curve of soft tissue (Fung, 1993; Ozkaya and Nordin, 1999)

In modeling of some soft tissues (blood vessels, muscles, skin etc.), the nonlinearity of phase II is often neglected and stress-strain curve is considered as piecewise linear (Ferrant, 2001b; Gladilin, 2003). But there is no certain quantitative data about the stiffness coefficients E_{I-III} and the critical strains $\varepsilon_{A,B,C}$ for the bilinear approximation of soft tissue. It is also observed that these parameters depend on different factors. For instance, the critical strain ε_C decreases with age (Maurel, 1998); significant variation in directional, regional and age-dependent properties are also noted by other researchers (Prange and Margulies, 2002).

It should be pointed that the load-deformation/stress-strain curve of brain tissue deviate significantly from the behavior of tendons, blood vessels, muscles and skin as described

above. Brain tissue is unique in this case since it shows a completely nonlinear load-deformation curve without any linear parts (Estes and McElhaney, Metz et al, 1970; Walsh and Schettini, 1984, Hagemann, 2001). A typical stress-strain curve for brain tissue has been shown in the Figure 2.3.

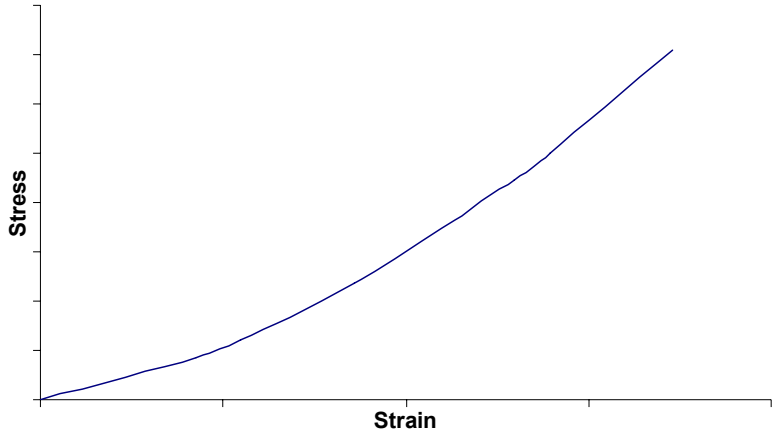

Figure 2.3 Typical nonlinear stress-strain curve of brain tissue (the curve is plotted from the data obtained from the experimentation in Bioengineering Lab National University of Singapore)[6]

In this work a fully nonlinear (i.e. accounting for both geometric and physical nonlinearities[7]) finite element 3D brain model has been constructed. The related issues will be discussed in later chapters.

---

[6] For detailed description kindly refer to chapter 5 of the dissertation.

[7] *Physical nonlinearity*: The nonlinear stress-strain relationship of soft tissue, which is given by the empiric curve, shown in Fig. 2.2 and Fig 2.3. is called physical or material nonlinearity.

Geometrical nonlinearity: Geometric nonlinearities occur in models with large displacements or rotations, large strain, or a combination of those. Mapping of displacement field with strain ($u \rightarrow \varepsilon$) is generally considered nonlinear.

2.2.4 Plasticity (Hysteresis and Stress Relaxation)

Plasticity is the property of a material to undergo permanent deformation under load. The deformation of physical bodies is reversible in the range of small strains only. Large deformations lead to irreversible destruction of material, which appears as a cyclic stress-strain curve that shows the basic difference of material response in loading and unloading, which is represented by *hysteresis* loop (Fig. 2.4).

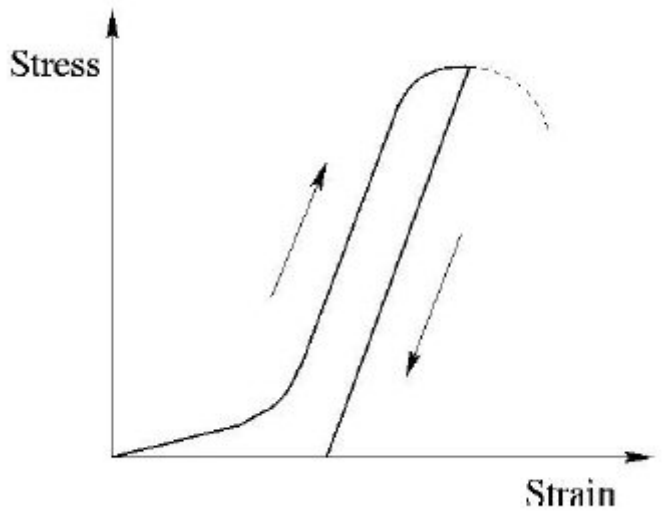

Figure 2.4 Hysteresis loop for an elasto-plastic material (Ozkaya and Nordin, 1999)

Such deformations are called plastic as opposed to reversible elastic deformations. It is reasonable to assume that soft tissue exhibits plastic behavior up to some critical strain as every known engineering material. However, as mentioned previously, some living tissues (such as skin) possess a very dominant feature of self-repairing ability, which means that after a certain period of time the destructive alterations are reversed by repairing mechanisms. Nevertheless a “time factor” which may vary in person, age and region could be essential for the choice of an appropriate material model of soft tissue biomechanics. Additionally, for multiple, subsequent loading/unloading cycles of a

tissue specimen, the load-deformation curve is usually shifted to larger deformations (Hagemann, 2001). The difference between successive cycles decreases and even disappears if the test is repeated infinitely often. In this case, the tissue specimen is said to be *preconditioned* (Fung, 1993) and shows a well defined load-deformation curve, thus allowing a unique description of the mechanical tissue properties.

The other important property shared by the most existing biological tissues is *stress relaxation* (Fig. 2.5) which denotes the process of gradually decreasing load when a tissue specimen is suddenly stretched and maintained at new length (Maurel et al, 1998). Stress relaxation will be discussed detailed in the next section as it has a relation with viscoelastic behavior of the material.

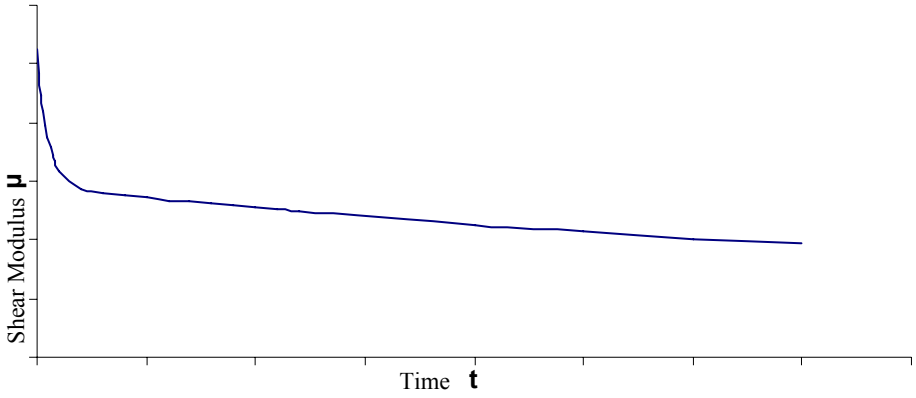

Figure 2.5 Typical time dependent relaxation curve for brain tissue

2.2.5 Viscoelasticity and Hyperviscoelasticity

The time-dependent material behavior is called viscoelasticity. The response of such materials depends on the history of the deformation, that is the stress $\sigma = \sigma(\varepsilon, \varepsilon^t)$ is a function of both the strain ε and the strain rate $\varepsilon^t = d\varepsilon/dt$, where t is the time. Viscosity is originally a fluid property. Elasticity is a property of solid materials.

Therefore, a viscoelastic material combines both fluid (Newtonian liquid) and solid (Hookean solid) properties. Soft tissue, for example brain, skin, blood vessel, kidney, liver prostates etc. have such viscoelastic characteristics. Two characteristics of tissue time-dependent behavior for viscoelasticity are *creep* and *stress relaxation* or *recovery*. Both creep and recovery can be explained by observing the material response to a constant stress σ_0 applied at time t_0 and removed at time t_1 .

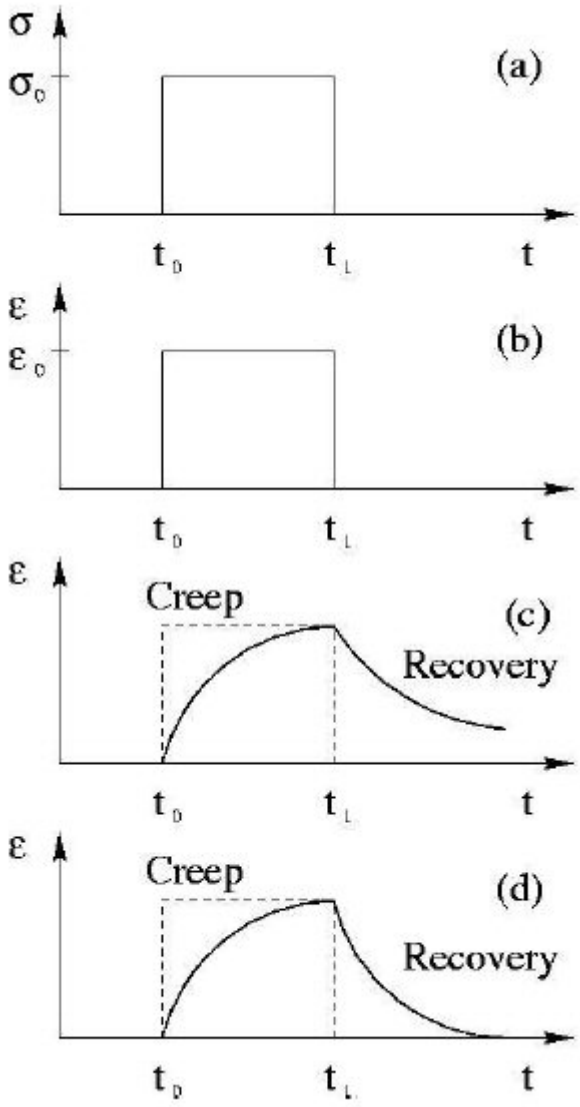

Figure 2.6 Creep and recovery (Ozkaya and Nordin, 1999). (a): constant stress σ_0 applied at time t_0 and removed at time t_1. (b): response of a linear elastic material. (c): response of a viscoelastic fluid. (d): response of a viscoelastic solid

The responses of a linear elastic solid, a viscoelastic solid and a viscoelastic fluid are shown in Figure 2.6. A linear elastic material shows an immediate response and completely recovers the deformation after the removal of loading. This situation is shown in Figure 2.6 (b). A viscoelastic solid responds with an exponentially increasing strain $\varepsilon \sim \{1 - \exp(-t/\tau_1)\}$ between times t_0 and t_1. After the loading is removed, at time t_1, an exponential recovery $\varepsilon \sim \exp(-t/\tau_1)$ begins. The way a viscoelastic solid completely recovers is shown in Figure 2.6 (d). In comparison a viscoelastic fluid, see Figure 2.6 (c), a residual strain will remain in the material and complete recovery will never be attained. The characteristic time τ of the exponential recovery curve $\varepsilon \sim \exp(-t/\tau)$ of soft tissue lies between milliseconds and seconds (Fung, 1993; Kauer, 2001). Since soft tissue does not exhibit long time history, the viscoelastic phenomena is sometimes ignored especially when 'long term" prediction (i.e., $t > \tau_{max} = 10\ s$) is involved.

Hyperelasticity is a property that was previously used to define rubbers and elastomers. Such materials experience large elastic strain that is recoverable. Recently it is being used for the development of constitutive equations of brain. Researchers (Ommaya, 1968; Galford and McElhaney, 1970; Shuck and Advani, 1972; Mendis et al., 1995; Bilston et al., 2001; Miller and Chinzei, 1997, 2002; Prange and Margulies, 2002; Wu et al 2004; Brands et al 2004) have been involved into several in-vivo and in-vitro experiments on soft tissues. Some of their recent works (Miller and Chinzei, 1997, 2002; Prange and Margulies, 2002; Wu et al 2004; Brands et al 2004) show that brain and other soft tissues that do not bear mechanical load can be best modeled with a

homogeneous *hyperviscoelastic*[8] material. Recent study of Prange and Margulies (2002) contradicts with the previous assumption on homogeneity and directional isotropy, even though full specification and features are still unknown. These issues will be discussed in detailed in the next chapter. In this study material properties of brain tissue have been assumed as hyperviscoelastic where exist a store energy function such that

$$\sigma(\varepsilon) = \frac{\partial W}{\partial \varepsilon} \tag{2.1}$$

Various complicated forms of energy function W (such as quasi-linear, hyperviscoelastic constitutive laws), first proposed for biological tissues by Fung in 1981. Among the several particular forms, polynomial form of strain energy potential with time dependent coefficients has been used in this analysis.

2.2.6 Incompressibility

A material is called incompressible if its volume remains unchanged by the deformation. Poission's Ratio of truly incompressible solid is considered as 0.5. However, soft tissues can be considered as a composite material that consists of both incompressible and compressible ingredients. Tissues with low water proportion are assumed quasi-incompressible. However, tissues with high proportion of water are usually modeled as incompressible materials. In this work brain tissue has been considered as nearly incompressible solid (Poission's ratio 0.45)

[8] Detailed description with mathematical formulation is given in section 2.3.5 of this dissertation.

In Table 2.1, the material properties of soft tissue in conjunction with their relevancy for the modeling of brain tissue are summarized. Comprising this information, brain tissue can be approximated as *piece-wise (structure-wise) homogeneous, isotropic, incompressible nonlinear hyperviscoelastic elastic* solid.

Table 2-1 Relevancy of general material properties for quasi-static tissue modeling

Property	**Modeling assumption**
non-homogeneity	Piecewise (structure wise) homogeneous approximation assumed
anisotropy	Isotropic (structure wise) approximation assumed
nonlinear elasticity	Basic continuum property (Hyperviscoelastic, polynomial form)
plasticity	Short term prediction and large deformations only
compressibility	Nearly incompressibility assumed

2.3 Continuum Mechanics: Analysis of Deformation, Strain and Stress

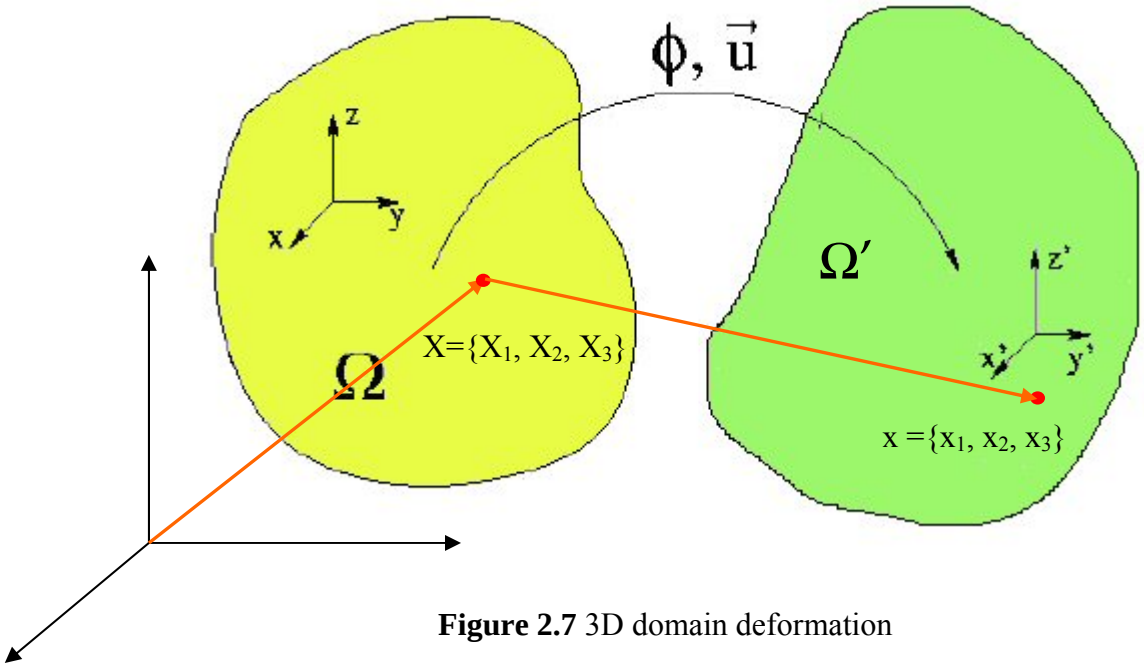

Figure 2.7 3D domain deformation

2.3.1 Basics on Continuum Mechanics

Apart from the tissue specimen considered, the mechanical behavior of biological tissues is uniquely characterized by their constitutive behavior, i.e. the relationship between externally applied loads like, e.g., pressure forces, and the resulting deformation. To analyze such situations we need thorough knowledge on the basics of continuum mechanics.

In this section, we will describe the basic mathematical definitions of elasticity theory. In elasticity theory, physical bodies are described as continua. Under the impact of external forces, physical bodies are deformed, which means that they change both their shape and volume. Let $\Omega \subset \Re^3$ be a domain representing the volume occupied by a body before the deformation. The state of a body associated with such "undeformed" domain is called the *reference configuration.*

In this analysis we assume that all particles are in their motion, i.e., from original to the final configuration of the body, which means that the Lagrangian formulation of the problem of large deformation is adopted. The fundamental difficulty in the general treatment of large deformation problem in solid mechanics is that the current configuration of a body is not known. This is an important difference when compared with linear analysis, in which it is assumed that displacements are infinitesimally small and therefore configuration of the body does not change. In fact in case of nonlinearity, the configuration of the body does change continuously; and such situation is dealt quite efficiently by using appropriate laws to measure stress-strain and constructing other constitutive relations.

Let us assume for the initial undeformed configuration, the coordinates of the points of a body are X= $\{X_1, X_2, X_3\}$. In the current or deformed configuration these points have new positions denoted by x = $\{x_1, x_2, x_3\}$. The notion of displacements is similar to that for coordinates: u = $\{u_1, u_2, u_3\}$ = x-X.

A basic tensoral quantity describing deformation of a body is a deformation gradient :

$$F_{ij} = x,^{i}_{j} \tag{2.2}$$

where F is deformation gradient and comma indicates covariant differentiation with respect to the undeformed configuration.

Left Cauchy –Green strain tensor[9] is given by :

$$B = FF^{T} \tag{2.3}$$

where T denotes a transposed matrix.

The right Cauchy-Green strain tensor is given by:

$$C = F^{T}F \tag{2.4}$$

---

[9] *Strain Tensor*: A strain tensor defines the body changes from initial to current configuration. It measures the change of an infinitesimal line and angles, when the body moves from the initial to current one. Two kinds of strain tensors have been defined and discussed: the Cauchy-Green (also called Lagrangian) and the Almansi (also known as Eulerian), relating to the initial and current configuration, respectively.

The Green-Lagrange (Cauchy-Green) strain tensor, measured with respect to undeformed configuration is given by:

$$E = \frac{1}{2}(C - I) \tag{2.5}$$

where I is the Identity matrix in Cartesian coordinates.

The Almansi strain tensor measured with current configuration is:

$$e = F^T EF \tag{2.6}$$

Each of the above strain measures should be used with appropriate and corresponding stress measures[10]. Cauchy stress (true stress), usually defined by τ, is measured with respect to the deformed (current) configuration. It is used together with Almansi strain, which as explained previously, is also measured with respect to deformed configuration. Cauchy stress and Almansi strain are energetically conjugate and therefore can be used to express virtual work as well as to develop constitutive relations for nonlinearity analysis (Zahavi, 1993; Miller, 2002;).

The Lagrange Stress or first Piola-Kirchhoff's stress tensor is defined as:

---

[10] Stress is normally defined as an internal force per unit area of a section in a body under loading. In linear static deformation it is assumed bodies undergoing small deformation. In nonlinearity analysis, we are concerned with the bodies where deformation caused by loading results in large deformation. To analyze such situation, two kinds of stress tensors are considered: the Cauchy (or true) stress tensor and the Piola stress tensors. The former refers to the current configuration, while the later refers to the initial condition.

$$S^{1p} = (\det F)\tau F^{-T} \tag{2.7}$$

It is energetically conjugate to Cauchy-Green strain tensor. But this stress tensor is not symmetric by definition, and therefore is not popular among the researchers. Thus a second Piola stress tensor is introduced, which is symmetric:

$$\overline{S}^{p} = (\det F)F^{-1}\tau F^{-T} \tag{2.8}$$

Since both the Piola stress tensors correlate the vector traction with the area of initial configuration, when the accuracy is required, the Cauchy stress tensor is more preferable, as it can relate to current configuration and therefore represents the true stress. There are two approaches to derive the constitutive equations for determining true stress: Cauchy method and Green method. The Cauchy method postulates the existence of laws that directly links the stress and strain tensors. Because the deformation process under consideration is very slow here, the dynamic phenomenon is neglected. The method assumes complete reversibility; i.e. after unloading, the body returns to its original shape. The Green method, on the other hand is based on energy potential. It postulates the existence of a potential energy function, defining stresses as derivatives. This method also assumes that there is no energy loss during loading and unloading path. The work done by external forces is completely converted into strain energy and is fully restored after unloading. The following sections discuss the two methods in mathematical terms.

2.3.2 Cauchy Method

In Cauchy approach, the stress tensor is expressed as a function the deformation tensor:

$$S = f(D) \tag{2.9}$$

where D denotes the deformation tensor. The above can be expanded in a polynomial series

$$S = a_0 I + a_1 D + a_2 D^2 + a_3 D^3 + ... \tag{2.10}$$

where coefficients a_k are function of invariants of tensor D. According to Cayley-Hamilton theorem, tensor D must satisfy its own characteristic equation (Zahavi, 1993); i.e :

$$D^3 - I_1 \times D^2 + I_2 \times D - I_3 \times I = 0 \tag{2.11}$$

Consequently, powers of tensor D those are higher than 2 can be expressed in terms of D and D^2. Thus the stress tensor may be represented as a quadratic function of deformation tensor D and its invariants.

$$S = b_0(I_1, I_2, I_3)I + b_1(I_1, I_2, I_3)D + b_2(I_1, I_2, I_3)D^2 \tag{2.12}$$

For the Cartesian coordinate system, the above equation can be represented as:

$$S = \chi_0(\lambda_1, \lambda_2, \lambda_3)I + \chi_1(\lambda_1, \lambda_2, \lambda_3)V + \chi_2(\lambda_1, \lambda_2, \lambda_3)V^2 \tag{2.13}$$

where λ is the right stretch tensor, and $\lambda_1, \lambda_2, \lambda_3$ are its *principal values*[11].

2.3.3 Green Method

Green's approach postulates the existence of potential strain energy of the deformed body. Let W be the strain energy $W = W(\varepsilon)$, where ε denotes a strain tensor and the strain energy W is measured per unit volume of the body. Then the stress tensor equals

$$S = \frac{\partial W}{\partial \varepsilon} \tag{2.14}$$

For (structure-wise) homogeneous and isotropic materials, the specific strain energy does not depend upon position, the strain energy becomes a function of the invariants of the strain tensor only.

$$W = W(I_1, I_2, I_3) \tag{2.15}$$

A detailed discussion on the adopted functions of the potential energy has been provided by Truesdell and Noll (1965). Readers may also referred to ABAQUS (2001) and ANSYS (2004) documentation. In this work *polynomial form* of strain energy function has been used which is discussed in detail in later section for *hyperviscoelastic* modeling.

---

[11] For a symmetric tensor, principal values of the tensor are the roots of polynomial equation following its determinants equal to zero.

2.3.4 Elasticity Laws for Linear Elastic Model

The discretization of Physcics-based modeling problems using the Finite Element (FE) Method became popular in late eighties and early nineties more and for various applications such as surgical simulation and surgical planning (Delinguette, 1998; Skrinjar et al., 1998; Paulsen et al., 1999), because soft tissue deformation was approximated using linear elasticity. The FE method, in conjunction with an elastic deformation model, is chosen for its reliable behavior and accuracy as compared to simpler analogies such as mass-spring models (e.g. Gibson ,1997) and models only computing the deformation at the surface (e.g. Bro-Nielsen,1997). Therefore, for the purpose of tracking and characterizing of brain shift, FE modeling of linear elasticity is still preferred over other models, as it can reflect and characterize the deformations without introducing much complexity. The algorithm is fully described in (Ferrant, 2001b)

2.3.4.1 Mathematical formulation

Assuming a linear elastic continuum with no initial stresses or strains, the deformation energy of an elastic body submitted to externally applied forces can be expressed as (Zienkiewicz and Taylor, 1987)

$$E(u) = \frac{1}{2}\int_{\Omega} \sigma^T \varepsilon d\Omega + \int_{\Omega} u^T F d\Omega \qquad (2.16)$$

where the variables are given in terms of the stress vector (σ), strain vector (ε), the forces $F = F(x, y, z)$ applied to the elastic body (forces per unit volume, surface forces or forces concentrated at the nodes), and $u = (u(x, y, z), v(x, y, z), w(x, y, z))^T$,

the displacement vector field which is to be computed. Assuming small deformation the strain vector ε is given by:

$$\varepsilon = \left(\frac{\partial u}{\partial x}, \frac{\partial v}{\partial y}, \frac{\partial w}{\partial z}, \frac{\partial u}{\partial y} + \frac{\partial v}{\partial x}, \frac{\partial v}{\partial z} + \frac{\partial w}{\partial y}, \frac{\partial w}{\partial x} + \frac{\partial u}{\partial z} \right)^T \tag{2.17}$$

which can be written as $\varepsilon = Lu$ where L is a linear operator. In case of linear elasticity, σ the stress tensor, can be linked to the strain tensor by constitutive equations of the material by generalized Hooke's law:

$$\sigma = (\sigma_x, \sigma_y, \sigma_z, \tau_{xy}, \tau_{yz}, \tau_{zx})^T = \mathbf{D}\,\varepsilon \tag{2.18}$$

where D is the elasticity matrix characterizing the properties of the material. The matrix is symmetric, this stems from the symmetry of the stress and strain tensors (Zienkiewicz and Taylor, 1987, page 51); thus there are 21 elastic constants for a general anisotropic material.

In the case of an orthotropic material, the material has three mutually perpendicular planes of elastic symmetry (Ting, 1996). The elasticity matrix then becomes:

$$D = \frac{1}{\Delta} \begin{pmatrix} \frac{1-\nu_{zy}\nu_{yz}}{E_y E_z} & \frac{\nu_{yx}+\nu_{zx}\nu_{yz}}{E_y E_z} & \frac{\nu_{zx}+\nu_{zy}\nu_{yx}}{E_y E_z} & 0 & 0 & 0 \\ . & \frac{1-\nu_{zx}\nu_{xz}}{E_x E_y} & \frac{\nu_{zy}+\nu_{xy}\nu_{zx}}{E_y E_z} & 0 & 0 & 0 \\ . & . & \frac{1-\nu_{xy}\nu_{yx}}{E_y E_x} & 0 & 0 & 0 \\ . & . & . & G_{xy}\Delta & 0 & 0 \\ . & . & . & . & G_{yz}\Delta & 0 \\ . & . & . & . & . & G_{zx}\Delta \end{pmatrix} \tag{2.19}$$

where

$$\Delta = \frac{1 - \nu_{xy}\nu_{yz} - \nu_{yz}\nu_{zy} - \nu_{zx}\nu_{xz} - \nu_{xy}\nu_{yz}\nu_{zx} - \nu_{yx}\nu_{zy}vxz}{E_x E_y E_z} \tag{2.20}$$

Assuming isotropic material properties for each point, the elasticity matrix has the following symmetric form:

$$D = \frac{E(1-\nu)}{(1+\nu)(1-2\nu)} \begin{pmatrix} 1 & \frac{\nu}{1-\nu} & \frac{\nu}{1-\nu} & 0 & 0 & 0 \\ . & 1 & \frac{\nu}{1-\nu} & 0 & 0 & 0 \\ . & . & 1 & 0 & 0 & 0 \\ . & . & . & \frac{1-2\nu}{2(1-\nu)} & 0 & 0 \\ . & . & . & . & \frac{1-2\nu}{2(1-\nu)} & 0 \\ . & . & . & . & . & \frac{1-2\nu}{2(1-\nu)} \end{pmatrix} \tag{2.21}$$

where Young's modulus E and Poisson's ratio ν are the same in any direction: $E = E_x = E_y = E_z$; and $\nu = \nu_{xy} = \nu_{xz} = \nu_{yz}$. There are no independent shear moduli, as the material parameters are the in same every direction.

For discretization, finite element method is applied over the volumetric image domain so that the total potential energy can be written as a sum of potential energies for each element $E(u) = \sum_{e=1}^{N_{nodes}} E^e(u^e)$. If the mesh is composed of simple tetrahedral elements, each element can be defined by four mesh nodes. The continuous displacement field u everywhere within the element *e* of the mesh is defined as a function of displacement at the element's nodes u_i^e weighted by the element's interpolating functions $N_i^e(x)$

$$u(x) = \sum_{i=1}^{N_{nodes}} IN_i^e(x) u_i^e \tag{2.22}$$

The linear interpolating (shape) functions are used to define the displacement field inside each element. The interpolating function of node *i* of element *e* is defined as:

$$N_i^e = K(a_i^e + b_i^e x + c_i^e y + d_i^e z) \tag{2.23}$$

where $K = \frac{1}{6V^e}$ for a tetrahedron, and $K = \frac{1}{2S^e}$ for a triangle. The computation of volume V^e and surface S^e of e and the interpolation coefficients are detailed by Zienkiewicz and Taylor (1987)

The volumetric deformation of the brain is found by solving the displacement field that minimizes the deformation energy by equation (2.16). For the finite element approach this is described by:

$$\delta E(u) = \sum \delta E^e(u^e) = 0 \tag{2.24}$$

where

$$\delta E^e(u^e) = \sum_{i=1}^{N_{nodes}} \frac{\partial}{\partial u_i^e} E^e(u^e)\delta u_i^e + \sum_{i=1}^{N} \frac{\partial}{\partial v_i^e} E^e(u^e)\delta v_i^e + \sum_{i=1}^{N} \frac{\partial}{\partial w_i^e} E^e(u^e)\delta w_i^e, \tag{2.25}$$

Since δu_i^e, δv_i^e and δw_i^e are independent, defining matrix $B^e = (B_i^e)_{i=1}^{N_{nodes}}$ with $B_i^e = LN_i^e$ for every node *i* of each element *e*, yields in the following equation:

$$0 = \int_\Omega B^{eT} D B^e u^e d\Omega - \int N^{eT} F^e d\Omega \tag{2.26}$$

with the element stiffness matrix $K^e = \int_\Omega B^{eT} D B^e d\Omega$. An assembly of the equations for all elements finally leads to global linear system of equations, which can be solved for the displacements resulting from the forces applied to the body:

$$Ku = F$$

The solution of which will provide us with the deformation field corresponding to the global minimum of the total deformation energy.

Above are the constitutive equations that model surfaces as elastic membranes and volumes as elastic bodies. Given externally applied forces F to a discretized body characterized by a rigidity matrix K, solving Equation (2.27) provides resulting displacements.

2.3.5 Hyperviscoelastic Model

In nonrigid registration, mathematical formulation described similar to above is typically used in linear elastic models (Ferrant et al, 1999, 2001b; Hagemann et al, 1999, Warfield et al. 2002). In this formulation, the brain deformations are regarded as infinitesimal (i.e. geometric linearity) and brain tissue is treated as an elastic material in which the stress is a linear function of the strain (i.e. material linearity). Although nonrigid registration using linear biomechanical models has contributed significantly in the research of biomechanics (Ferrant, 2001b) and intraoperative imaging analysis (Warfield et al, 2002), it must be realized that neither the assumption about infinitesimally small brain deformation nor the one about brain stress-strain linear behavior is valid during brain shift. For example, Craniotomy[12] typically results in deformation of brain surface is claimed as approximately 10 mm (i.e. around 10% of distance between the left and right cortical landmarks) and rigid body movement of the

[12] Craniotomy: Surgical incision into the skull.

brain (Miga et al, 2003), which implies that fully nonlinear finite element formulations and material models are more suitable for predicting deformation within the brain during a typical brain shift scenario.

Therefore, image analysis techniques should be complemented by biomechanical models based on nonlinear finite element formulations rather than linear ones that has been previously used. It can be demonstrated that such nonlinear models facilitate accurate prediction of deformation field within the brain even when simplified brain geometry and limited data about the brain surface deformation are used. Research shows that brain tissue can be best modeled with a homogeneous hyper viscoelastic material (Figure 2.8).

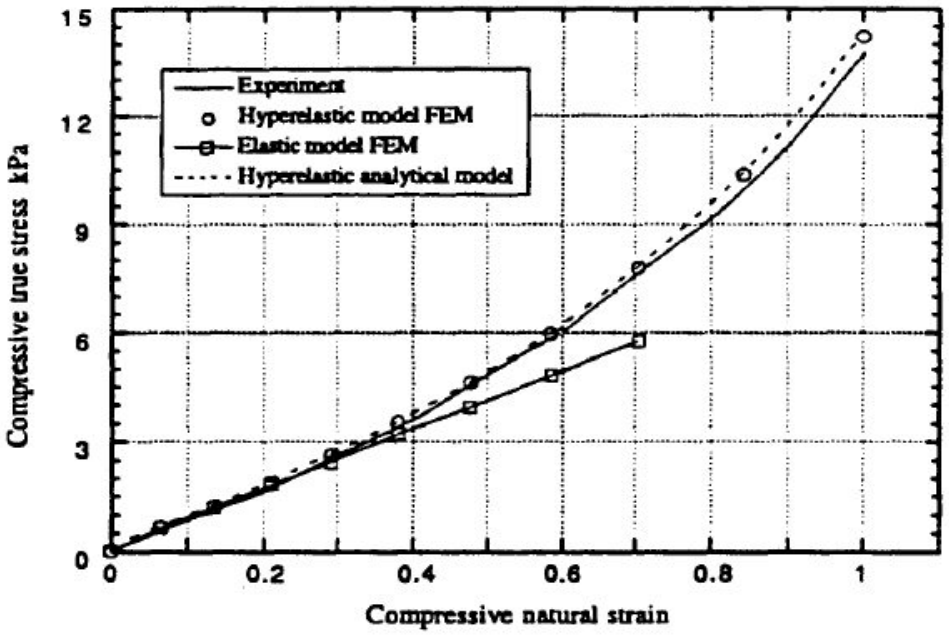

Figure 2.8 Hyperviscoelastic constitutive model gives better approximation of experimental data compared to linear elastic one (Darvish, 2000)

2.3.5.1 Mathematical formulation

In a hyperviscoelastic material, stress is calculated from a strain energy function. The brain, which is believed to behave as almost incompressible, follows the following formula to exhibit large deformation (Bathe, 1996; Zienkiewicz and Taylor, 1987).

$$ {}_0^t\overline{S}_{ij} = \frac{\partial_0^t \overline{W}}{\partial_0^t \varepsilon_{ij}} \tag{2.27} $$

Here ${}_0^t\overline{S}_{ij}$ and ${}_0^t\varepsilon_{rs}$ are the components of the second Piola-Kirchhoff stress and Green-Lagrange strain tensors; ${}_0^tC_{ijrs}$ are the components of constant elasticity tensor. A simple and widely used elastic material description for large deformation analysis is obtained by generalizing the linear elastic relation in the following fashion:

$$ {}_0^t\overline{S}_{ij} = {}_0^tC_{ijrs}\, {}_0^t\varepsilon_{rs} \tag{2.28} $$

Considering three-dimensional stress conditions, we have:

$$ {}_0^tC_{ijrs} = \lambda\delta_{ij}\delta_{rs} + \mu(\delta_{ir}\delta_{js} + \delta_{is}\delta_{jr}) \tag{2.29} $$

where, λ and μ (shear modulus G) are the Lamé constants and δ_{ij} is the Kronecker delta,

$$ \lambda = \frac{E\nu}{(1+\nu)(1-2\nu)}; \qquad \mu = \frac{E}{2(1+\nu)} \tag{2.30} $$

The above formulation assumes linearity and is valid for only undeformed initial state; hence, the constitutive model used in the study is linear in parameters describing instantaneous response of the material. For example, the shear modulus from above equation gives instantaneous value, μ_0. The time dependent formulation is obtained assuming hyperviscoelasticity (Miller, 2002a):

$$\mu = \mu_0[1 - \sum_{k=1}^{n} g_k (1 - e^{-t/\tau_k}) \tag{2.31}$$

The material response in *ANSYS* hyperelastic models is always assumed to be isotropic and isothermal. From the *Green method* (discussed in section 2.3.2) the strain energy is a function of the invariants of the strain tensors:

$$W = W(\bar{I}_1, \bar{I}_2, \bar{I}_3)$$

The hyperelastic materials are also assumed to be nearly or purely incompressible, for which the volume is considered to be remaining constant during deformation (Zahavi and Barlam, 2000). Hence, the strain energy is a function of two invariants only:

$$W = W(\bar{I}_1, \bar{I}_2)$$

The simplest and typical example of the above form is Moony material (Zahavi and Barlam, 2000). In this dissertation, a polynomial form of strain energy potential has been used[13].

---

[13] There are some other mathematical forms such as the Ogden form; the Mooney-Rivlin form, Yeoh form, the Arruda-Boyce form and the Van der Waals form are available. Detailed mathematical description of each model is out of scope of this dissertation. For detailed formulation kindly refer to ABAQUS (2001) and ANSYS (2004).

$$ {}^{t}_{0}\overline{W} = \sum_{i+j=1}^{N} C_{ij}(\bar{I}_1 - 3)^i(\bar{I}_2 - 3)^j + \sum_{i-1}^{N}(\frac{1}{D_i})(J-1)^{2i} \tag{2.32} $$

where, C_{ij} and D_i are material parameters; J is the determinant of the elastic deformation gradient F, $\bar{I}_1$ and $\bar{I}_2$ are first and second deviatoric strain invariants, respectively.

From equation (2.32), the Neo-Hookean model can be obtained by setting N = 1 and $C_{01} = 0$. Also for N = 1, the two parameters Mooney-Rivlin model is obtained, for N = 2, the five parameters Mooney-Rivlin model is obtained and for N = 3, the nine parameters Mooney-Rivlin model is obtained (ABAQUS, 2001). The initial shear modulus is defined as:

$$ \mu_0 = 2(C_{10} + C_{01}) \tag{2.33} $$

The initial bulk modulus is:

$$ K = 2/d_1 \tag{2.34} $$

The displacement within each element can be linked to the nodal displacements through its associated shape functions. The first order hyperelastic polynomial coefficients are chosen between the ranges, which are suitable for slow and moderate strain rate (approximately between $0.001s^{-1}$ – $1.0s^{-1}$), typical case for neurosurgical scenario.

Theoretical materials with a Poisson's ratio of exactly 0.5 are truly incompressible (ABAQUS, 2001; ANSYS, 2004). Since we assume brain tissue is nearly

incompressible, we fixed the value at 0.45 that matches with most of the resent research. The Lamé constants G and λ with the standard relations to the instantaneous Young's modulus E is determined. The first order hyperelastic polynomial coefficients are considered to be equal [$\frac{C_{01}}{C_{10}} = 1$ and $\frac{C_{02}}{C_{20}} = 1$] in the previous study (Miller, 1999). However, it is to be noted that such assumption is equivalent to assuming the equality of the energy of reciprocal deformation to that of the original one. In reality, the stiffness in compression for the brain tissue is higher than extension reported in literature (Miller, 2002b). The regional and directional differences in the shear modulus of gray matter further confirms the presence of tissue heterogeneity within the brain (Prange and Margulies, 2002; Coats and Margulies, 2005). Thus the values of polynomial coefficients need to be readjusted. In order to determine the effect of the ratio between C_{10} and C_{01} on the stress response at large strains, a parametric study can be conducted on cylindrical specimens. The following equation has been suggested for the analysis (Mendis, 1992):

$$\sigma = \frac{F}{A} = 2C_{10}\{\lambda_1^2 - \frac{1}{\lambda_1}\} + 2C_{01}\{\lambda_1 - \frac{1}{\lambda_1^2}\} \tag{2.35}$$

where λ_1 is the principal stretch ratio in the direction of the axis of the cylinder. The parametric study can be performed by evaluating the above equation (2.35), for five different ratios of C_{10} and C_{01} while keeping their sum constant. This constant value is chosen to be comparable to the small strain instantaneous Young's modulus of brain tissue as given by $E_0 = \frac{d\sigma}{d\lambda_1}|_{\lambda=1} = 6(C_{10} + C_{01})$. The same expression can be achieved by combining equations (2.30) and (2.33). These equations will be useful in brain deformation analysis described in later chapters.

2.4 Summary of the chapter

This chapter describes the basic background of biomechanics and soft tissue modeling. A brief introduction of continuum mechanics is also provided. Some important mathematical formulation of hyperviscoelastic modeling has also been deduced. The next chapter will be dealing with various biomechanical models and modeling issues.

Chapter 3

BACKGROUND STUDY OF BIOMECHANICAL MODELS AND MODELING ISSUES

3.1 Biomechanical Models for deformable objects

Biomechanical modeling[14] of deformable objects has a pretty long history. Historically deformable models appeared in computer graphics and were used to edit complex curves, surfaces and/or solids. In image analysis in particular, deformable models were used for fitting curved surfaces, boundary smoothing, image segmentation and registration. In later years deformable models played a major role in computer industry especially in character animation, cartoon, computer graphics and realistic simulation of skin, clothing and human or animal characters. Deformable models were being used by CAD/CAM sector to simulate the deformation of industrial materials such as metal forming and plastic molding. There has recently been particular interest in the use of biomechanical models to predict soft tissue deformation and to address the demand of realistic modeling of complex tissue behavior during image-guided surgery (computer assisted surgery).

Biomechanical models can be either *physical* or *nonphysical* in nature. Models that are based on solving continuum mechanics problems under consideration of

[14] *Biomechanics:* Here the term biomechanics refers to the area of research that deals with mechanics of biological tissue and structures. *Biomechanical Model:* The study of the mechanics of a living body, especially of the forces/stress exerted by muscles and gravity on the external structure like skeleton or internal organ like brain, liver in surgical condition etc.

material properties, boundary constrains etc. are called physical model (or physics-based model). All other modeling techniques are non-physical model, even if they may have physics or mathematical formulation. Spline technique (Bartels et al, 1987; Bookstein, 1989; Rohr, 1996) and Free-form deformation (Barr AH, 1984; Chang and Rockwood, 1994; Coquillart,1990) are two widely used examples of non-physical modeling technique.

Terzopoulos is one of the pioneers who introduced physically based modeling for the simulation of deformable objects (Terzopoulos et al, 1987). One of the most widely used physical methods has been the *spring–mass* model that represented a system consisting of various nodes connected by elastic links (Cover et al, 1993; Lee et al, 1995; Bucholz et al, 1997). However these types of models do not incorporate real material parameters and hence are very weekly related to the physical biomechanical behavior of soft tissues. Most recent PB models have applied Finite Element Method (FEM) – a numerical solution technique that has already shown great power and promise for the solution of partial differential equations in solid mechanics. An alternative approach used to solve the PDEs in continuum mechanics (biomechanical modeling) is the boundary element method (BEM) (Brebbia CA et al, 1984) or Finite difference method (Sarti et al, 1999). Nevertheless, among the all other methods in physics-based modeling, FE method stays as the ultimate "state of art" technique. The FEM is found superior to all previously mentioned techniques while an accurate solution of continuum mechanics problem with the complex geometry is under concern (Gladilin, 2003). The next chapter will address all the important issues related to FEM modeling in a greater detail. Here we will mainly discuss historical advancement and outline of the basic

contribution of physics-based (biomechanical) soft tissue modeling in medical and bioengineering sector.

3.2 Previous Research on Biomechanical modeling

In the past, a variety of different biomechanical models for intraoperative image correction purposes have been proposed. Additionally, other biomechanical models have been developed in different contexts like car crash, fall, sports and other impact analysis or surgery simulation, but most of them are applicable for image correction purposes, too. In nineties, the earliest of such biomechanical models in the field of medical image analysis has been proposed (Tada et al, 1994; Takizawa et al, 1994). Other approaches based on e.g, mass-spring-system (Bucholz, 1997) was introduced for either surgical planning or intraoperative image correction purposes. Slightly different approach was proposed by Edwards et al. (1997, 1998) used to set combined energy terms and minimized the spatial discrepancy between given land mark positions in the preoperative human head data and their current position while satisfying some prior given geometry constraints like, e.g., area preservation constraints. It has to be mentioned that all these models do not incorporate real physical parameters and hence are weakly related to the physical behavior of biological soft tissue (Delingette, 1998).

Some physical deformation models have been proposed to constrain a deformation field computed from image data using elastic (Bajcsy and Kovacic, 1989; Ferrant et al., 1999) or even viscous fluid deformation models (Christensen et al., 1997; Bro-Nielsen and Gramkow, 1996). However, many of these models do not account for the actual material characteristics of the objects depicted in the images, because the

matching is done by minimizing an energy measure that consists of a weighted sum of an image similarity term and a relaxation term representing the potential energy of a physical body (e.g. elastic). Therefore, the actual biomechanics of the phenomenon cannot be properly captured by these models, and the physical model simply acts as a regularization constraint on the image similarity criterion.

Other authors have proposed to use deformable surface models in conjunction with a physics-based model to infer a volumetric deformation field from surface-based deformations [e.g. Davatzikos (1997); Thompson and Toga (1996)]. But the used parameters in the physics-based volumetric models were determined heuristically, and one may not get the necessary information generated by the model to extract biomechanical properties.

The issue of whether deformations could be calculated within surgical time frames was successfully addressed by Warfield et al. (Warfield et al, 2002). However, only visual inspection was used to determine that the registration process. Xu and Nowinski (2001) applied small strain, large deformation theory (metal forming principle) to the problem of brain atlas registration. The work of this group also focuses on a nonrigid matching procedure based on the finite element method.

The cardiac image analysis community has also been using physics-based models - mainly FE models, but they deform them with image-derived forces. These models then provided quantitative and physically interpretable 3D deformation estimates from image data. Papademetris et al. (1999b) derived the forces applied to the FE model from ultrasound (US) images using deformable contours using a shape-tracking

algorithm. Metaxas (1997) derives the forces from MRI data for the motion analysis of the left or right ventricle (Park et al., 1996; Haber et al., 1998). These approaches are very interesting in a sense that a generic parameterized FE model is usually fit onto the image sequence before doing the analysis.

Biomechanical models have been explicitly proposed recently to constrain the registration of images (Kyriacou et al, 1999; Hagemann et al, 1999) in the context of deformable brain registration. Hagemann et al. (1999) used a biomechanical model to register brain images showing deformations due to neurosurgical operations. The model is deformed by enforcing correspondences between landmark contours manually or semi-automatically. The constitutive equations of the biomechanical model are discretized using finite elements, and the basic elements of the mesh are the pixels of the image, which causes the computations to be particularly heavy. Kyriacou et al. (1999) studied the effect of tumor growth in brain images. They used a FE model and apply concentric forces to the tumor boundary to shrink it. The drawback of such methods is that they require user intervention to compute the forces (or correspondences) applied to the model, hence the method is not fully automated. Again, these methods have only been applied to 2D images thereby limiting the realistic clinical study and accuracy.

In the context of brain shift analysis, there has been a significant amount of work directed towards simulation using models driven by physics-based forces such as gravity. Skrinjar and Duncan (1999) propose a model consisting of mass nodes

interconnected by Kelvin models[15] to simulate the behavior of brain tissue under gravity, with boundary conditions to model the interaction of the brain with the skull. Some authors (Paulsen et al., 1999; Miga et al., 1999b, 2000a) proposed a Finite Element (FE) model based on consolidation theory[16] where the brain is modeled as an elastic body with an interstiticial fluid. They also used gravity induced forces, as well as experimentally determined boundary conditions. Most of researchers (Kyriacou et al. 1999; Takizawa et al. 1994; Skrinjar et al, 1999) at that time applying the FEM to CAS have focused on linear-elastic models of the brain, which would benefit from computational simplicity and therefore were relatively quick to solve. Ferrant et al. (1999, 2001b) also assumed linear elastic body and applied finite element method to solve the equilibrium equations. His result is remarkably similar[17] to Skrinjar et al (1999) given the significantly different boundary conditions used. Clatz et al. (2003) also used a linear elastic model in order to predict the *gravity-induced deformation*[18] of the brain based on the cerebral spinal fluid levels during long procedures to treat Parkinson's disease. The use of elastic models has been later extended by Hagemann

---

[15] A Kelvin model is a simplified mechanical model of viscosity and consists of a parallel connection of a linear spring and a dashpot.

[16] This representation considers brain as a porous solid saturated by a fluid, whose behavior is determined by changes in hydration. This brain-behavior can be represented by the consolidation model, which was originally developed in the field of soil mechanics (Terzaghi K, 1942).

[17] Ferrant et al. (1999, 2001a, 2001b) used a linear elastic FEM to infer a volumetric deformation field from surface deformations, based on intraoperative MR images acquired at several time points. The mean distance and standard deviation between the predicted and measured location of 400 landmarks was 0.9±0.7 mm.

[18] Brain shift in the direction of gravity.

et al (1999, 2001) who coupled elastic and fluid models to describe the behavior of solid tissue and cerebrospinal fluid.

Miller et al. (Miller, 1999, Miller and Chinzei, 2000) were the pioneers in introducing a non-linear viscoelastic model that claims to be suitable for surgical procedures. Unlike the previous models, Miller's model proposed constitutive equations of hyperviscoelasticity to account for the relationship between stress and strain rate. He and his collaborators (1999, 2000) carried out exceptional modeling work and presented simulations and comparisons with in-vivo experiments demonstrating that a hyperviscoelastic constitutive model can accurately reproduce brain deformation for compression levels reaching 30% and for loading velocities varying over five orders of magnitude. Wittek et al. (2004) used this non-linear material response function, and considered a fully non-linear FEM formulation appropriate for large deformations. They modeled the deformation a brain due to the load similar to the load exerted by the surgical tools driven approximately perpendicular to the surface of the brain. The calculated and measured reaction forces agree to around 20%.

Even though these models are very promising, it remains difficult to accurately estimate all the forces and boundary conditions that interact with the model, especially during the course of surgery. For instance, it is very difficult to model the shrinking of the lateral ventricles during brain shift. This phenomenon is probably due to a pressure change of the cerebrospinal fluid (CSF) inside the ventricles (A. Navabi et al., 2001), but it is extremely complicated to measure this pressure continuously during neurosurgery. Also, only the state of the brain before and after opening of the dura has been considered to be changed. So far, most of the proposed models, do not consider

the dynamic evolution of the shape of the brain during surgery. Two of the major causes of brain shift are gravity as cerebrospinal fluid is released, and forces imparted by surgical instruments. The majority of modeling studies have focused on predicting deformation prior to any resection or retraction. The modeling of cutting/sectioning a meshed brain is not straightforward within an FEM framework, because it introduces discontinuities which cannot be treated within elements. Furthermore, no attempt was given so far to build a meshed model from an anatomical atlas, thus a proper study of structural deformation of human brain is still rather incomplete. This leaves problems related to biomechanical modeling unaddressed and unsolved. A comprehensive review of biomechanical medical modeling for medical and bioengineering applications can be found in literatures (Metaxas, 1997; Hagemann, 2001).

3.3 Modeling Issues

The mechanical behavior of brain tissue was modeled in different ways based on the various assumptions and specific conditions of interest in biomechanics. Hence, different constitutive relations were obtained by various researchers for the same material depending on the particular condition. In a recent review article, Kyriacou et al. (2002) discussed important issues in brain biomechanical modeling for neurosurgery, and the paper compared various constitutive equations with each other. We will however, not focus on each and every aspect; rather restrict our discussion on major modeling issues and major area of dispute. Initial modeling issues encountered with various assumptions, such as whether the brain was to be considered as 1) elastic, viscoelastic or poroelastic, 2) compressible or incompressible, 3) fluidic or solid, 4) homogeneous or inhomogeneous 5) isotropic or anisotropic, 6) being affected by gravity and CSF submersion, or 7) being affected by friction etc.

3.3.1 Constitutive Tissue Property: Elastic, Viscoelastic or Poroelastic

The biomechanical models that have been developed so far to name few, *Viscoelastic* and *hyperviscoelastic* models (Wang and Wineman 1972; Mendis et al. 1995; Miller 1999), *Poroelastic* (Paulsen et al. 1999; Miga et al. 1999a, 1999b; Subramaniam et al. 1995; Kaczmarek et al. 1997; Pena et al. 1999; Nagashima et al. 1990; Tenti et al. 1999; Basser 1992) and purely *Elastic* (Kyriacou et al. 1999; Kyriacou and Davatzikos 1998; Takizawa et al. 1994; Ferrant et al. 2001a) etc are important advancements. The characteristic time scale is found as a very important phenomenon for choosing the material model. For example, Impact analysis on brain is usually modeled with viscoelasticity (Zhou et al. 1996; Brads et al. 2004), while long term processes like hydrocephalus can be modeled using poroelasticity (Zienkiewicz, 1987) or mixture theory (Kyriacou et al. 2002) due to the need to account for interstitial fluid movement. Recent study shows a biphasic hyperviscoelastic model has also been found suitable for modeling of hydrocephalus where a strain rate is very low (Miller, 2004).

3.3.2 Constitutive Tissue Modeling: Compressible or Incompressible

The issue of compressibility of brain was also in dispute and demanded careful investigation. Some of the researchers argue for incompressibility in impact situations while for compressibility for long duration processes (Kaczmarek et al. 1997). Saron et al (2000) suggest since fluid cavities allow movement of fluid and thus occurs apparent changes of local volume, it would be proper to consider brain as a compressible material. However, Miller and Chinzei (1997) did not find any apparent change in volume due to loading, all of their models related to brain biomechanics assume incompressibility to simulate the brain deformation. The poroelastic models (Miga, 2000, Paulsen 1999) by definition assume compressibility as the models allow fluid movements. Researchers also took initiative to measure Poission's ratio which is the index of compressibility.

Some groups (Tenti et al, 1999) used a linear poroelastic material to calculate a dry Poisson's ratio $\nu = 0.4$. Guillaume et al. (1997) found that $\nu = 0.35$ gives best agreement with hypergravity experiments on excised bovine brains. Miga et al. (1998) however did not seem to agree and they suggested an approximate value of $\nu = 0.45$ which represents brain as *nearly incompressible*[19] material. Most of the recent researchers assume brain as nearly incompressible (Poisson's ratio ranging from 0.45 to 0.49) due to its high water content and larger bulk modulus. However, rigorous experimental work in vitro or vivo is still needed to come to any definite conclusion on compressibility.

3.3.3 Constitutive Tissue Modeling: Fluidic or Solid

Bilston et al. (1997) and Shuck and Advani (1972) modeled brain tissue assuming it a fluid since they found lack of long term elastic modulus. On the contrary, Donnelly and Medige (1997) argue for need of a solid model. Since Shuck and Advani (1972) discuss yield properties[20] of brain tissue; this would strengthen the solid model theory since fluid models are not usually associated with yield. Another useful attempt of modeling for brain tissue was assuming it elastoplastic material. The argument was brain tissue behaved as an elastic solid when immersed in saline and as a fluid when out of it. Hagemann et al. (2001) tries to couple solid and fluid models to describe the behavior of brain as solid tissue and cerebrospinal fluid as liquid; Hooke's law is taken to represent the behavior of the solid material, whilst the Navier–Stokes law is used to represent the fluid.

---

[19] For truly incompressible material Poisson's ratio is exactly 0.5.

[20] The point at which material deforms permanently (plastically) is known as yield point.

3.3.4 Constitutive Tissue Property: (In)Homogeneity and (An)Isotropy

It is well recognized that biological tissues are anisotropic and inhomogeneous (Zhou, 1995), however most of the biomechanical models of brain considers homogeneity and isotropy assumption (see e.g. Pamidi and Advani, 1978; Walsh and Schettini, 1984; Sahay et al., 1992; Mendis et al., 1995; Miller and Chinzei, 1999; Miller and Chinzei, 2002b). The argument is given that in favor that very soft tissues like brain, kidney liver etc. do not bear mechanical loads thus they do not exhibit any directional structure. This assumption were put into doubt while recent in-vivo and in-vitro experimentation by Prange and Margulies (2002) reports anisotropic and inhomogeneity of brain tissue. Margulies and her collaborators (Prange and Margulies, 2002; Gefen and Margulies, 2004; Coats and Margulies et al 2005) found that the gray matter was in an average sense stiffer than the white matter (corona radiata and corpus callosum) by about 30% in fresh porcine brain tissue. In addition they found regional, directional age related dependency in brain tissue as well. This was contradictory to the finding of previous research that did not show any significant difference in elastic properties of white and gray matter (Bilston et al, 1997). Yet previously, Nagashima et al (1990) assumed a much stiffer (10-fold) gray matter without fully justifying their choice. Kaczmarek et al. (1997) used the same elastic properties for both white and gray matter, taken from the lowest strain tests performed by Metz et al. (1970). Ozawa et al. (2001) performed experiments on rabit spinal chord and showed no significant difference in stiffness between gray and white matter. However, King and his collaborators (Zhou et al, 1994, King et al 1995) used a 60% stiffer white matter due to its fibrous nature. Arbogast et al (1997) and Manduca et al (2001) also reported a stiffer white matter with average shear stiffness. There seems to be a need for further experimentation on this issue.

3.3.5 Effect of Gravity and CSF submersion

Normally the brain is considered to be submerged in CSF in physiological conditions, thus its weight is neutralized by the fluid pressures (buoyant force). However, during open skull surgery where loss of CSF seems to be the dominant factor inducing several millimeters of deformation mostly along the direction of gravity. So, the weight of brain tissue while modeling the experimentation for finding the material properties can be crucial in some cases.

3.3.6 Effect of Friction

Recently Wu et al (2004) argues that friction may play an important role in tissue modeling. The friction coefficient in particular at the contact interface between the specimens and platens is assumed to vary from 0.0 to 0.5. Their numerical simulations show that the tissue specimens are, due to the specimen/platen friction, not compressed in a uniform stress/strain state, as has been traditionally assumed in analytical analysis. Since this issue is ignored by most of the research papers, the stress levels of soft tissues can be overestimated by 10–50% in such cases and, consequently, most published data on soft tissues obtained in unconfined compression may not reflect their true mechanical properties. The common assumption of homogeneity and isotropy can also become invalid and measurement results misleading if friction factor is high. The problem was addressed is some recent literature on biomechanics (for e.g, Nasseri et al, 2003; Miller, 2005b). Friction may play a major role in brain– skull boundary conditions. In literature the brain–skull interface has been represented as tied (no brain–skull relative slip) or sliding (with or without friction, with or without brain–skull separation). But limited experimental data are currently available for specific validation. During actual friction coefficient measurements, friction is observed to be

sliding-speed-dependent (Wang and Ateshian, 1997; Wu et al, 2004): It increases with increasing sliding speed and stabilizes around a steady-state value. Friction may also a dominant role in modeling simulators for specific applications such as needle or electrode insertion in Deep Brain Stimulation (DBS).

3.4 Summary of the chapter

This chapter describes the research on various existing biomechanical models and modeling issues. The next chapter will be focusing on the construction of physics-based atlas, its validation and its various applications.

Chapter 4

CONSTRUCTION OF PHYSICS-BASED BRAIN ATLAS AND ITS APPLICATIONS

4.1 Physics-based Atlas

The human brain is the most complex organ in the known universe. For centuries its development, structure, function, and disease have been studied. Substantial energy and efforts are already spent to build various kinds of brain models. Numerous brain atlases have been developed capturing *anatomy* (Talairach and Tournoux et al, 1993; Nowinski et al, 1998a, 1998b; Nowinski et al, 2002a, 2002b; Nowinski et al, 2003a, 2003b, 2003c; Nowinski et al, 2004; Nowinski et al, 2005), *function* (Nowinski et al, 2001a, Nowinski et al, 2003c), and *vasculature* (Szikla et al., 1977; Nowinski et al, 2005). These atlases use various representations including bitmaps, contours, surfaces, and volumetric models. To our best knowledge, a physics-based atlas (PBA) of the human brain is not constructed yet (Roy et al, 2006a). As the usefulness of electronic brain atlases in medical research is growing, particularly in medical image analysis, human brain mapping, and disease study, in our opinion, to develop a volumetric biomechanical simulation and deformation 3D atlas model has become a necessity.

Incorporating physics-based (PB) techniques in anatomical discipline to build a 3D meshed model has become obligatory in today's research since PB methods have already made possible to address many difficult problems that were not possible with only geometrical and anatomical data. In opposed to purely geometric models,

physics-based models incorporate additional constraints (such as material properties) that are very useful in accurate modeling and simulation (Metaxas, 1997). Thus, the investigation of the material properties of the brain to construct an accurate PB model for deformation analysis is very crucial. We have selected an electronic brain atlas database named *Cerefy* Brain Atlas (see chapter 1) for the construction of a 3D human brain model for the investigation of biomechanics of the brain. The important factors that influenced us to choose this particular atlas were its use in clinical, research and educational practice. The main objective of this chapter is to introduce a framework of physics-based modeling that will enable to compute brain deformations. The FEM Brain model has been developed based on the assumption of large deformation of non-linear hyperviscoelastic material with quasi-static behavior (Roy et al, 2004a, 2004b, 2005b, 2006a; Miller, 2002a). A nearly incompressible material behavior is assumed for the brain tissue as the bulk modulus of the brain has been found about 10^6 times higher than the shear modulus (Brands et al, 2004). 10-node parabolic (quadratic) elements are used in tetrahedral mesh generation as they yield better mathematical approximations and better-curved boundaries compared to linear ones.

The developed physics-based model has several advantages over the other existing ones. A key advantage is it has detailed 43 sub-cortical structures, cortical regions and brain connections having highest level of anatomic parcellation[21]. The model preserves salient anatomical information and employs a non-linear hyperviscoelastic material property of the brain tissue typically suited for surgery simulation. Therefore, the model offers a more accurate prediction of deformation of each structure as well as

[21] Comparing with other existing model such as Wayne State Brain Injury Model (WSUBIM) that has only 7 subcortical meshed structures.

the entire brain during neurosurgical interaction. In contrary to the previous efforts motivated mainly by traumatic injury prevention, e.g. fall, sports and automotive accident (Ruan et al, 1994b; King et al, 1995; Zhou et al, 1996; Mendis et al, 1995; Al-Bsharat et al, 1999; Brands et al, 2004) requiring investigation of a very fast strain rate, we focus primary on a closer examination of mechanical properties of brain tissue at moderate and low strain rates relevant to surgical procedures. The method can be further extended to model various structural diseases such as hydrocephalus and tumor growth or tumor shrinkage due to radiotherapy. The complete flowchart of the PBA is illustrated in Figure 4.1.

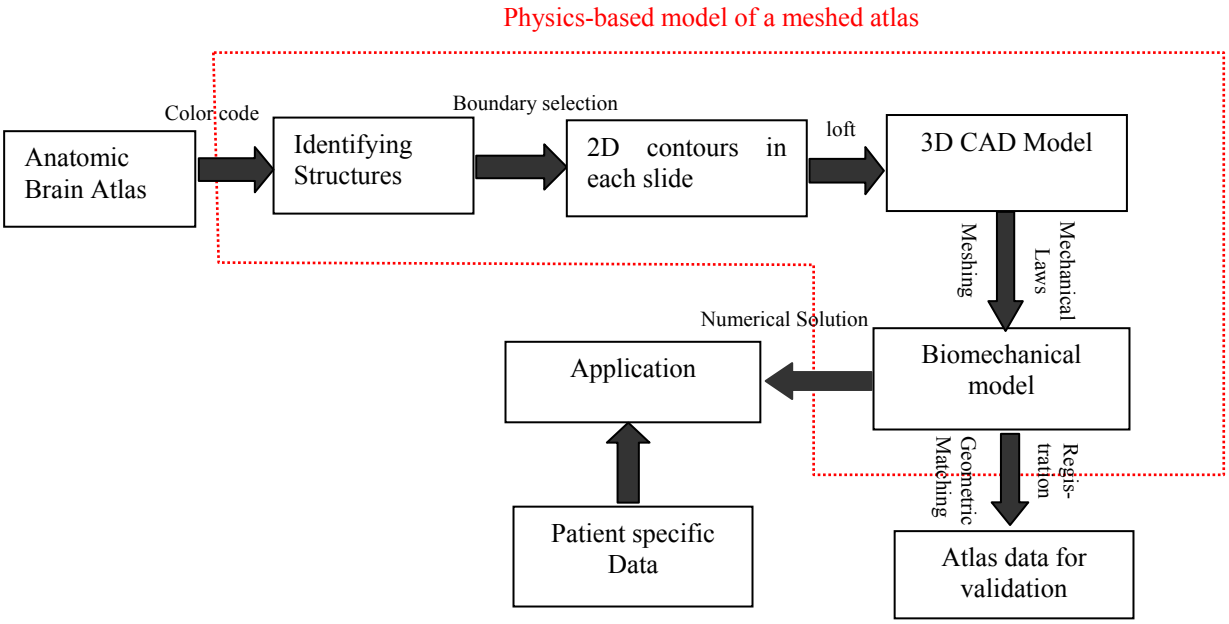

Figure 4.1 Framework of the proposed physics-based meshed atlas

The previous chapter describes the various modeling issues and related literature review of physics-based (biomechanical) modeling. Since FEM method is the heart of the developed physics-based atlas model, this chapter's focus will be more on Finite element method.

4.2 Principles of Finite Element Method (FEM)

Most recent PB models have applied Finite Element Method (FEM) – a numerical solution technique that has already shown great power and promise for the solution of differential equations in solid mechanics. Differential equations can model all physical phenomena in engineering and mechanics. Problem of engineering mechanics are most often too complicated to be solved using classical analytical methods (Ottosen and Peterson, 1992).

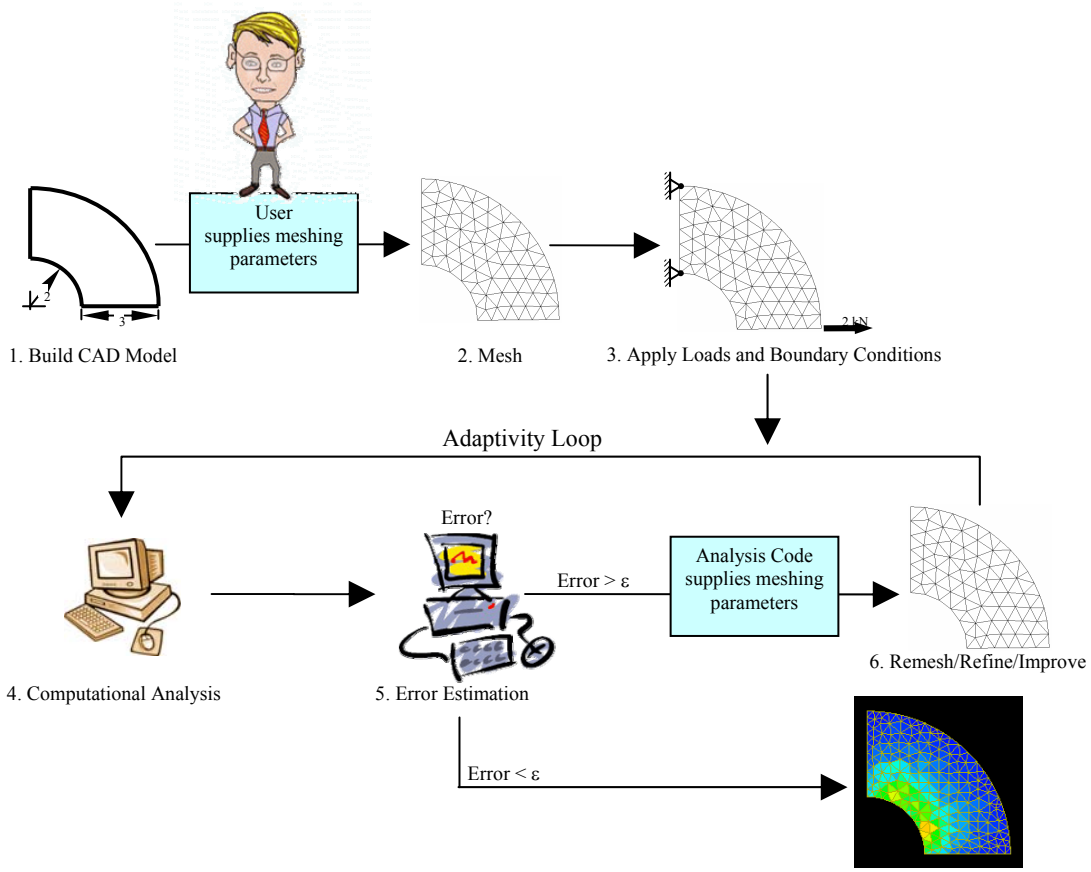

Figure 4.2 Typical finite element modeling technique used in CAD/CAM application

In such cases differential equations are solved in an approximate manner using numerical methods. Differential equations that describe physical phenomena are

assumed to hold over a certain 1D, 2D or 3D region. In finite element method, the entire physical phenomenon is divided into discrete number of such regions, so called finite elements, and solution approximation is subsequently carried out for each element. The collection of finite elements, which describes the physical phenomena, is called finite element mesh. Therefore, finite element meshing and modeling is the subdivision of physical phenomena into finite elements.

Figure 4.2 shows the typical numerical FEM technique for analyzing engineering design. The process starts with the creation of a geometric model. Then parameters are defined by the user. These parameters can be model dimension, material properties and/or any other entities that one needs to investigate. The model is then meshed into many small pieces called elements. Load, restraints are specified and the behavior of each mesh element can be determined after the approximation applied across the element. Computationally determining the approximation across the finite element mesh, the approximate solution of the entire physical phenomena can thus be obtained. For validation, the output is repeatedly checked with the theoretical (analytical) result. For any particular case, if analytical result does not exist, more simulation experiments are conducted in various design scenarios. The results are viewed and checked with an error limit (δ) specified by the user. If the computational error exceeds that limit remeshing/refining etc. is done (adaptivity loop in Figure 4.2) until the satisfactory result is obtained.

4.3 Finite Element Method for Medical Applications

Finite element method is the most common method to simulate complex technical processes. That's why in recent years, apart than its efficacy in solid mechanics and

other classical fields, FEM stretches its usefulness to various human musculoskeletal system, artificial implants, tumor growth, or calculating brain deformation in vivo and vitro. FE method can model very complex geometries with boundary conditions, and in addition inhomogeneous nonlinear materials can be simulated. In last couple of decades several FE based constitutive models have been reported analyzing soft tissue such as brain (Ferrant et al, 1999, 2001b; Hagemann et al, 1999; Warfield et al. 2002; Miller and Chinzei, 1997, 2002; Prange and Margulies, 2002), kidney (Schmidlin et al, 1996; Farshad et al., 1998), liver (Liu and Bilston, 2000; Schwartz et al, 2005) and breast (Azar FS et al , 2001, Samani A et al, 2001, Schnabel JA et al. 2003) and hard biological tissues such as bone and shells and spine (Jackson et al. 1988, Kumaresan et al 1999, Liu B et al 2006) etc. In the FEM an organ is discretized (meshed) into small volumetric elements, some examples are shown in Figure 4.3. The shape functions are then constructed upon this underlying discretized geometry. Generally, for computational simplicity, the shape functions are polynomials. Nonlinear shape functions increase the accuracy of the solution, whereas linear shape functions give a quicker solution as those take less processing time. The PDEs that represent constitutive laws are used with a variational formulation. This makes it possible to express the state variable (usually displacement) at every point within the model using only the nodal values of the mesh and the integrals of shape functions. The resulting system of equations will have as its unknowns the state variables (such as displacements) at the node locations. Once the equations are solved, the solution (in the sub-space of solutions considered) can be calculated everywhere by interpolation using the shape functions.

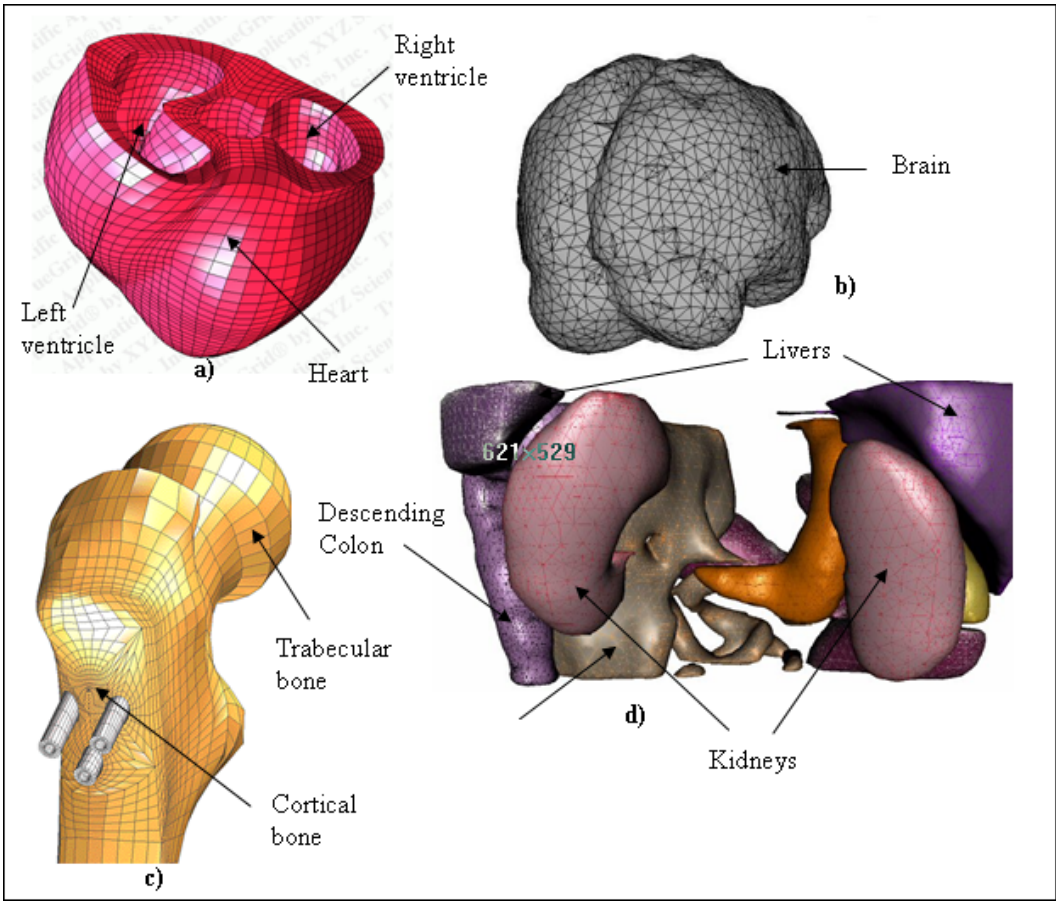

Figure 4.3 Finite element modeling of various tissues a) Heart : www.truegrid.com b) Brain: Carter et al, 2005, c) Femur: Cornell University d) Kidney area: Sullivan, 1997

The FEM has been implemented in a range of commercial software packages today, such as ABAQUS (ABAQUS Inc., Rhode Island, USA) and ANSYS (ANSYS Inc., Philadelphia, USA), CosmosWorks (SolidWorks Inc.), PROENGINEER etc. These allow models to be created relatively simply, although they do not always provide sufficient flexibility for medical applications: for example, introducing modifications to the available constitutive laws in order to test new models or defining

loads of a type suited to surgery guidance applications is often proved to be difficult. Research on FEMs is still an active area, for example in the definition of new shape functions and elements which can reproduce newer possibilities. One such recent development is the extended finite element method XFEM (Moes et al, 1999; Vigneron et al, 2004), in which additional shape functions are introduced. This removes the need for remeshing when modeling discontinuities. For solving the problems that require the ability to treat large deformations, Mesh Free methods are also gaining popularity.

4.4 FEM Principles and Algorithms

Finite element mesh generation, or finite element modeling are usually grouped into two categories, *structured* and *unstructured*. Structured meshing is commonly referred to as "grid generation" as all interior nodes of the mesh have equal number of adjacent elements.

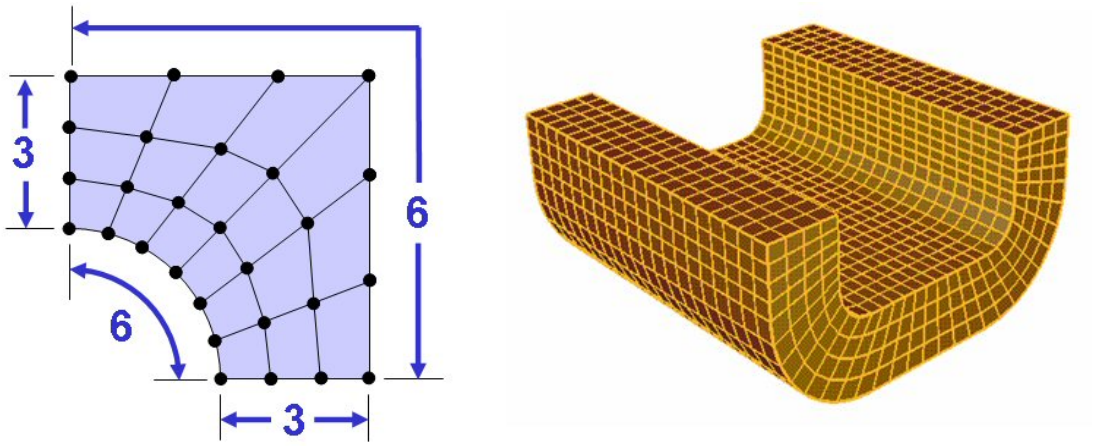

Figure 4.4 Illustration of structured mesh (Owen, S., 1998)

Figure 4.4 shows an illustration of structured mesh. The opposite sides must have similar intervals or similar mapped meshes to construct structured mesh. There are several algorithms (such as Trans-finite Interpolation, abbreviated as TFI) available that map a regular lattice of quads onto polygon to develop structured mesh (Thompson et al, 1999; Cook and Oakes, 1982). The algorithms employed generally involve complex iterative smoothing techniques that attempts to align elements with boundaries or physical domains, this is often achieved by distorting the elements. Where boundary accuracy is not required, "block-structured" techniques can be employed to break the domain up into topological blocks.

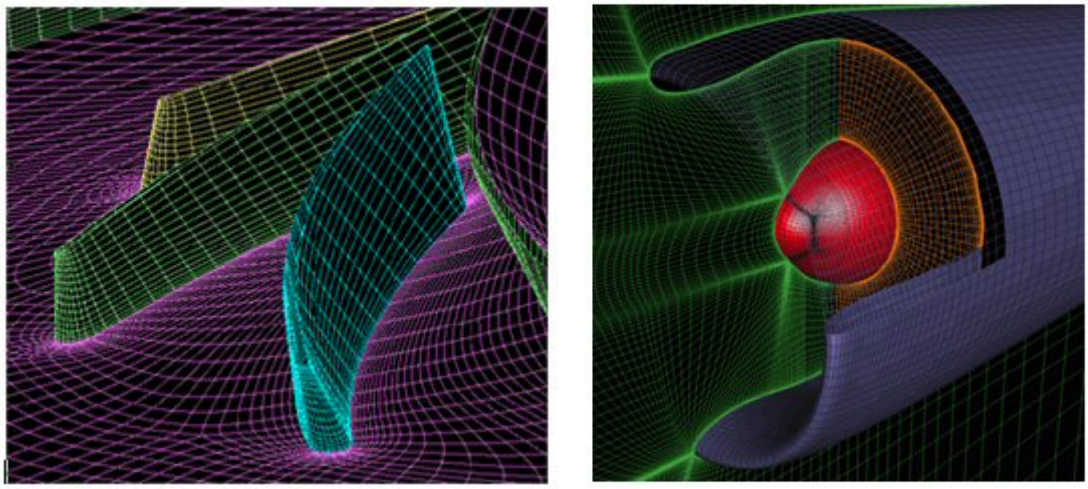

Figure 4.5 Illustration of Block-Structured mesh (Diagrams extracted from http://www.gridpro.com/gridgallery/tmachinery.html and http://www.pointwise.com/case/747.htm respectively)

On the other hand, unstructured mesh generation relaxes the node valence requirement, allowing any numbers of elements to meet at a single node. Triangle,

tetrahedral, quad or hexahedral elements are most common forms of unstructured elements used (Figure 4.6).

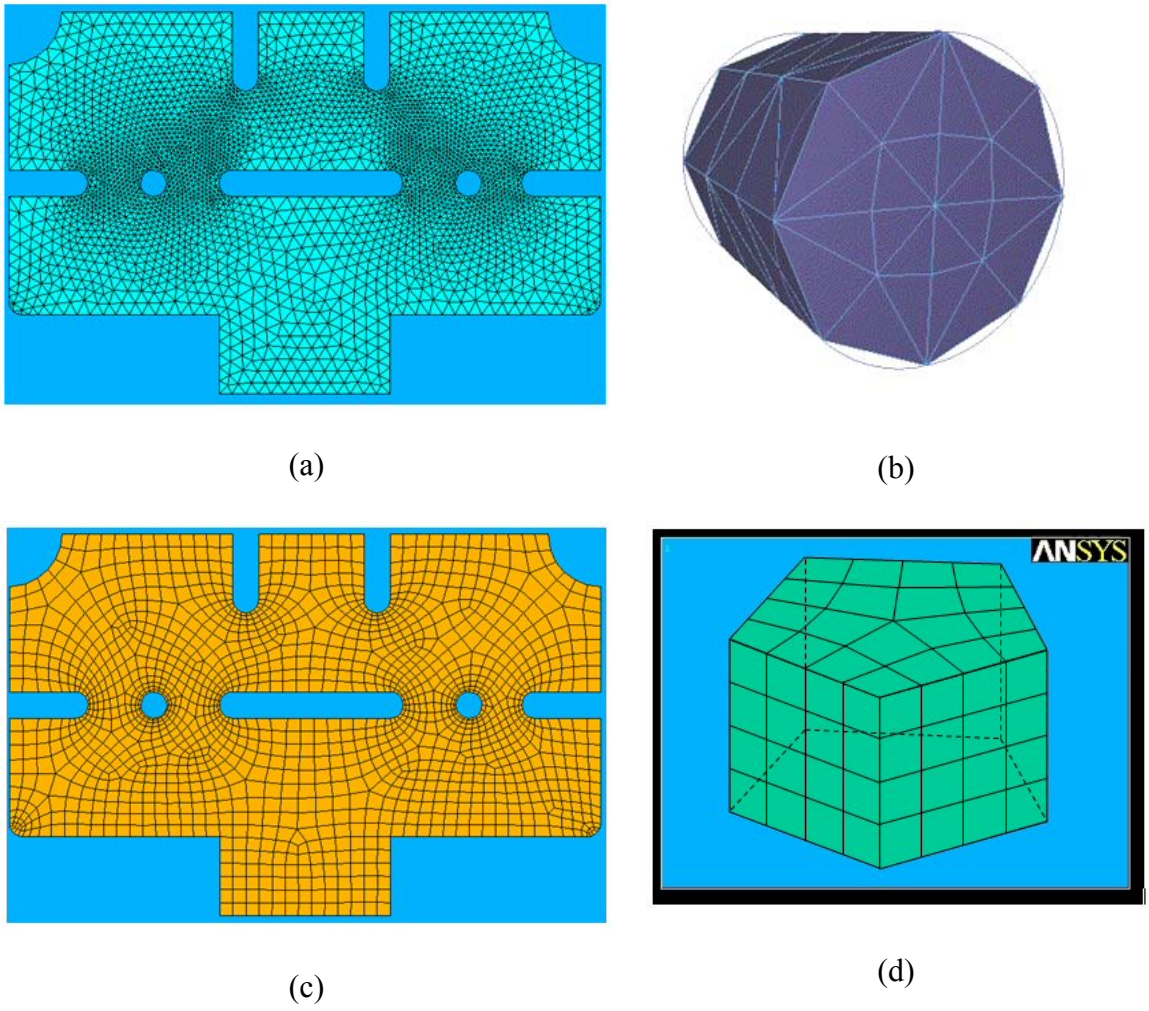

Figure 4.6 Illustration of unstructured mesh a) 2D triangular element b) 3D tetrahedral element c)2D quad d) 3D hexahedral element (Diagrams extracted from Owen S, Meshing Research Corner : http://www.andrew.cmu.edu/~sowen/mesh.html)

Algorithms employed for generation of mesh usually fall into one of the following categories:

1. Octree (Shepard and Marcel, 1991; Yerry et al, 1984),
2. Delaunay (Delaunay, 1934; Lawson, 1977),

3. Advancing Front (Lohner, 1996; Lo, 1991)
4. Grid-based approach (Schneiders, 1996),
5. Plastering (Blacker et al, 1993) and
6. Whisker-Weaving (Tautges, 1996).

The various algorithms can be represented as the following flowchart (Figure 4.7)

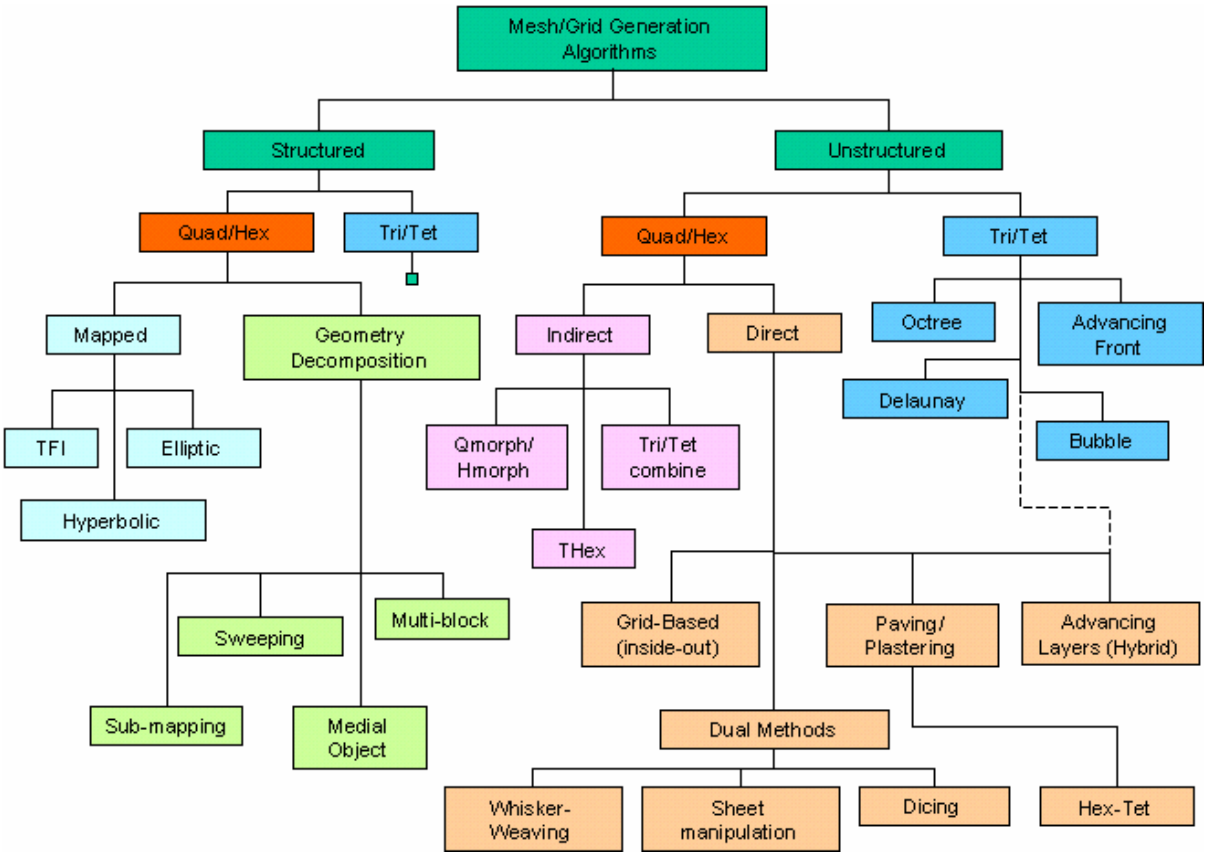

Figure 4.7 Various Meshing Algorithms (Owen S, Meshing Research Corner: http://www.andrew.cmu.edu/~sowen/mesh.html)

4.4.1 Meshing considerations

The meshing step is crucial to the ability of the FEM to represent deformation analysis. The size of the generated mesh (number of nodes and elements) depends on the geometry and dimensions of the model, element size, mesh tolerance, mesh

control, and contact specifications. The meshing element can be from a zero-dimensional mass particle to tetrahedral/hexahedral/pyramid element (Figure 4.8). The simplest volumetric element is a tetrahedron, with a node at each vertex. More complex element shapes include hexahedra and higher order elements, in which additional nodes are located at positions other than vertices. By using linear tetrahedral elements it can be possible to compute analytical integrals whilst other element shapes generally require numerical integration, using techniques such as Gaussian quadrature (Carter, 2005). Meshing anatomical structures with tetrahedra is relatively easy compared to hexahedra, as fewer elements are required to achieve a smooth surface of the organ. Sometimes cutting hexahedral meshes is not possible without introducing new elements, such as wedge-type or prismatic elements (Delingette and Ayache, 2004; Carter, 2005). Hexahedra and tetrahedron both provides structured or unstructured mesh, depending upon the requirement.

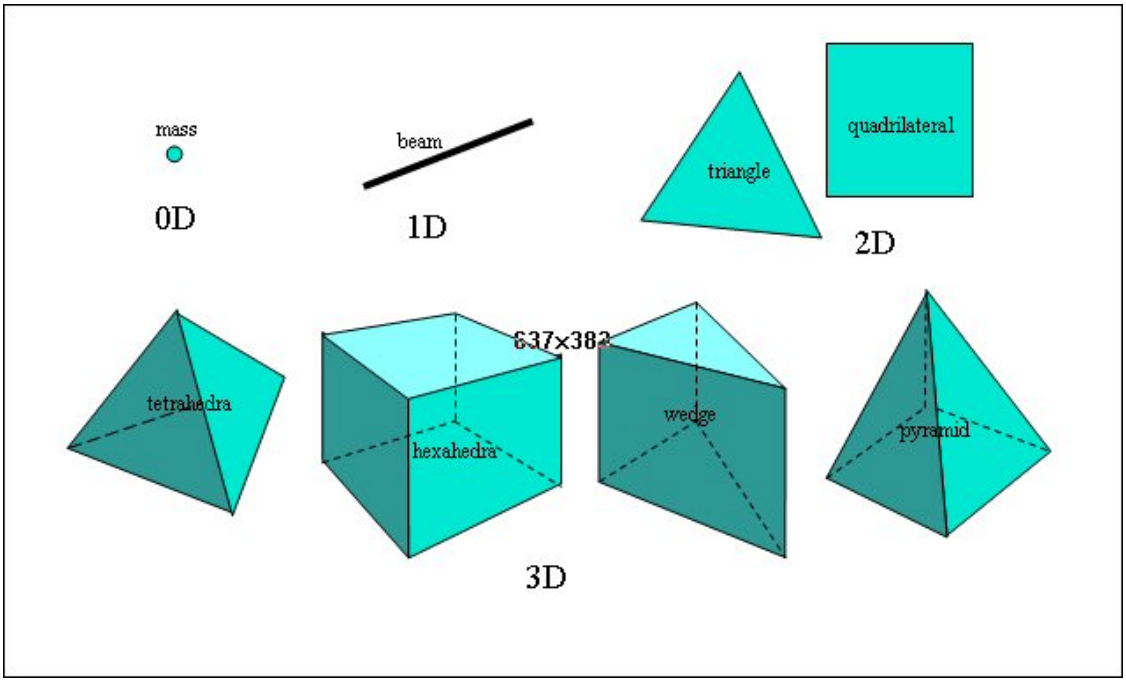

Figure 4.8 Various types of Meshing Elements

Soft tissue such as brain is considered nearly incompressible, due to its high water content. Unfortunately linear tetrahedral elements are particularly susceptible to 'locking'[22] when modeling almost incompressible material. Although this may lead to dubious result in stress calculation, the displacements (which are the variables of interest for computer-assisted surgery) do not give erroneous result (Bathe, 1996; Carter, 2005).

Locking effect can be reduced by introducing parabolic or higher order elements instead of linear. Linear elements are first-order; they are also called lower-order elements whereas parabolic (quadratic) elements are second-order, or higher-order elements. A linear tetrahedral element is defined by four corner nodes connected by six straight edges. On the other hand, a parabolic (quadratic) tetrahedral element is defined by four corner nodes, six mid-side nodes, and six edges. The Figure 4.9 shows schematic drawing of linear and parabolic (quadratic) tetrahedral solid elements.

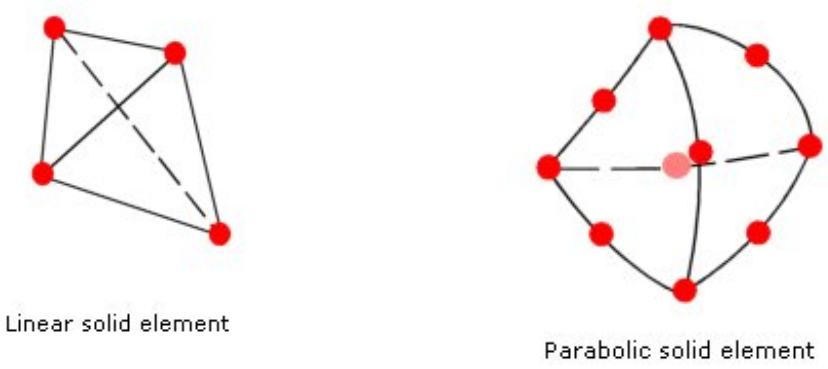

Figure 4.9 Locking effect can be reduced by introducing parabolic or higher order elements instead of linear

[22] Locking refers to an excessive stiffness of the mesh, resulting in erroneous result in FEM analysis.

For the same mesh density (number of elements) parabolic elements yield better results than linear elements because: 1) they represent flexible curved boundaries more accurately, and 2) they produce better mathematical approximations. Allowing flexible triangulation of arbitrary 3D domains, tetrahedral elements are widely used in the finite element analysis of solid structures. For this analysis parabolic (quadratic) tetrahedral elements are used for better accuracy and reduce locking effect. One of the general measures proposed to avoid the locking is the so-called reduced integration, which consists in taking a preferably low number of sample points for the numerical integration via Gauss-Legendre quadrature (Gladilin, 2003).

An important parameter for the accuracy and stability of the model solution is the so-called "element quality", which is the ratio of the different dimensions in an element. Although the accuracy of the final solution is generally increased by using smaller elements, this will also lengthen the computation time. It is possible to use elements of differing sizes, such that smaller elements are used to model regions near surfaces of high curvature or where high precision is desired, whilst using larger elements where precision is less important. Obtaining good quality meshes from medical images is still difficult especially for many image-guided applications (Carter et al, 2005). Segmenting and meshing medical images are typically time consuming and require human interaction. One approach to easing this burden is to adopt the concept of mesh-warping, in which non-rigid registration techniques are used to warp an atlas mesh to match a patient's anatomy (Castellano-Smith, 2002).

4.4.1.1 Mesh Quality Check

The quality of the mesh plays a key role in the accuracy of the results. The accuracy of the finite element calculation depends on the quality of meshed element. One of the reasons is that the derivatives of the basis functions needed for assembly of the elementary matrix are reciprocally proportional to the element volume (Gladilin, 2003). Degenerated tetrahedrons with small volume in conjunction with large displacements of the associated nodes may lead to large local errors. Two important checks to measure the quality of elements are:

1. Aspect ratio checking
2. Jacobian checking

Aspect Ratio Checking:

For a solid mesh, numerical accuracy is best achieved by a mesh with uniform perfect tetrahedral elements whose edges are equal in length with angles of $\pi/3$. For a general geometry, it is not possible to create a mesh of perfect tetrahedral elements. Due to small edges, curved geometry, thin features, and sharp corners, some of the generated elements can have some of their edges much longer than others. When the edges of an element become much different in length, the accuracy of the results deteriorates. Poorly shaped or distorted elements can result in numerical difficulties during the solution process. For example, it has been shown that as element angles become too large, the discretization error in the finite element solution is increased and as angles become too small the condition number of the element matrix is increased (Freitag and Ollivier-Gooch, 1996).

The aspect ratio of a perfect tetrahedral element is used as the basis for calculating aspect ratios of other elements. The aspect ratio of an element is defined as the ratio between the longest edge and the shortest normal dropped from a vertex to the opposite face normalized with respect to a perfect tetrahedral. By definition, the aspect ratio of a perfect tetrahedral element is 1.0.

Figure 4.10 a) Tetrahedral element with relatively high aspect ratio (should be avoided); b) Tetrahedral element with aspect ratio 1

The aspect ratio check assumes straight edges connecting the four corner nodes. The aspect ratio check is automatically used by the program to check the quality of the mesh. Most tetrahedral quality measures are based on geometric quality indicators (Parthasarathy et al., 1993; Berzins, 1999). One of the common ways to calculate aspect ratio is given by (Ferrant, 2001b):

$$A_\gamma = \frac{\left(\frac{1}{6}\sum_{i=1}^{6} l_i^2\right)^{3/2}}{8.47867 V^{el}} \tag{4.1}$$

where V^{el} is the volume of the tetrahedron, and l_i (i = 1…6) are its edge lengths. The aspect ratio metric is normalized so that A = 1 corresponds to an ideal element and $A \to \infty$ as the element becomes increasingly distorted.

Jacobian Checking

Quadratic elements can map curved geometry much more accurately than linear elements of the same size. The mid-side nodes of the boundary edges of an element are placed on the actual geometry of the model. In extremely sharp or curved boundaries, placing the mid-side nodes on the actual geometry can result in generating distorted elements with edges crossing over each other. The Jacobian of an extremely distorted element becomes negative. An element with a negative Jacobian causes the analysis program to stop. The Jacobian check is based on a number of points located within each element.

The Jacobian ratio of a parabolic or quadratic tetrahedral element, with all mid-side nodes located exactly at the middle of the straight edges, is 1.0. The Jacobian ratio increases as the curvatures of the edges increase. The Jacobian ratio at a point inside the element provides a measure of the degree of distortion of the element at that location. Normally Jacobian ratio at the selected number of Gaussian points is calculated for each tetrahedral element. Based on stochastic studies it is generally seen that a Jacobian Ratio of forty or less is normally acceptable.

The following sections will mainly focus on construction of FEM brain model from *Cerefy*. In the 1st chapter of this dissertation, main features and advantages of the Cerefy brain atlas were described (see section 1.4.2.1). The following section will elaborate the method of construction a physics-based FE model using the atlas database.

4.5 Biomechanical (FEM) Model of Brain from the Atlas Data

Because the *Cerefy* Brain Atlas is fully colored and labeled, the *feature points* (a set of point database describing the outlines or surface features of an object) of each structure were easily extracted. For example, the RGB value of the *corpus callosum* has been denoted by number: (130, 75, 130); *putamen*: (0, 135, 91); *hippocampus*: (179, 147, 179); *caudate nucleus:* (255, 239, 0) etc. The surface features of 43 structures were extracted from the images (bitmaps) of 27 axial plates of *Cerefy* separated about 2-5 mm vertically from each other. The outline, white matter and 43 identified structures with their individual color codes have been listed in Appendix I. The feature points of the individual structures have been extracted to form *point clouds* (a set of three-dimensional points in 3D CAD) shown in Figure 4.11.

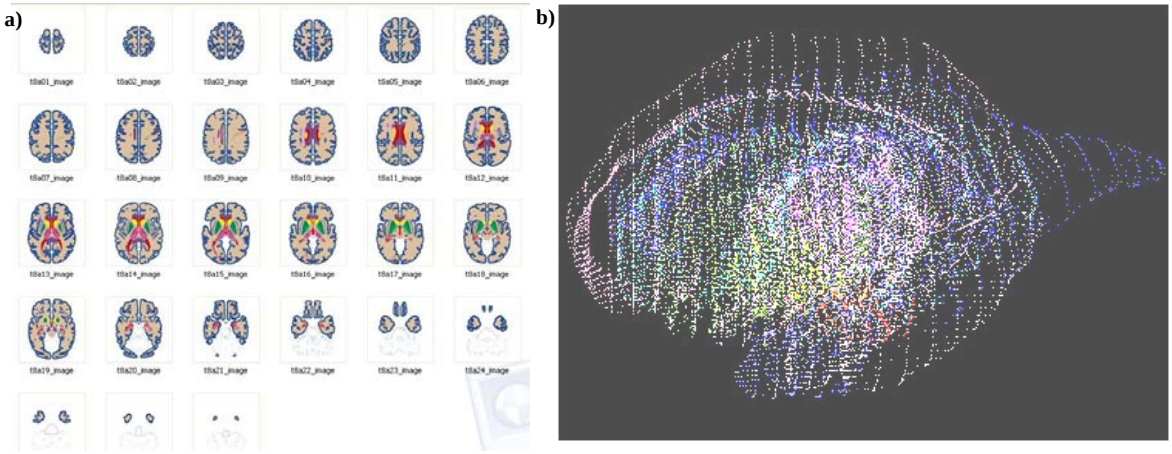

Figure 4.11 (a) 27 plates of the *Ceerefy* Brain Atlas, (b) formation of point clouds from the atlas data.

The surface models were constructed in a CAD platform from these point clouds. The model was then filled with solid tetrahedrons and prepared for Finite Element Analysis. The typical flowchart is as follows: *Bitmaps* → *2D feature points* → *Point*

clouds → *Surface mesh* → *Volumetric mesh.* The details of the steps (Figure 4.12) will be discussed in subsequent sections.

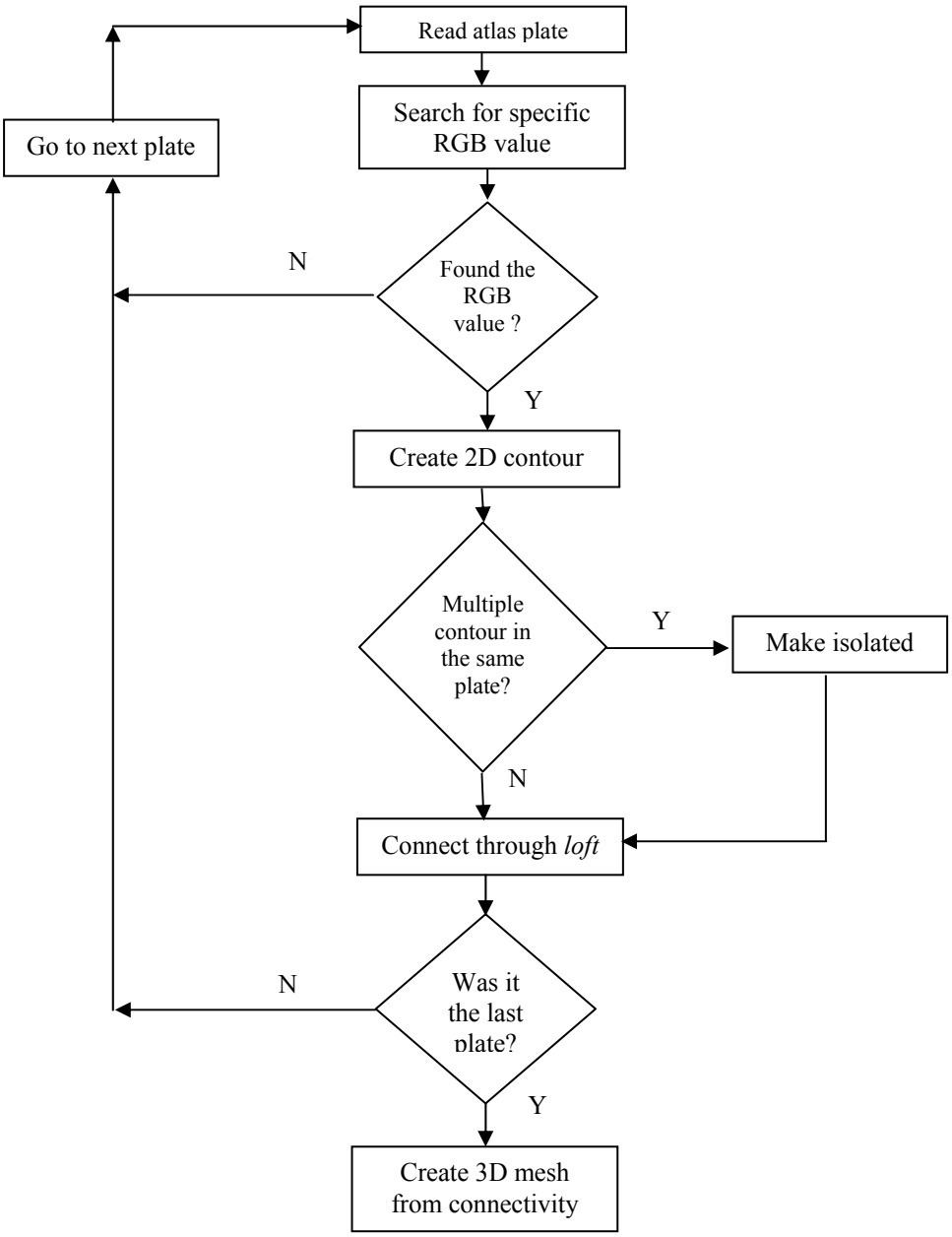

Figure 4.12 Flowchart of different stages for the construction of meshed structures

4.6 Construction of Biomechanical CAD Model

The following conditions are considered to be met while constructing the 3D CAD model:

1. Design model should be built in 3D solids (and surfaces) that fully enclose volumes.
2. The parts were supposed to be meshed with tetrahedrons or will be simple enough to provide foundation for solid mapped brick meshing or mid-plane surface extraction for building shell models.
3. The CAD model should be optimized.

The first two conditions were met and geometry was constructed with the proper experience (with CAD software) and practices. These modeling issues fall primarily in two categories: *clean geometry* and fragile *parent-child or dependency* relations (Adams and Askenazi, 1998). The clean geometry was ensured in such a way that the model maximized the possibility for mesh which in turn captured the features required the correct result. Special care was given in *short edges*[23], *silver surfaces*[24], and checked whether there were any *voids* or *cracks* in the solid model. The third point may need further clarification. When the design had processed to the point that a detailed CAD model existed, we evaluated the possibility of saving time by optimizing the model considering modeling speed, solution speed, accuracy and convergence.

[23] In CAD model, *short edges* are commonly known as corner edges

[24] *Silver surfaces* are the faces on a part with the high aspect ratio.

Consequently, the model was made possible for checking of *topological constrains* and *relationship constrains* that allow optimization routine to evaluate possible configurations.

The model was created using a *SolidWorks*™ tool called *loft. Loft* uses cross sections to extrapolate along a curve[25]. It lets user create complex 3D shapes by interpolating multiple 2D cross-sections of various size (CosmosWorks, 2004). Loft connectors define how models profiles align. The generic algorithm for constructing the structures is shown in Figure 4.12. Construction of 3D model of some deep structures such as the *putamen* (Fig. 4.13a) or the *hippocampus* (Fig. 4.13b) was straight forward and easy, while constructing some other parts such as the *corpus callosum* or the *caudate nucleus* (Fig. 4.13c) were never been straight for having concavity and convexities along axial plane. We had to construct those structures breaking into several steps, piece by piece. Main difficulty was to maintain the connectivity in the multiple divisions in two successive slides. The construction of *corpus callosum* for instance, has been explained through the following sections.

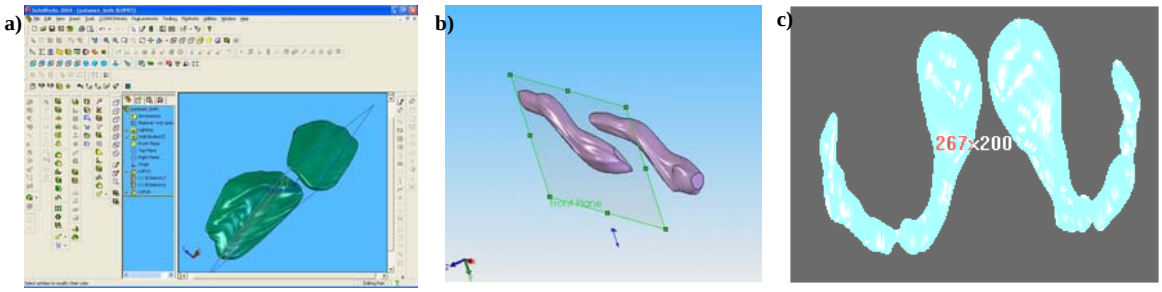

Figure 4.13 Construction of a) putamen b) hippocampus c) caudate nucleus using loft technique

[25] Also see Appendix IV for implementation of loft in a Java platform

Figure 4.14a is the 11th plate of the electronic atlas. This plate shows a continuous cross-sectional area of *corpus callosum*. The area is divided into two parts in successive plates, shown in Figure 4.14b. To maintain the connectivity, all the data (text file of 3D points) of each atlas plate has been uploaded in *SolidWorks*™. *SolidWorks* (ver. 2005) does not recognize text file for drawing 3D points; therefore, a macro[26] using *Visual Basic* script has been written to interact with this software (Appendix V). It allows reading 3D point cloud data from a text file and then automatically placing the points into CAD system. 3 separate parts (for the *corpus callosum*) have been constructed from the data using *loft* feature. Then multiple solid bodies are combined to create a single-bodied part. The process has been shown in the Figure 4.15.

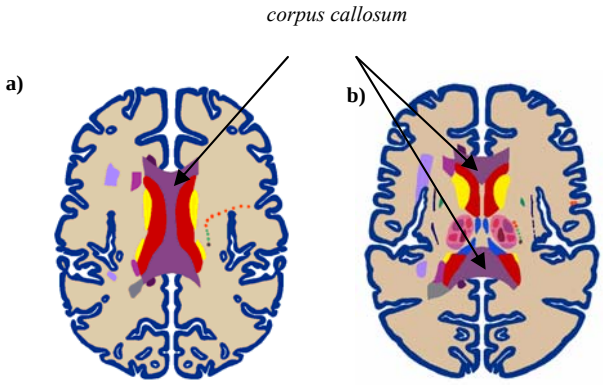

Figure 4.14 11th plate of the *Cerefy* brain atlas showing the *corpus callosum* with the continuous cross section, (b) 12th plate showing the division into 2 parts

Figure 4.15a shows three parts, one of the existing parts is a solid *loft*, created by the planar profiles while the other two remain in the sketch plane. Figure 4.15b shows

[26] SolidWorks macros are ASCII text files containing basic code. They are identical to a standard Visual Basic (VB) other than having different file extension such as *swp*.

the three lofted solids which were then combined (merged) into a single solid volume, Figure 4.15c. The next two figures show surface mesh [Figure 4.15d] and volumetric mesh [Figure 4.15e].

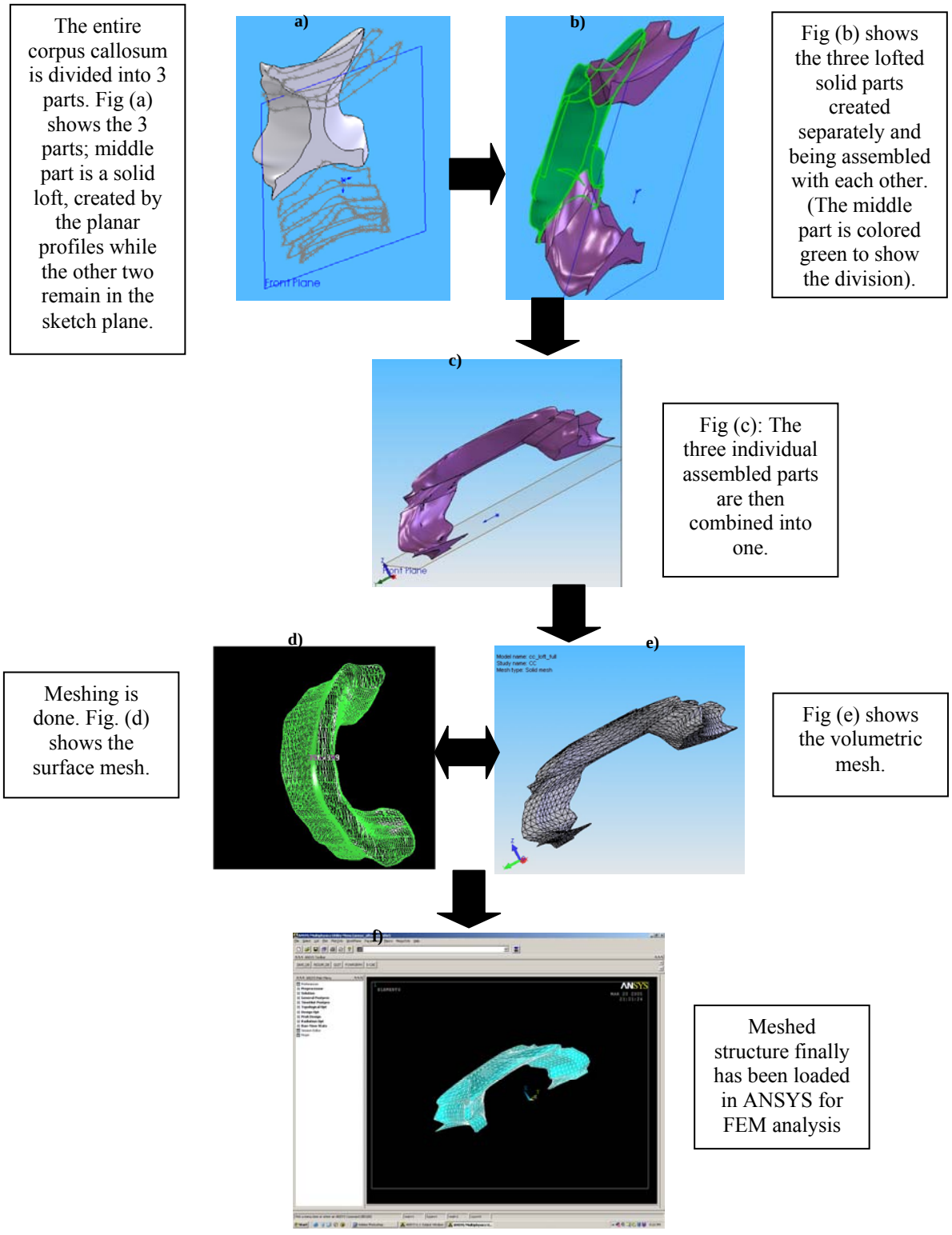

Figure 4.15 Various steps involved in construction of the corpus callosum

The mesh has been created in *COSMOSWorks™*. The volumetric meshed model then loaded in *ANSYS* for FE analysis [Fig 4.15f], as it supports all basic types of nonlinearities such as large deformations, plasticity, creep, stress stiffening, contact (gap) elements, hyperelastic elements, and so on (ANSYS, 2004).

4.7 Mesh Generation for Biomechanical Model

Prior to mesh generation a proper planning stage is needed. The planning involves *Grouping and Layering* by which various parts of the brain (assembly model) were organized in a separate group to assist the model building. The other two criteria are to check *Element selection* (type of elements to be used for meshing) and to decide on *Manual vs. Automatic meshing* etc. As the manual mesh is proved to be very time-consuming on even moderately complex solid parts (Adams and Askenazi, 1998), it can be prohibitive in design environment of meshed atlas. The automatic mesher in *COSMOSWorks™* (later uploaded in *ANSYS*) has been used to generate a mesh based on a global element size, tolerance and local mesh control specifications. Two key points were considered while meshing. First, geometric features must not prevent the mesh from being created and must also contain surfaces of consistent size and shape ratios to prevent forcing high *aspect ratio* and/or transitions between edges that may comprise accuracy. Generally a good rule of thumb for minimizing occurrence of high *aspect ratio* elements is to limit transitions into 2:1 or less, if geometry is broken into patches (Adams and Askenazi, 1998). Secondly, simplification or manipulation of features in an attempt to clean up geometry (discussed in the previous section) would not reduce structural integrity of the part. In the early stages of design a larger element size was specified for a faster solution. Later, for a more accurate solution, a smaller element size was chosen. A state of art approach for the geometric modeling is the generation of surface models through a process known as *triangulation*. Allowing

flexible triangulation of arbitrary 3D domains, tetrahedral elements are widely used in the finite element analysis of solid structures (Gladilin, 2003). In this work, mesh was generated by 10 node 3D parabolic (quadratic) tetrahedral solid elements (SOLID187). According to the authors' view type of mesh (tetrahedral/hexahedral) should not be taken as a major issue, as long as simulation of biological soft tissue is under concern (for detailed discussion check the section on *meshing consideration* 4.4.1 and 4.10).

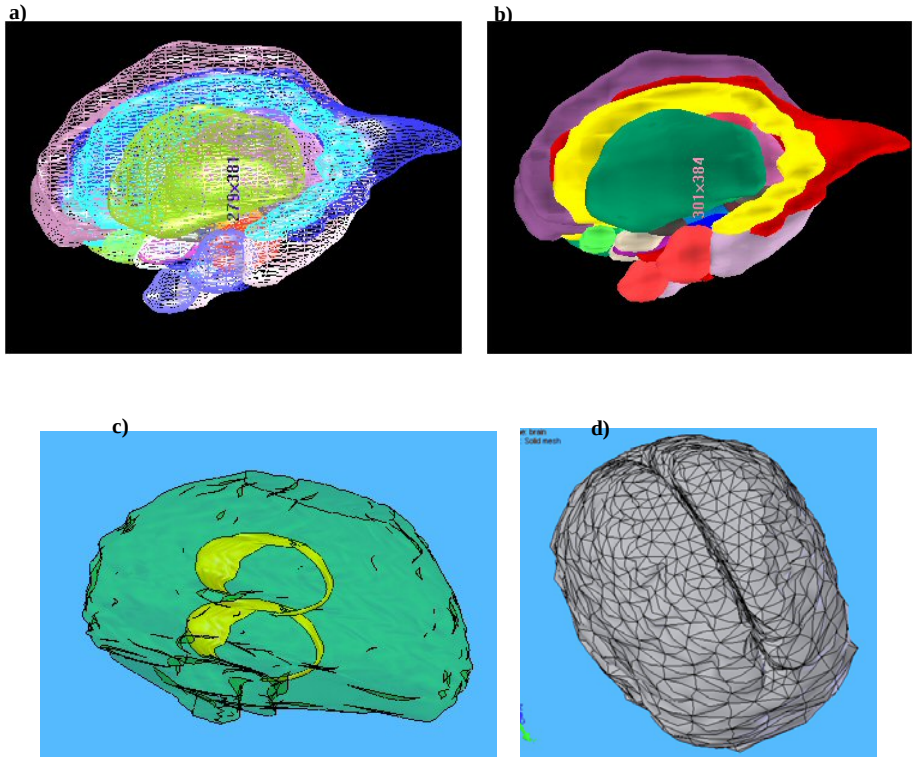

Figure 4.16 3D model of brain : (a) surface mesh, (b) volumetric mesh, (c) brain with the caudate nucleus, (d) meshed model showing tetrahedrons

Before initiating the simulation analysis, two types of "final model checks" were performed: 1) Free node check (deleting all unattached nodes), 2) Model continuity check. Then the model is made ready for further verification and FE analysis. The entire brain model (surface area: 90917.09 mm^2) consists of 327500 elements with 587600 numbers of nodes (avg. element size: 4.1691mm, tolerance: 0.03085). A

relatively simplified homogeneous and isotropic model has also been meshed where node and element numbers are 24840 and 16264 respectively. Figure 4.16 shows the surface and volumetric mesh of the constructed model. The basic comparison of PBA with WSUBIM has been shown in the following table (Table 4-1).

Table 4-1 Comparison of PBA with Wayne State University model (2001)

Properties	**WSUBIM**	**PBA (our model)**
Structures	7	43
Element size	10~15 mm	4.17 mm
Number of Nodes	29,000	5,87,600
Number of Elements	38,000	3,27,500
Jacobian Ratio	unknown	1.5~1.7
Aspect Ratio	unknown	1.9~2.5
Material properties	Visco-elastic	Hyper visco-elastic
Main organ	Head and neck	Only brain
Primary source	CT scan	atlas data
Strain rate	high	Moderate and low
Application range	Brain injury	Surgery, structural disease etc.

The above table shows that PBA has incorporated 43 structures in its model compared to only 7 structures of WSUBIM. The average element size of PBA is significantly smaller and it also integrated more elements and more nodes in the FEM model compared to WSUBIM. Wayne State University model only applies to the brain injury due to high impact whereas PBA can be used to simulate neurosurgical scenario and some diseases such as tumor growth and hydrocephalus.

4.8 Validation of the Proposed Model

Accurate solution in FEA depends on the correctness of geometry, material properties and the assumed boundary conditions. For a given set of properties, geometrical accuracy is controlled by the mesh. The uncertainties driven by material

properties and boundary conditions are usually considered as subjective and open to interpretation while the uncertainty contribution due to geometry and due to mesh is totally under designer and analyst's control. As a rational choice for a realistic validation, we limit our check in geometrical (geometry of anatomical structures) validation and convergence of the mesh in our proposed model.

4.8.1 Geometrical Validation

To check the validity of our proposed model, we studied the accuracy of our 3D reconstruction by cross sectioning the surface models comparing with the 2D atlas plates. The general flow chart is shown in Figure 4.17.

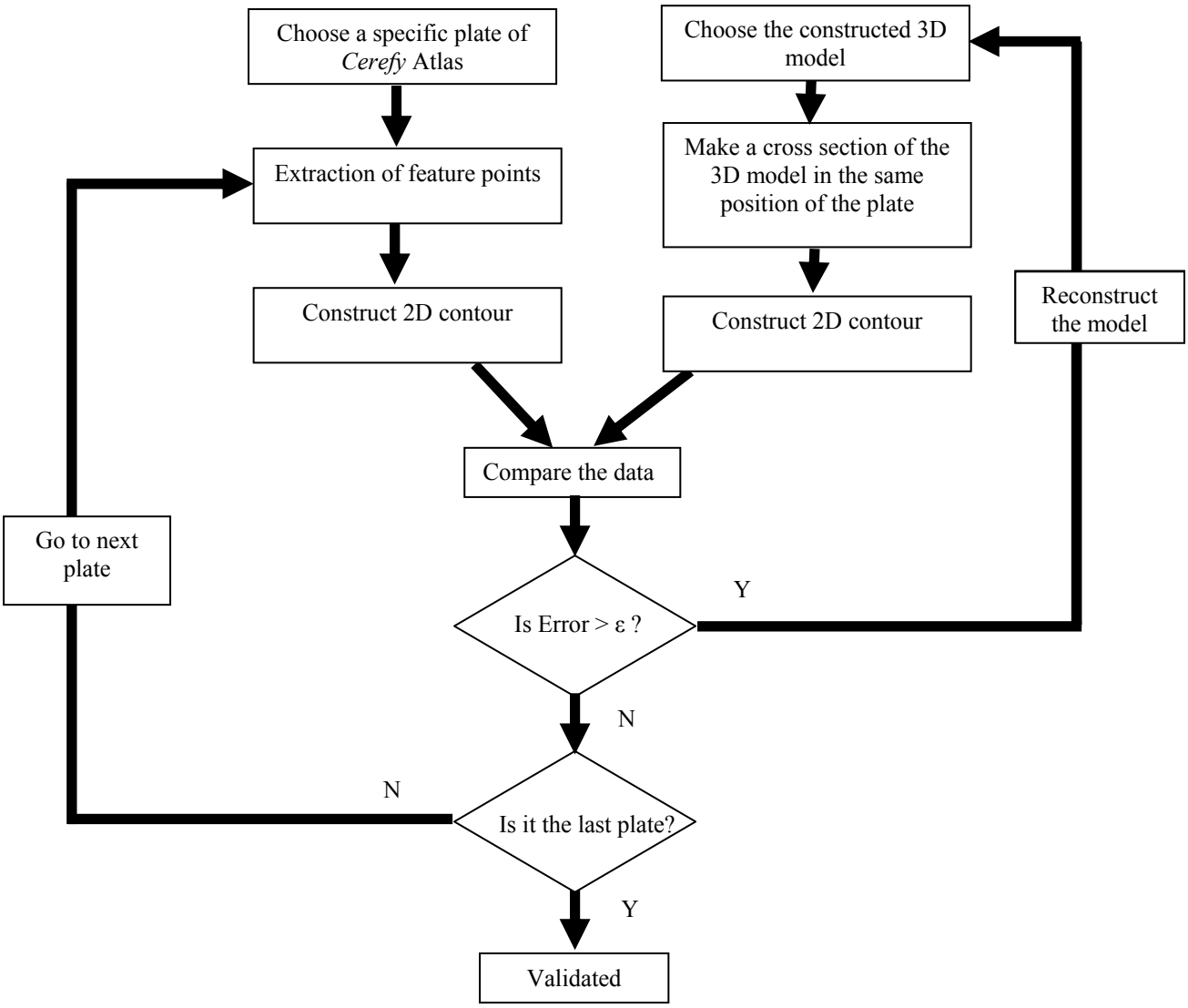

Figure 4.17 Flowchart of the verification of the proposed model

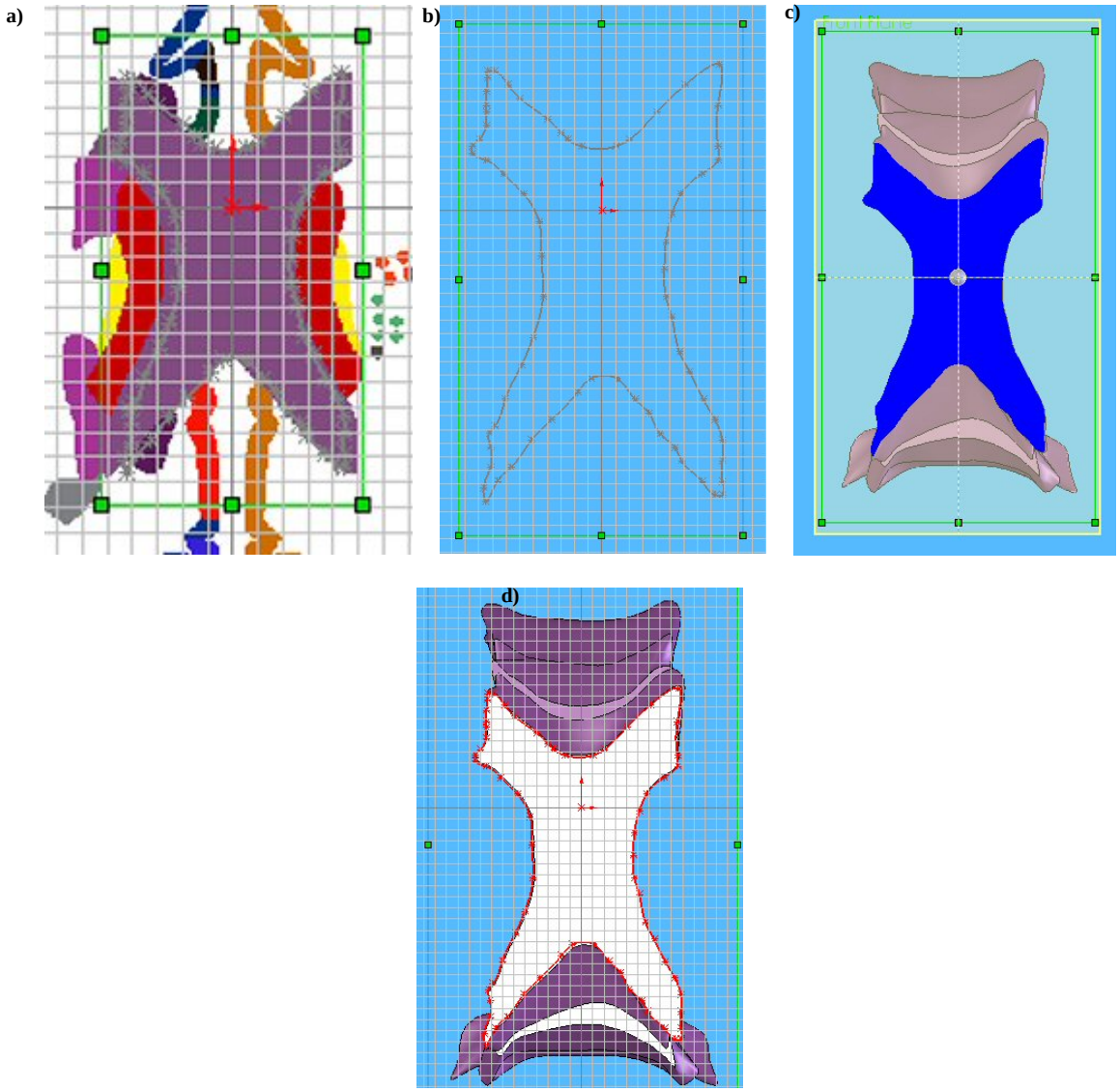

Figure 4.18 Verification of the *corpus callosum*: (a) Feature points extractin from the *Cerefy* atlas. (b) 2D contour formed from extracted points. (c) Cross section view of the 3D model on the same position of the atlas plate. (d) Interpolation of atlas data on the cross section

Here the *corpus callosum* is taken as an example to demonstrate the validation process. Fig. 4.18a shows the feature points of the *corpus callosum* extracted from one of the plates (plate number: 10, 24 mm from the base line) of the brain atlas. Fig. 4.18b presents the 2D contour formed from the extracted points. Fig. 4.18c shows the cross sectional view of the 3D model. This sectional view was obtained from the same

position of the atlas plate. The cross sectional data of the *corpus callosum* were compared with the atlas data, Fig. 9d. The error limit ε was set as 0.65mm [27] for both average or mean sectional error (for each cross section), and for percentage error (for each structure) of final geometry. The model was reconstructed if the measured error exceeded the specified limit. To compare the data, 5 common feature points or landmarks (A, B, C, D, E and F) were selected that would identify the 2 cross sections of the atlas and model simultaneously. This has been illustrated in Figure 4.19.

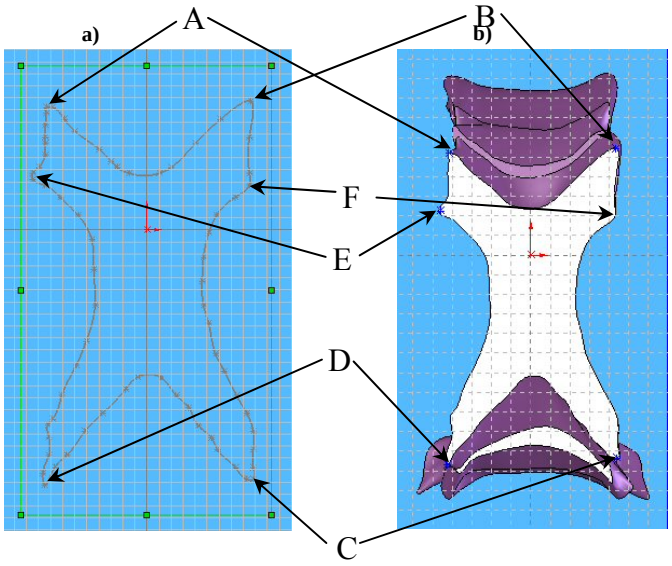

Figure 4.19 Common feature points (a) in 2D contour of the atlas data. (b) in 2D cross section of the proposed model

These results are put in Table 4-1.

[27] The rationale behind this choice of this particular value has been discussed in section 4.10.

Table 4-2 The validation of proposed model: comparison of the Atlas data with cross sectional data for the *corpus callosum*.

Distance	Measurement based on atlas points (mm)	Measurements based on sectioned model (mm)	Relative Error (mm)	Sectional Error (mm)	Structural Error(mm)	% Error
A-B	d: 34.01 ΔX: 34.00 ΔY: 1.00	d: 34.29 ΔX: 34.27 ΔY: 1.10 (Fig. 4.201)	d: 0.28 ΔX: 0.27 ΔY: 0.1			
B-C	d: 63.00 ΔX: 0.44 ΔY: 63.00	d: 63.32 ΔX: 0.26 ΔY: 63.32	d: 0.32 ΔX: 0.18 ΔY: 0.32			
C-D	d: 34.75 ΔX: 34.73 ΔY: 1.00	d: 34.94 ΔX: 34.92 ΔY: 1.29	d: 0.19 ΔX: 0.19 ΔY: 0.29	0.44 mm*	0.32mm**	0.52 ^
D-E	d: 51.04 ΔX: 1.92 ΔY: 51.00	d: 51.79m ΔX: 1.61 ΔY: 51.77	d: 0.75 ΔX: 0.31 ΔY: 0.77			
B-F	d: 14.00 ΔX: 0.22 ΔY: 14.00	d: 14.68 ΔX: 0.48 ΔY: 14.67	d: 0.68 ΔX: 0.26 ΔY: 0.67			
Perimeter	232.80	233.55	Difference: 0.75			

* *Arithmetic mean is used follo*wing *the equation:* $\bar{e} = \frac{\sum_{i=1}^{n} e_i}{n}$, *where n is the number of landmarks.*

** *Weighted mean average is used (for the entire structure) following the equation:* $\bar{E} = \frac{\sum_{i=1}^{N} P_i \bar{e}_i}{\sum_{i=1}^{N} P_i}$

^ *% of error in geometry is calculated by:* $Err\% = \frac{\bar{E} \times N}{\sum_{i=1}^{N} P_i} \times 100$, *where N is the no. of cross sections.*

Figure 4.20 gives a pictorial description of the symbols used in Table 4-1 while considering two feature points A and B. The black line denotes the variation in x direction, the green line denotes the variation in y direction and the red line (AB) denotes the point to point distance.

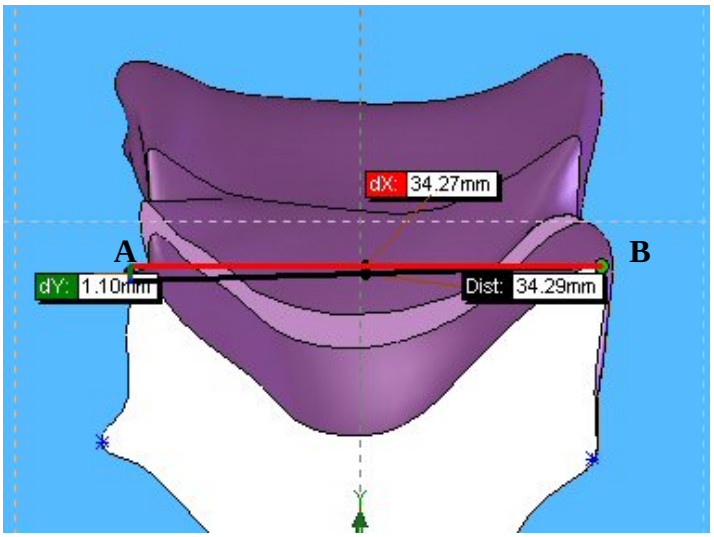

Figure 4.20 Graphic description of the symbol used in Table 4-1. ΔX (dx) = variation in x direction, ΔY (dy) = variation in y direction, d (Dist) = distance between two specified points, A and B

Structural error (error in geometry for the each structure) was defined as a criterion to quantify the error in each constructed structure. To determine the error, each structure was initially divided into several cross sections and then perimeter and sectional error has been determined. This *sectional error* is the simple arithmetic mean of the errors of specified landmarks in each cross section. The statistical weighted average method was then applied taking perimeters and sectional errors of other cross sections into account. This can be stated by the following equation:

$$\overline{E} = \frac{\sum_{i=1}^{N} P_i \overline{e}_i}{\sum_{i=1}^{N} P_i} \qquad (4.2)$$

where P_i is the perimeter , N is the number of cross sections being used and $\overline{e}_i$ is the average error of each cross section.

Lastly the percentage error in geometry was calculated from:

$$Err\% = \frac{\overline{E} \times N}{\sum_{i=1}^{N} P_i} \times 100 \qquad (4.3)$$

Let us give an illustration how this method can be applied on a specific structure, for example, the *Putamen*. For this structure 8 cross sections were used. For each cross section the perimeter and the average sectional error were determined (Figure 4.21).

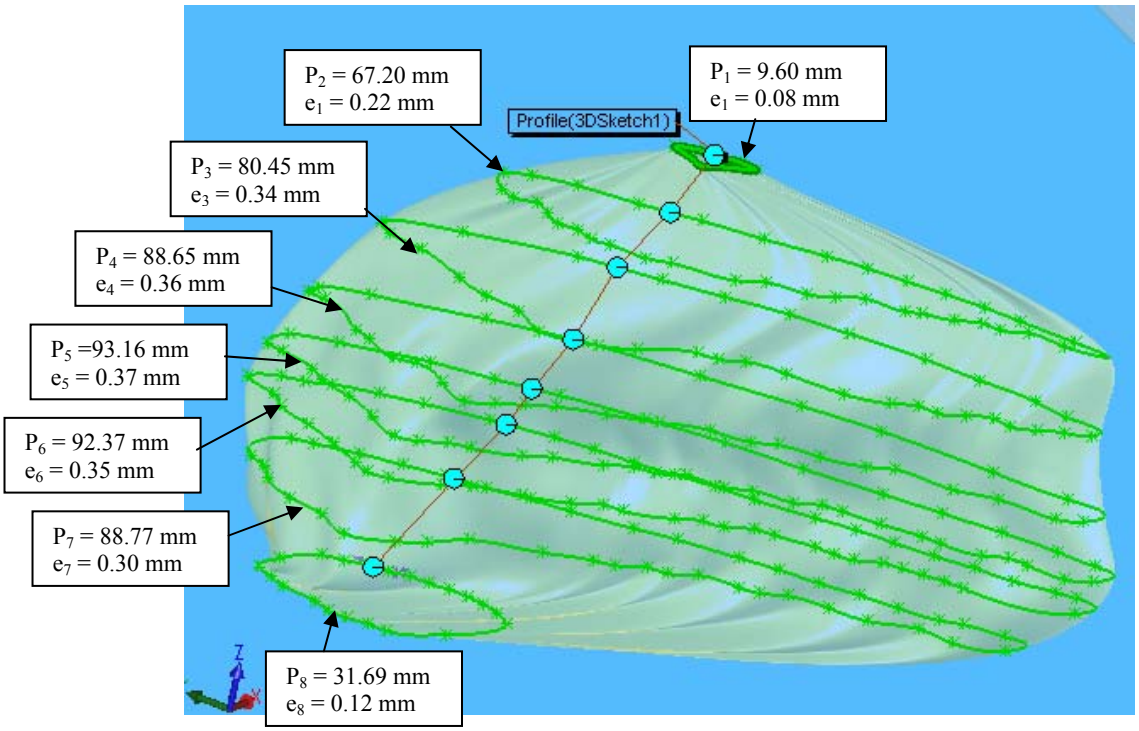

Figure 4.21 Perimeter and average error for each cross section of the constructed *putamen*

Then equation (4.2) gives the structural error for *putamen*:

$$= \frac{\{(9.60 \times 0.08) + (67.20 \times 0.22) + (80.45 \times 0.34) + (88.65 \times 0.36) + (93.16 \times 0.37) + (92.37 \times 0.35) + (88.77 \times 0.30) + (31.69 \times 0.12)\}}{(9.60 + 67.20 + 80.45 + 88.65 + 93.16 + 92.37 + 88.77 + 31.69)}$$

$$= 0.312mm$$

$$= 0.45\% \text{ of the original geometrical data [from equation (4.3)]}$$

Same validation procedure was applied for all the 43 structures and then for the whole brain. The result is enlisted in the following table (Table 4-2) with the mesh specifications.

Table 4-3 The validation of proposed model: Percentage error in comparison with original geometry.

Structure Name	Mesh		% Error
	No of Element	No of nodes	
Corpus callosum	9492	15927	0.52
Corpus geniculatum laterale	8088	14203	0.23
Corpus geniculatum mediale	8219	14540	0.37
Corpus mamillaris	8486	15289	0.24
Cortical areas	2672	5867	0.55
Cuneus	8449	15177	0.30
Fornix	8554	15494	0.28
Globus pallidus lateralis	4510	8072	0.49
Globus pallidus medialis	6248	10167	0.32
Hippocampal gyrus	8491	15303	0.21
Hippocampus	4998	8211	0.38
Hypothalamus: POL	8228	14562	0.25
Hypothalamus: SO	8215	14528	0.28
Hypothalamus: VM	8518	15383	0.22
Hypothalamus: LAT	8320	14813	0.34
Inferior frontal gyrus	8352	14901	0.32
Inferior occipital gyrus	8486	15288	0.28
Inferior temporal	8494	15311	0.30
Insula	8451	15183	0.20
Lingual gyrus	8321	14815	0.26
Medial frontal gyrus	8385	14994	0.34
Middle frontal gyrus	8476	15259	0.32
Middle occipital gyrus	8496	15317	0.34
Middle temporal guyrus	8350	14896	0.44
Nucleus accumbens septi	8320	14812	0.45
Nucleus caudate	4079	7443	0.52
Nucleus ruber (bottom)	7916	13785	0.38
Nucleus ruber (top)	8262	14653	0.42
Nucleus subthalami	7911	13774	0.38
Putamen	1586	4705	0.45
Substantia nigra	8468	13696	0.25
Thalamus: Others	4169	7635	0.46
Thalamus: Anterior	7645	13175	0.38
Thalamus: Centromedianum	8012	14015	0.28
Thalamus: Dorso medial	6467	10944	0.33
Thalamus: Lateral dorsal	8291	14733	0.24
Thalamus: Lateral posterior	7587	13049	0.33
Thalamus: Pulvinar	3865	7257	0.42
Thalamus: Ventral anterior	7780	13472	0.38
Thalamus: Ventral lateral	5848	9953	0.45

Structure Name	Mesh		% Error
	No of Element	No of nodes	
Thalamus: Ventral posterior lateral	7272	12405	0.43
Thalamus: Ventral posteromedial	7957	13883	0.26
Ventriculus	9215	18256	0.59
Overall	**317949**	**565145**	**0.36**

It has been found that structures with bigger twist and turns (such as ventricles, caudate nucleus, corpus callosum etc.) are more prone to geometrical error compared to simple structures like substantia nigra, centromedianum thalamus or putamen. However, since the range of the percentage error in geometry of structures varies between 0.2-0.59% (average percentage error is 0.36%) which is very minimal compared to the surface area of the brain, the model falls in an acceptable range (user specified max. error limit was set as 0.65%). Finally, no structure has exceeded the user specified error limit after several times of reconstruction.

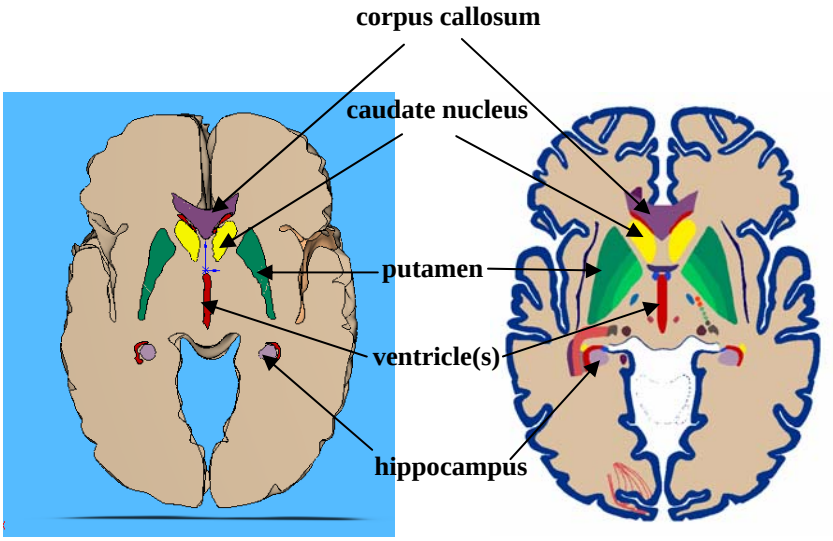

Figure 4.22 Comparison: a) cross section of 3D model, b) original atlas plate

Figure 4.22 provides a visual comparison between the newly developed 3D meshed atlas with one of the original 2D plates of *Cerefy*. Note that only the prominent

structures are shown in the 3D model for clarity and for obtaining faster solution. In a Hewlett Packard's B2000 Client workstations (with 1.60 GHz Intel Pentium processor, 352 MB RAM, windows XP as OS) it takes almost an hour to generate the whole brain having finer mesh with all the detailed structures. Figure 4.23 illustrates front, bottom and isometric view of 3D meshed model and compared (visually) with axial, coronal and sagittal plate of *Cerefy* atlas respectively.

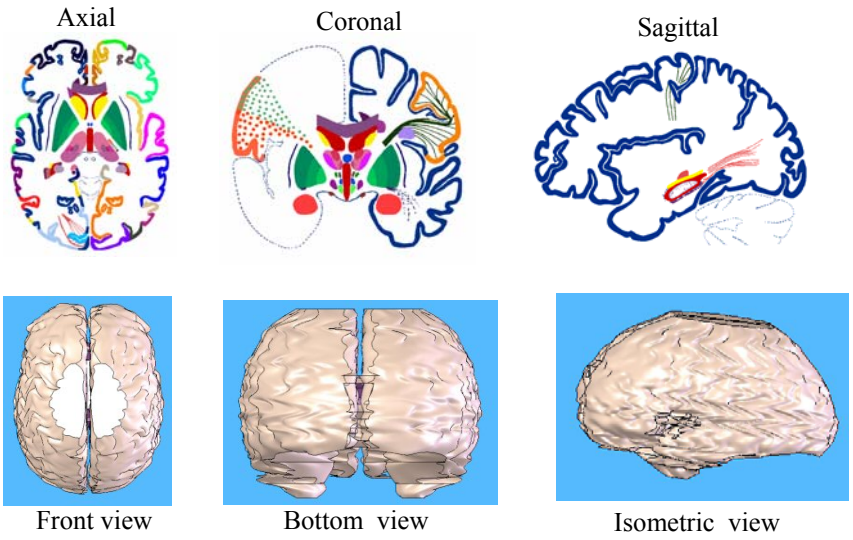

Figure 4.23 Visual comparison: Comparing 3D model with Atlas data; axial, coronal and sagittal cross sections of original electronic atlas are kept on the top; front, bottom and isometric view of 3D meshed model are kept at the bottom.

4.8.2 Mesh Optimization and Convergence study

Using commercial software package it is possible to generate hundred and thousands of meshing elements. However, dense mesh does not always lead to better solution. There are some penalties that should be kept in mind when one decides to use mesh-elements to a greater extent for a particular solution of a FE model. The penalties include:

1. Longer processing time to obtain the finite element solution.

2. Larger computational resources needed to process the finite element analysis as well as to store the final solution.
3. Slow graphics (in terms of zooming, rotating etc.) and definite time lag for CAS will be experienced.

Finite element analysis for the whole brain was re-run with each increment in mesh density and/or element complexity. This is performed until there is less than a 5% change in the final result, and then optimized FE model is obtained. Change in results of 5% in such cases is rarely warranted (Adams and Askenazi, 1998). This gave the confidence that FEM approximation had converged and the results were satisfactory. The conclusion matches with other groups (Miller, 2002a) in accord to determine the benchmark of mesh convergence study.

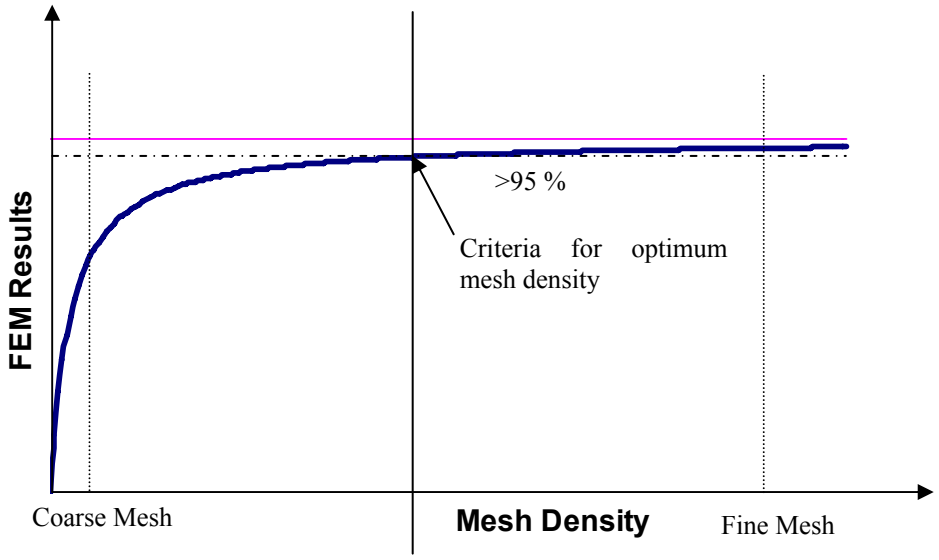

Figure 4.24 Graphical representations of the criteria for optimum mesh density

Ten different finite element models with different mesh densities were tested. Table 4-2 shows 3D mesh density used and corresponding number of nodes and elements.

Table 4-4 Different 3D mesh with corresponding number of elements and nodes

No of Nodes	Total Element	Von Mises Stress (Pa)
4670	2894	1.18E+04
5147	3193	1.22E+04
8812	5608	1.45E+04
11203	7205	1.59E+04
16777	10924	1.86E+04
18520	12069	1.92E+04
22000	14379	2.03E+04
24840	16264	2.10E+04
28306	18564	2.14E+04
29524	19373	2.15E+04

Static finite element analysis was conducted for each of the 10 cases listed above. All finite element analysis were conducted using commercial finite element software CosmosWorks and ANSYS on Hewlett Packard's B2000 Client workstations with 1.60 GHz Intel Pentium processor and 352 MB memory using windows XP operating system.

A uniform distributed load of 50 m-N was applied[28] to the top of the surface of the brain with the bottom surface rigidly fixed to determine optimum mesh of the model. The maximum Von Mises stress (Figure 4.25) in the longitudinal direction were noted and plotted against the number of nodes, for each of the ten FE models of the brain.

[28] The value was chosen as it was the approximate load applied to both experimental and computational biomechanics dealing with soft tissues. For example, indentation experiment (uniaxial compression test) on porcine brain in bioengineering lab of NUS (see next chapter) generated maximum load of 56 m-N (around) for 4 mm indentation of the brain at 1mm/sec indentator speed.

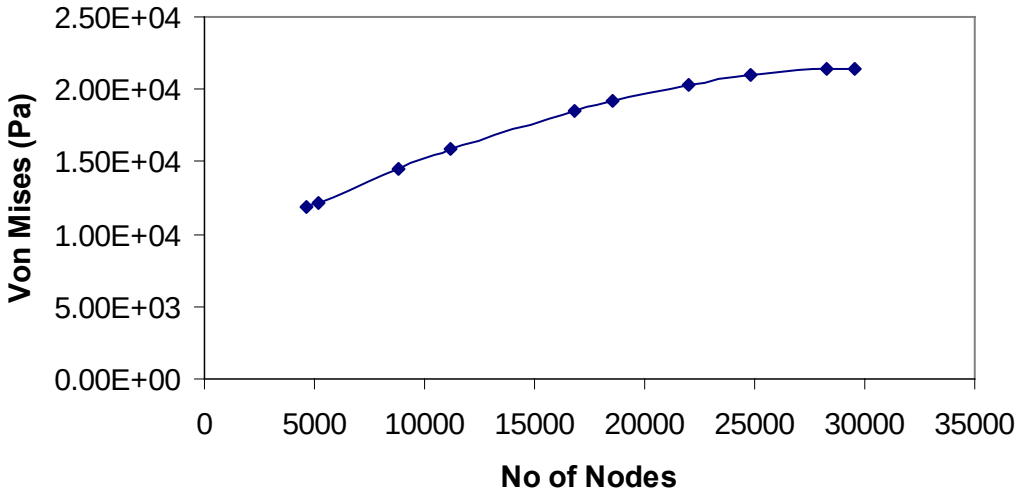

Figure 4.25 Graph of Von Mises stress vs. Number of nodes obtained from the static analysis for the ten different mesh densities

From this mesh optimization exercise, the optimum mesh was found to have within 24000 to 25000[29]. Between these two mesh densities the result obtained did not differ abruptly. The percentage difference between the two meshes for the analysis was found to be at 5%.

Using the similar principle, a two-dimensional finite element model of the brain/ventricle system was validated with the atlas data and then analyzed for mesh convergence study. This was done using *COSMOSWorks*™ software. The particular model in Fig. 4.26 is consisted of 471 numbers of tetrahedral elements of 4.51231 mm size, and 290 nodes. Fig. 4.26a shows geometric matching of a cross section with axial atlas data and Fig. 4.26b demonstrates the undeformed mesh used in the model. Results are obtained with the *highly dense* (total nodes 1127, total elements 503 and element size 4.2974mm) and *relatively coarse* (total nodes 311, total elements 503,

[29] Simplified model has been used to obtain relatively faster result.

element size: 4.297 mm) mesh, which had around three times fewer nodes.

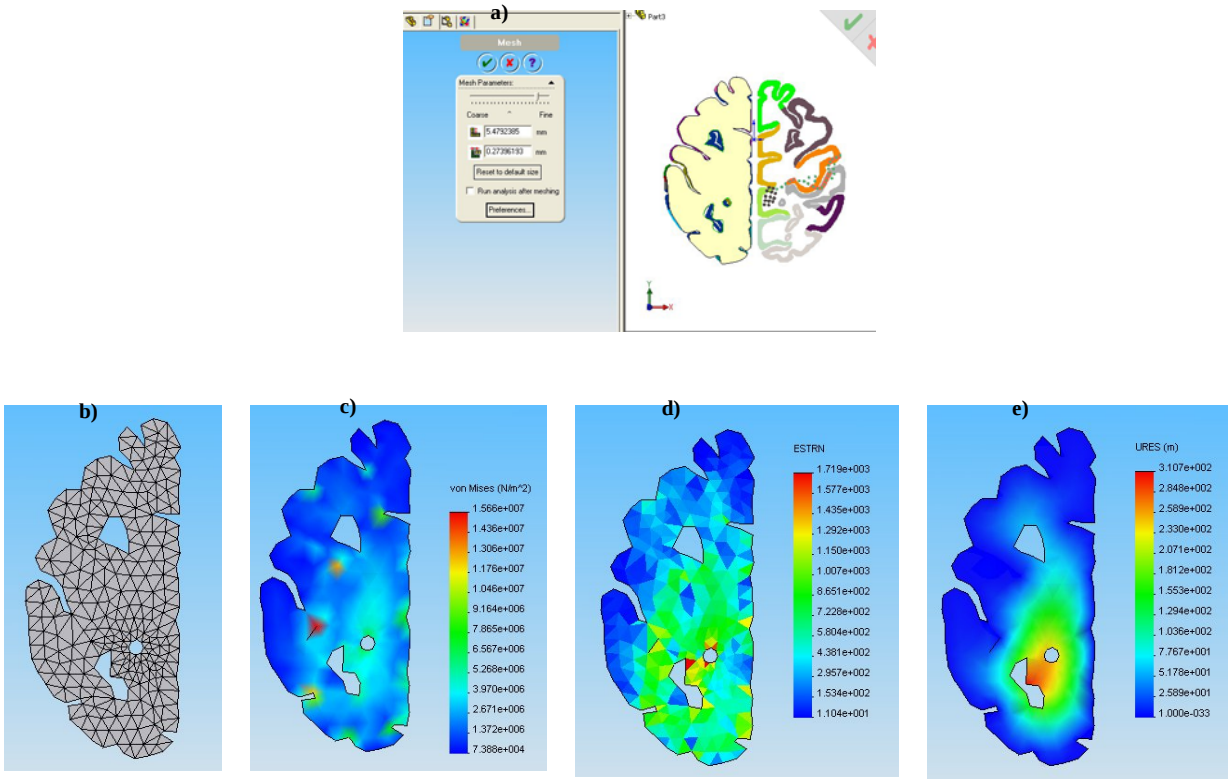

Figure 4.26 (a) Matching of cross section of the model with the atlas plate. (b) Construction of un-deformed mesh (c) Static nodal stress (Von Mises) distribution (d) static strain (e) static displacement in a sample simulation

The stress calculated with a coarse mesh was also about 5% higher than estimated with the finer meshes that fall within the acceptable range. The *error estimates*[30] on a single result case is also obtained. Following is the equation used to determine probable error applying the n*ormalized present maximum deference* method (Adams and Askenazi, 1998):

$$Error = \left| \frac{Stress_{Max} - Stress_{Min}}{Stress_{ModelMax}} \right| x100\%$$

[30] The error estimates in FE analysis refer to the relative difference between results across an element edge or at a node.

The estimated nodal error for a particular node (node 92 : X =-30.0634, Y= -30.6055, Z=55) : 0.128 which is well within the reasonable limit. The error estimation was calculated later more precisely using grid-invariance tests which is the standard practice for grid convergence index and Richardson Extrapolation. Richardson's extrapolation formula for error estimate can be defined as (Brezinski & Zaglia, 1991):

$$\int_a^b f(x)dx - A_{2n} \approx \frac{A_{2n} - A_n}{2^r - 1}. \tag{4.4}$$

Where r is a real number that can vary; for example: r = 2 for the Trapezoidal Rule and r = 4 for Simpson's Rule. If we denote A_n to be either the sum of the definite integral from the Trapezoidal Rule or the sum from Simpson's Rule.

4.9 Examples of Applications of the Proposed Model

Since newly built physics-based atlas has several advantages (such as high parcellation of structures, 3D models of detailed anatomical structures with fine mesh, option to choose martial properties etc), it has a potential to offer new possibilities for clinical practice, biomechanical research and medical training. The typical potential applications may include modeling the brain for surgical simulation, prognosis of diseases such as tumor growth and hydrocephalus, intraoperative computations (such as brain shift), patient specific operation planning, simulation for needle insertion for deep brain stimulation etc. These applications need proper knowledge of biomechanical tissue behavior in terms of nonlinearity, registration, boundary condition etc which often become crucial for real time simulation of many clinical applications. In many applications the surgeon relies on his expertise and operates with only a mental map of anatomy and pathology. Thus any relatively modest navigation

accuracy and tangibility instead of relying on 'mental mapping' would still be a significant improvement. One possible suggestion is to use physics-based biomechanical models. As a starting point for the purpose two applications of PBA have been described. These are illustrated in the following sections.

4.9.1 Investigation of Brain Deformation Behavior

Starting point of the mathematical derivation is the assumption that brain tissue can be considered as hyperviscoelastic material, i.e a material whose response function is determined by an existing stored energy function. The related mathematical formulation has been shown in the chapter 2 (section 2.3.5).

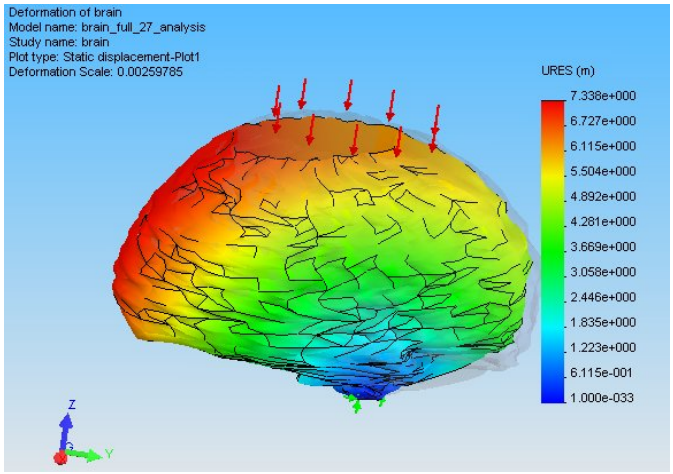

Figure 4.27 Visualization of deformation after applying a uniform load in a specified area

The small strain Young's modulus is considered identical in this study. It has also been observed that brain tissue is best suited with analytical result for C_{10} and C_{01} = 0.9: 1. As the bulk modulus of brain has been found to be about 10^6 times higher than the shear modulus, equation (2.34) gives the instantaneous value of material constant $d_1 = 1.9011e^{-9}$. The values are used as nonlinear material properties or special element input in *ANSYS*.

Physics-based application of our model in a scenario where uniform load at 1 mm per second indentor speed on the top surface of the brain (Area: 3784.34 square millimeters; Perimeter: 265.87mm) is simulated. The formulation of appropriate boundary conditions constitutes a significant problem in biomechanics of soft tissues (Miller, 2002a).

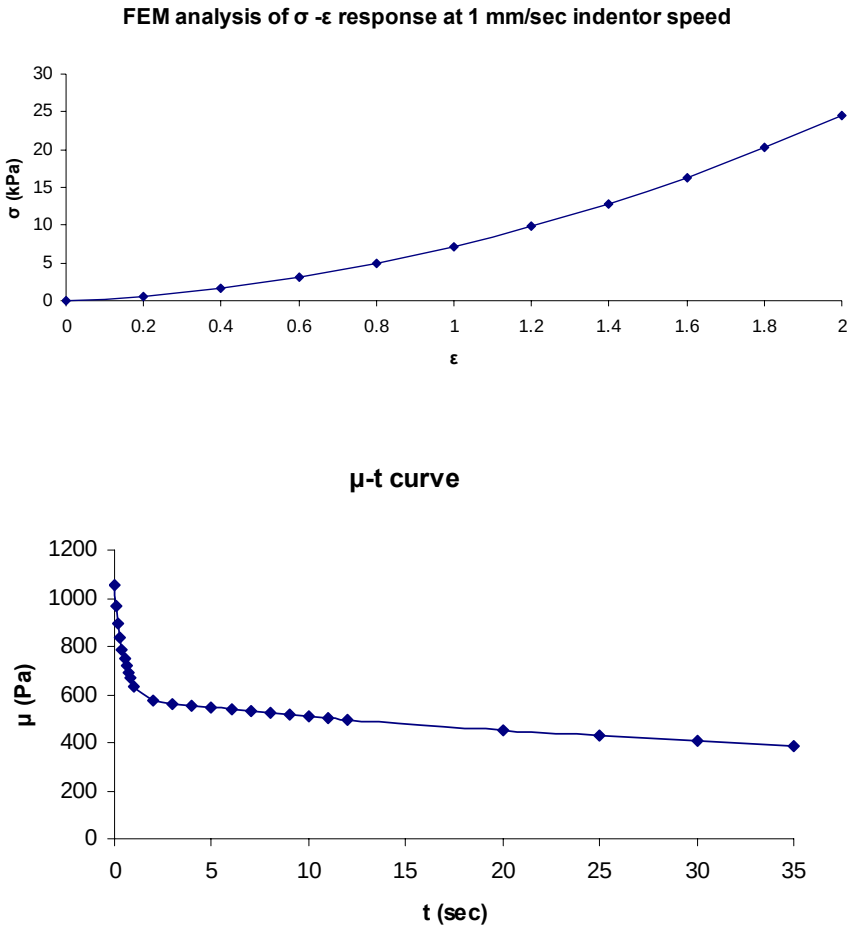

Figure 4.28 (a) Plot of quasi static stress response, (b) Plot of Shear Modulus with time from (Eq. 2.31); in the extreme case the shear modulus at infinitesimally small loading reaches approximately, $\mu_\infty \equiv 194.62$ Pa

A hypothetical scenario was constructed from where one can study the brain tissue behavior in compression due to the forces acting on the top of the brain by the surgical tools. As a crude approximation, the brain is assumed to be submerged in CSF, thus its

weight is considered to be neutralized by the buoyant force. It was also assumed that the bottom surface of the brain did not move, thus immovable (no translations) restraint has been set which confirms all translations on the specified plane to zero. The static displacement of the model has been illustrated in Fig. 4.27.

From equation (2.31), limiting case of the constitutive model can be determined. For instance, assuming $t \to \infty$, the equilibrium elastic behavior can also be obtained by substituting $\mu_\infty = \mu_0\{1-(g_1+g_2)\}$. The values of g_1 and g_2 are taken from Table 1 listed in Miller and Chinzei (2002b). So, the shear modulus in undeformed state at infinitesimally small loading can be achieved approximately, $\mu_\infty \equiv 194.62Pa$ that exhibits the similarity with a hydrocephalus condition (Miller, 2004). Fig. 4.28(a) shows the predicted true stress for the elastic model with large deformation. Equation (2.31) gives the time dependent relaxation component of Eq (2.32) that has been plotted in Fig. 4.28(b).

4.9.2 Modeling of Tumor Growth

As an extension of our work with the *Cerefy* Brain Atlas, a macroscopic, primary brain tumor growth model has been developed, incorporating the biological and biochemical factors that affect in vivo neoplastic growth. Tumor growth causes a substantial brain deformation and change stress distribution in the tissue as well as CSF flow. Previously, a preliminary sample simulation scenario was conducted to determine the effects of the tumor growth (Miller et al, 2005a). The tumor was hypothetically modeled as a 2D rigid circle of 3 cm diameter and the simulation of effect of tumor growth on the brain, pore pressure distribution and magnitudes of flow velocity has been determined. However, a lack of realistic and pathological data was a

shortcoming of the work. In the present analysis, following steps are performed (illustrated in Figure 4.29) to modify the work:

1. Segment the loaded RAW tumor data[31] based on radiological (intensity) characteristics.
2. Create 3D volume of the tumor from the segmented contours.
3. Load volumetric mesh in FEM software (*COSMOSWorks* /*ANSYS*)
4. Simulation to determine the effects of the tumor growth. The effect includes the normal and shear stress/strain and deformation of brain structure due to pore pressure distribution.

The tumor was identified and initial segmentation of tumor was done in *Multiplaner Editor* (Su H et al, 2004) to generate contours of a continuous 3D model for the structures without breaking the consistency and continuity of the surface. The software uses the *region growing* algorithm for the segmentation of tumor. The algorithm is used for segmentation of tumors in recent work of Nowinski and Belov (2005).

For the selected region, the system basically calculates the mean value μ and standard deviation σ of the intensity and creates a resulted intensity range $[\mu - C\sigma, \mu + C\sigma]$, where C is a constant. After extracting the boundaries, 3D model of the tumor (surface area 2517.948 mm^2 and perimeter 47.53 mm) has been generated in the same way we constructed the entire brain model (Fig. 4.29b). Fig. 4.29d presents

[31] The tool for conversion of DICOM format to 8bit RAW format belongs to Biomedical Imaging Lab and can be downloaded from the following site: http://www.cerefy.com/ ; Narayanaswami B, Aziz A, Ananthasubramaniam A, Lim T, Nowinski WL, Multi-media Based Medical Image Discussion Forum, CODE: 9149 DS-I, RSNA 2005, http://rsna2005.rsna.org/rsna2005/V2005/conference/event_display.cfm?id=66601&p_navID=272&em_id=4409601

the FEM analysis of the brain with a tumor. The analysis shows the deformation of the brain for the pore pressure distribution within the brain.

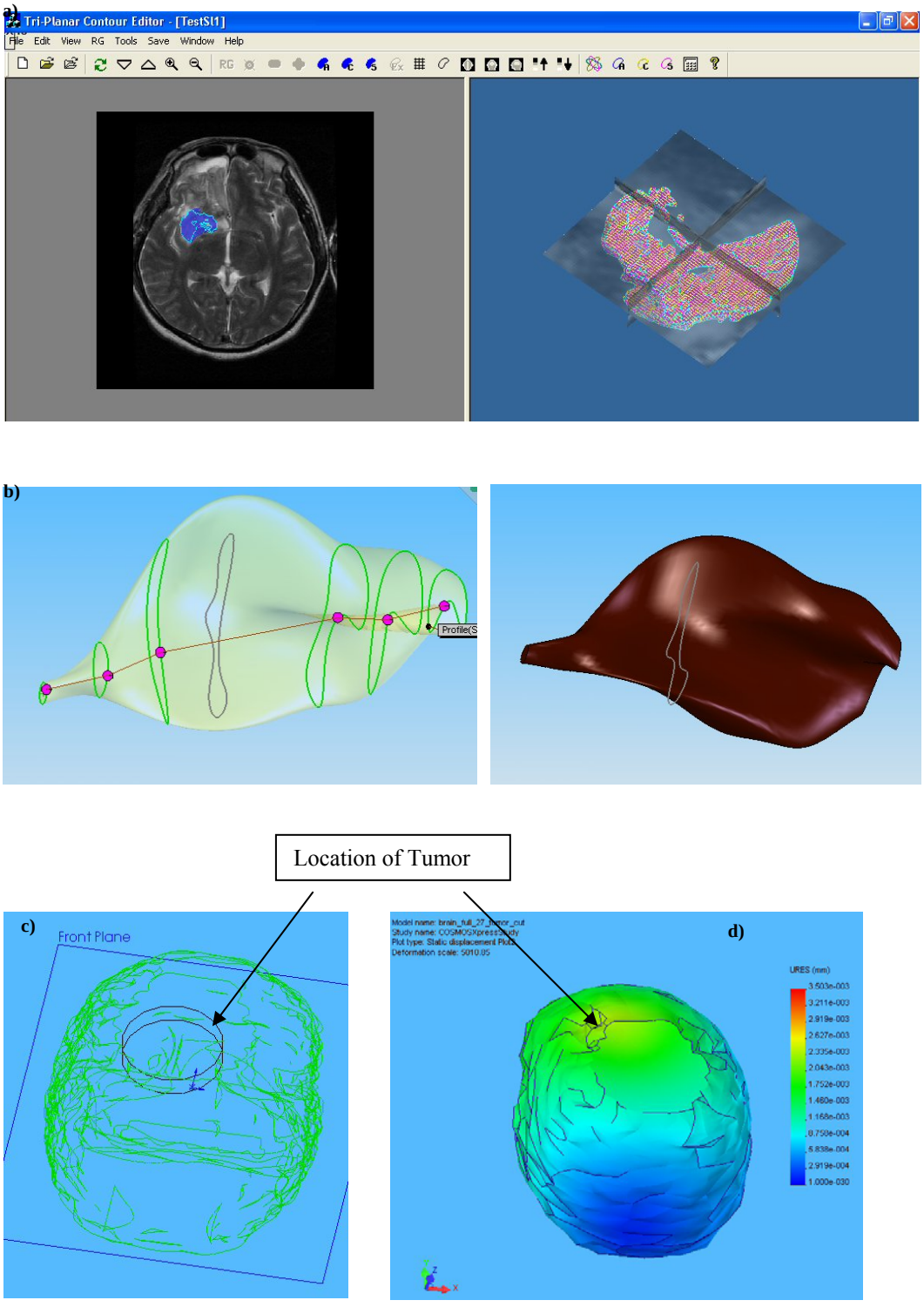

Figure 4.29 (a) Identified tumor in Multiplaner Editor (top), (b) 3D model of tumor after extraction (middle), (c) demonstrated in wire frame model, (d) FEM analysis of the effect of tumor growth on the brain (bottom)

The tumor data has been incorporated in PBA after determining its position precisely with relation to multi-structured 3D atlas. The cross section of PBA with tumor has been shown in the following figure (Figure 4.30).

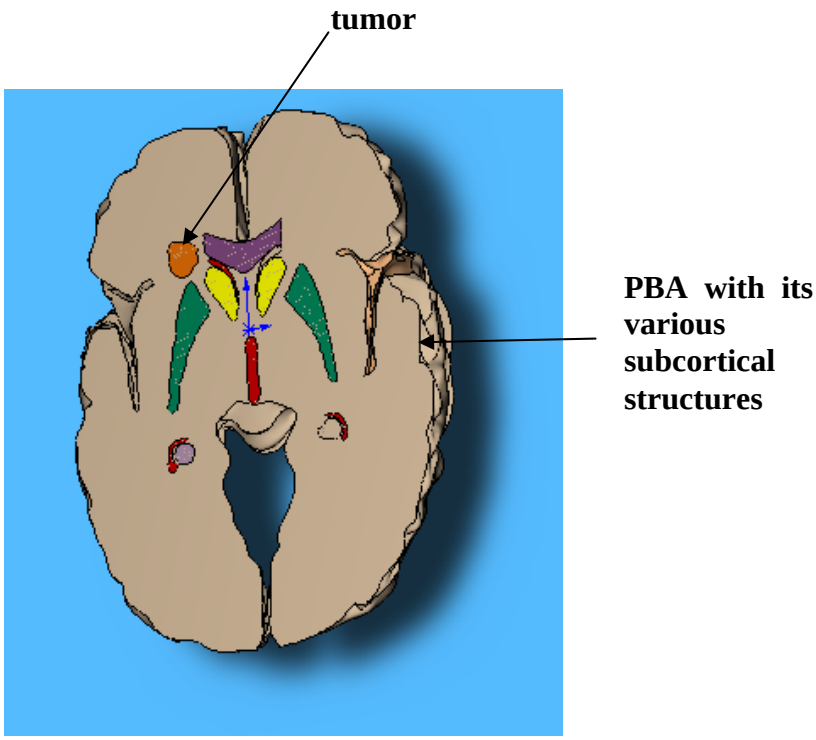

Figure 4.30 Tumor volumetric model acquired from MRI image has been incorporated to PBA [The model has been created using the same technique described in chapter 4 (section 4.6 and 4.7)].

In this analysis, the effect of tumor growth is modeled in the form of displacement of contact nodes of the brain having a tumor inside. From the point of view of surgical simulation, the brain can be considered a single-phase (multistructured) continuum undergoing large deformation. Stress-strain distribution inside the brain is calculated based on the deformed configuration (moving boundary). Distribution of stress due to tumor growth in the brain indicates a nonlinearity of the stress in radial direction. The

stresses and strains were measured with respect to the current configuration. Thus, energetically conjugate Almansi strain and Cauchy stresses[32] were used.

Since there is virtually no data on mechanical properties of brain tumor are available in the literature (Wittek et al, 2006), some realistic assumptions are made prior to perform the analysis. It is commonly assumed that tumors are associated with "stiffer" tissue, even though specific criterion is not available. As the volume of the tumor is very small as compared to the volume of the entire brain, tumor can be simulated using the same constitutive hyperviscoelastic model (chapter 2, section 2.3.5) as normal brain tissue with an exception that tumor having stiffer material properties. In this analysis, the instantaneous shear modulus of tumor was assumed two times higher than that of brain tissue. The permeability is taken as, $k = 1.59 * 10^{-7}$ m/s, and Poisson's ratio, $\nu_{solid} = 0.35$ are obtained from Kaczmarek et al (1997).

4.10 Results and Discussion

In this chapter a framework a newly developed Physics-based Atlas (PBA) has been proposed. The developed atlas has several advantages including highest parcellation of structures and realistic 3D models of brain anatomy. The proposed 3D meshed atlas is of vivid clinical and research importance, particularly in identification of brain structures and their deformation in different boundary conditions. A prospective application of brain biomechanics is in realistic surgical simulation (Roy et al, 2004b) at moderate strain rate (strain rate between $0.001s^{-1} - 1.0s^{-1}$). Our simulation study has indicated to measure the ability of biomechanical deformations of the brain

[32] Kindly refer to the second chapter (section 2.3) of this dissertation.

and individual sub-cortical structures. The extreme case for an infinitesimally small loading has also been obtained that exhibit similarity with hydrocephalus (Miller, 2004). In contrary to existing brain models that are simple, homogeneous or constructed with few structures employing simple linear elastic properties, we have developed a multi-structured detailed 3D human brain model in conjunction with a non-linear hyperviscoelastic material. However, in author's opinion, further experimentation may be needed to examine the assumptions lying behind the construction of meshed atlas with multiple subcortical structures. The next chapter will focus on one of our own efforts to investigate material properties and other underlying assumptions through in-vitro indentation experiment.

Our proposed meshed model is composed of 10 node 3D parabolic (quadratic) tetrahedral solid elements (SOLID187). One may argue that brick-mesh could have provided more accurate results closer to converged solutions, however, according to the authors' view the simplification required to build a brick mesh cancel out any element accuracy issues when compared to second order tetrahedral mesh with little or no simplification. Moreover, the accuracy in biological soft tissue simulation does not entirely depend on what type of mesh-element has been chosen, but also depends on the material properties and boundary condition. Taking into account the large variability inherent in biological tissue, even 31% error level (in analyzing force-displacement curve) can be considered as "almost perfect" reproduction (Miller, 2002a). Therefore, we were more concerned for the geometrical correctness, cleanliness and convergence of the model instead of type of mesh being used.

With the efficiency and quality of good automeshers (*CosmosWorks* and *ANSYS*), we tried to ensure a clean CAD geometry of the brain. However, ensuring that mesh of each structure is clean with good quality elements and that the final mesh has been converged on the desired behaviors is always a difficult proposition. Some heuristic approaches were taken to address such issues. In CAD practice, poor fringe quality usually gives poor sign of poor solution convergence. If the mesh is too coarse, usually refining the mesh in the problem areas help the model converge. As the converging mesh a less than 5% change in results between high dense and coarse mesh is an acceptable criterion, we set our goal of satisfaction and reliability based on the assumption. In the same manner we have set a quantitative target for geometrical validation. The error limit ε was set as 0.65 mm for both average or mean sectional error (for each cross section), and for percentage error (for each structure) of final geometry for the comparison of 2D cross section with atlas data. The choice was based on our experience with handling atlas data and biological soft tissue. We experienced any limiting value greater than this could make the model more error prone. If we set a value less than 0.65 mm, it will make the entire validation process too cumbersome, and too time-consuming - hence becomes impractical[33].

[33] The study was carried on considering the limiting values of 0.50, 0.65 and 0.70 mm. For the value of 0.50, huge numbers of structures including Corpus callosum, Cortical areas, Globus pallidus, Middle temporal guyrus, Nucleus caudate, Nucleus rubber, Putamen, Thalamus, Ventricles fall far behind reaching the goal even after fine remeshing and adaptive meshing with a very precise geometry. Again, if we set the error limit at 0.70, no reconstruction needed for any single structure, hence the system would become more error prone. Conducting a close and systematic examination, we set the error limit at 0.65 which had built an objective realm to attain the proper verification of the model.

It is to be noted that a slicing sequence of axial images would lead to distorted elements at the crown regions, in fact in some cases (for example in some subcortical structures such as Corpus callosum, Caudate nucleus and Ventriculus and top most cortical areas of the brain) it did. Nevertheless, the problem was solved by adopting several efficacious techniques. We have cross-verified the model with coronial and sagittal Atlas data to check whether any constructed structure came up with any unrealistic shape. For example, to construct the entire Corpus callosum structure coronal and sagittal data has been incorporated later on. Below are the three views of 4th Slide of Cerefy Brain Atlas [Fig. 4.31 (a, b, c)]. These slides are used to study and construct the correct shape of the complex structures [Fig. 4.31 (d)].

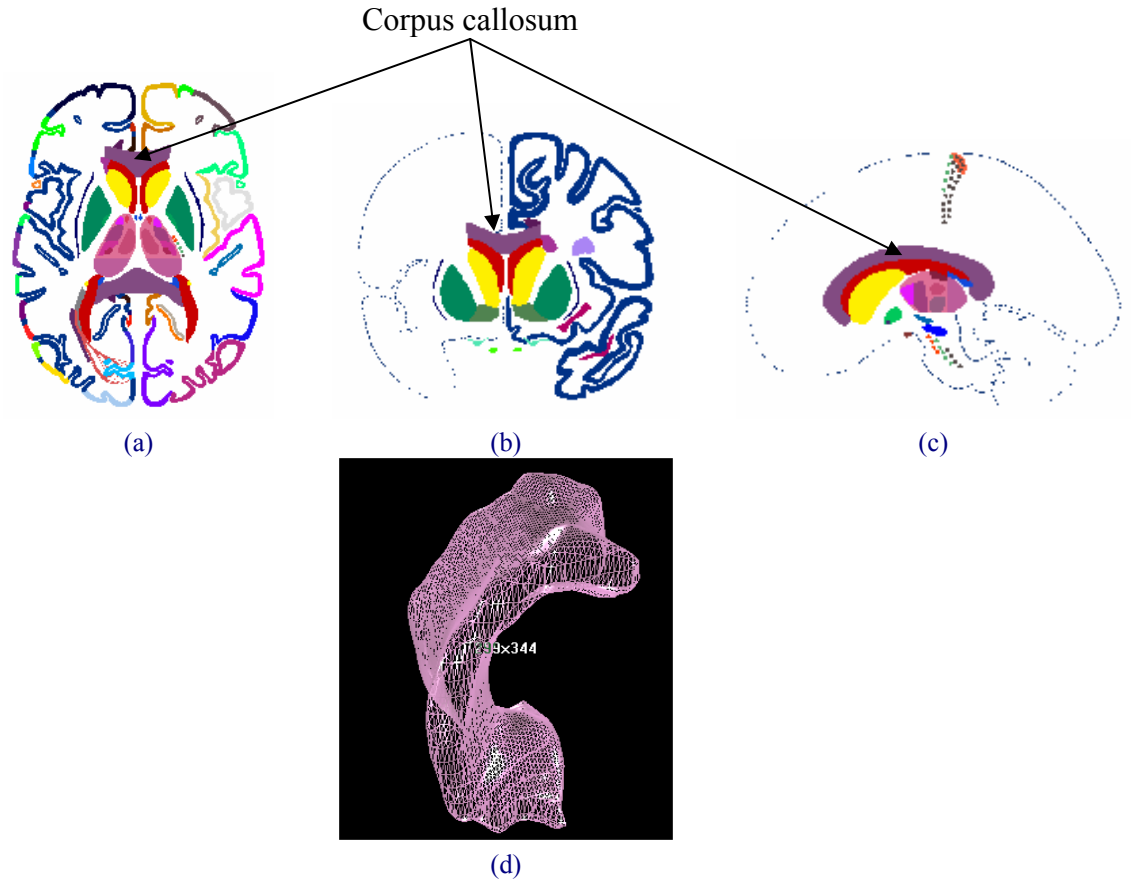

Figure 4.31 (a) Axial, (b) Coronal and (c) Sagittal view of the brain. The PBA has been built upon axial slides where as coronal and sagittal slides are used for structural verification. (d) Corpus callosum has been constructed after verification.

As a last step, topological improvement and Laplacian/Optimization based smoothing (Canann et al., 1998) was done which further reduced the possibility of having distorted structure(s). More detailed picture of the subcortical structures and the entire meshed model has also been presented in Appendix VI.

We have also conducted a computer simulation of the effects of tumor growth and demonstrated the deformation of brain for the pore pressure distribution. However, the accurate analysis requires the accurate biomechanical properties of tumor tissues to be known. We were not in the position to measure the tissue properties for the individual patients by any means. Few literatures provide some ranges for these parameters; they are found contradictory (Nowinski and Belov, 2005). Thus, it was not possible to validate the results; at this moment, we present a generic procedure for simulation of the effects of the tumor growth through FEM-based biomechanical modeling just for research application, rather than a method of choice in the clinical setting. In addition, several novel solutions to analyze structural diseases such as hydrocephalus, and Parkinson's along with tactile feedback system have been introduced for various atlas-assisted applications. Integration of computational biomechanics also offers newer and newer possibilities for clinical practices, such as control of surgical robots, intra-operative computation of brain shifts, patient specific operation planning, prognosis of the development and the effects of diseases, training and education (Roy et al, 2004a, 2004b, 2005b, 2006a; Miller et al, 2005a).

4.11 Summary of the Chapter

We have developed a multistructured physics-based atlas with highest anatomical parcellation. The newly developed atlas showed its potential to analyze the deformation of brain in a specified biomechanical condition. The simulation of a

primary brain tumor has also been illustrated in this chapter. The portion of work described in this chapter has been published in Roy et al (2006a and 2004a). The next chapter will focus on the indentation experiment on brain tissue to investigate its properties.

Chapter 5

EXPERIMENTAL WORK ON SOFT TISSUE

5.1 Investigation of Material Properties of Brain

Since material property plays a major role in FE modeling, the mechanical properties of the brain have been the subject of investigation for a considerable period of time. Mechanical properties of brain tissue have been measured in vitro under compression, tension, shear and oscillatory loading (Ommaya, 1968; Galford and McElhaney, 1970; Shuck and Advani, 1972; Mendis et al., 1995; Bilston et al., 2001; Miller and Chinzei, 1997, 2002; Prange and Margulies, 2002). The extensive determination of the mechanical properties of brain tissue at large strains, including the effects of region, direction, age and species, represents a major step forward in our understanding of the response of the brain during traumatic events and neurosurgical cases. As the existing material properties testing were mostly for research on the impact analysis of the human brain, where the strain rate is much higher than for surgery applications, related data available for surgical biomechanical modeling is very meager. As such, we propose to compare and analyze the limited data available in the literature, and furthermore carry out our own experiment to account for the particular neurosurgery situations. Since the brain models are to be used to study human brain, it is worth having to obtain experimental data using the samples of fresh human brain. However, due to ethical issues involved, it was reasonably not possible to experiment on fresh and intact human brain tissue during the course of the research. Even treated human brain tissue, preserved or chemically fixed, was not available. Furthermore, there is still little known about the effect of the preservation on the viscoelastic properties of

the brain tissue. A study reported by Metz et al (1970) on Rhesus monkey showed that after fixing with 10% formalin through the circulatory system, the modulus of elasticity of the brain was increasing by almost 100%. They observed no change in the qualitative behavior of the stress-strain curve though. Since their model was elastic it was not possible to quantify the changes in viscoelasticity of the tissue. Due to difficulty in obtaining human brain samples, porcine tissue is quite often used as a substitute for brain material testing (Thibault and Margulies, 1998, Brands et al, 1999; Miller and Chinzei, 1997, 2002; Prange and Margulies, 2002) for a long time. We have also decided to conduct our own in-vitro indentation experiment on porcine brain tissue in Biomechanics lab of National University of Singapore in order to investigate the material properties of brain. As the experimentation in National University of Singapore was done almost immediately after the sample collection, we did not need to store in a refrigerator or in any physiological saline or any other chemical solution.

5.2 Compression Experiment on Porcine Brain Tissue

5.2.1 Sample Procurement and Preparation

The five adult pig brains were collected from a slaughter-house near Clementi, Singapore. The pigs were terminated according to the standard slaughtering procedure and the samples were taken as by product. The specimens were not frozen at anytime during the procedure. The brain weights ranged between 100 grams and 110 grams. After removing the brains from dura, each brain was stored in a polythene packet without using any chemical solution. Transportation of brains to the Biomechanics Lab of National University of Singapore and starting experimentation took approximately one hour.

5.2.2 Experimental Set-up

Indentation is considered as a well-established method for characterization of mechanical properties of soft tissues for long (Lai-Fook et al., 1976, Miller et al., 2000, Vannah and Childress, 1996, Gefen and Margulies, 2004). In this method an indentor is pressed against the tissue and modulus of elasticity and shear modulus etc. are calculated from the applied load and extent of tissue deflection. The vitro indentation experiment was conducted on five adult pig brains using the facility in Biomechanics Lab, the division of Bioengineering of National University of Singapore (NUS), in accordance with ethical guidelines on animal experiments (Figure 5.1). As the brains were kept in a rigid glass bucket of flat surface on Instron Microtester, we assumed that the bottom surface of the brains did not move. Therefore, all nodes on this surface were assumed fixed. The top surface, however, moved when the velocities (0.05, 0.5 and 1mm per sec) were applied using a flat end surface shaft of 6 mm diameter, so this surface was left free to deform. No constrains were put to restrict the deformation of the side surfaces as well. The experiment confirmed tissue nonlinearity and inhomogeneity.

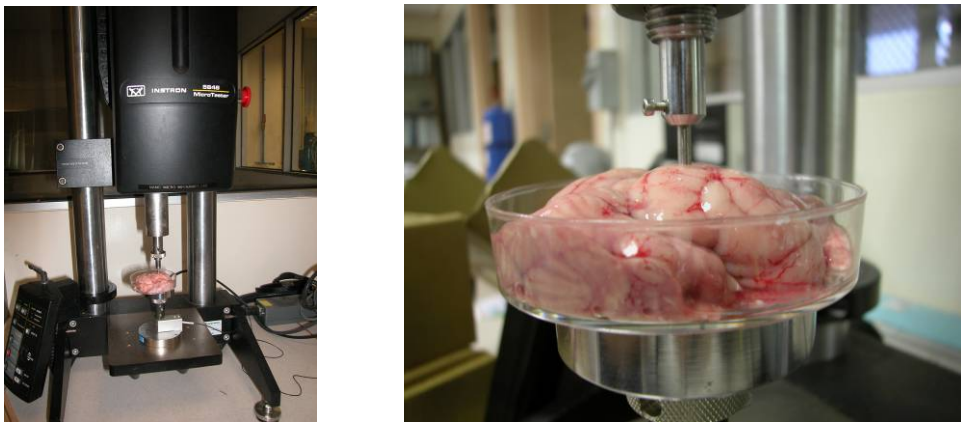

Figure 5.1 Experiment setup for indention test of porcine brain tissue

The general behavior of the pig brain samples under compression showed the general nonlinear features typical of the soft tissues. Deformation of brain tissue has

been simulated in a scenario where uniform load at 0.05, 0.5 and 1mm per second indentor speed on the top surface of the brain is applied. The force predicted by the finite element model based on quasi-liner, hyperviscoelastic constitutive equation (see chapter 2) for brain tissue, at the maximum indentation of 4 mm has been compared.

5.3 Result and Analysis

A series of measurements have been conducted on five samples of pig brain using the above set up. The shaft (needle) was moved vertically at constant velocity to compress the brain. The force modulus exerted onto the load cell was measured and plotted against the needle displacement. Three different velocities were considered at 0.05, 0.5 and 1mm per second as mentioned above. For each velocity, five independent experiments were carried out. The stress-strain curve obtained from the experiment are concave upward for all compression rates and contain no linear portion from which a meaningful modulus of elasticity could be determined. Tissue response in observed to be stiffened with increasing loading speed, indicating strong stress-strain rate dependence. Simulation on the meshed model described in previous chapter was used for comparative analysis.

To achieve repeatability of the measurements, the Lagrange stress[34] vs. strain for each loading velocity is measured. Figure 5.2 shows the five experimental measurements on five samples. The best fit curve has been chosen after determining the mean value and standard deviation of five experimental results for each velocity (Figure 5.2 shows the curves for 1 mm/sec indentor speed).

[34] Lagrange stress: vertical force divided by initial cross sectional area.

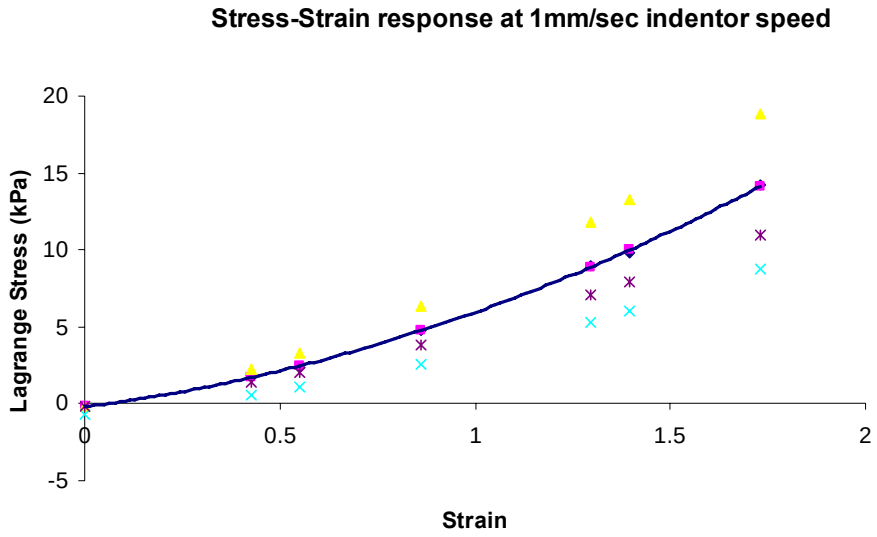

Figure 5.2 Repeatability measurement of Stress-Strain relationship at a loading speed of 1 mm/sec

The analysis shows that the assumption of hyperviscoelasticity in the theoretical constitutive model (see chapter 2 and 3) for brain tissue agrees well with the result obtained from our indentation experiment. Figure 5.3 shows the results of the uniaxial compression tests at 0.05, 0.5 and 1 mm per second speed of indentor on the pig brain tissue; it represents the plots of nominal stress versus nominal strain. The experimental result was also compared with some of previous experimental findings of researchers. The brain samples also confirms incompressibility which is commonly assumed (Estes and McElthaney, 1970; Mendis et al. 1995; Pamidi and Advani, 1978; Ruan et al., 1994b; Voo et al., 1996; Miller et al., 2000; Wu et al. 2004) in most of the theoretical work.

It can be observed that the standard deviation of experimental measurements is small in low deformations, illustrating the high similarity between the experimental curves, and grows higher deformations.

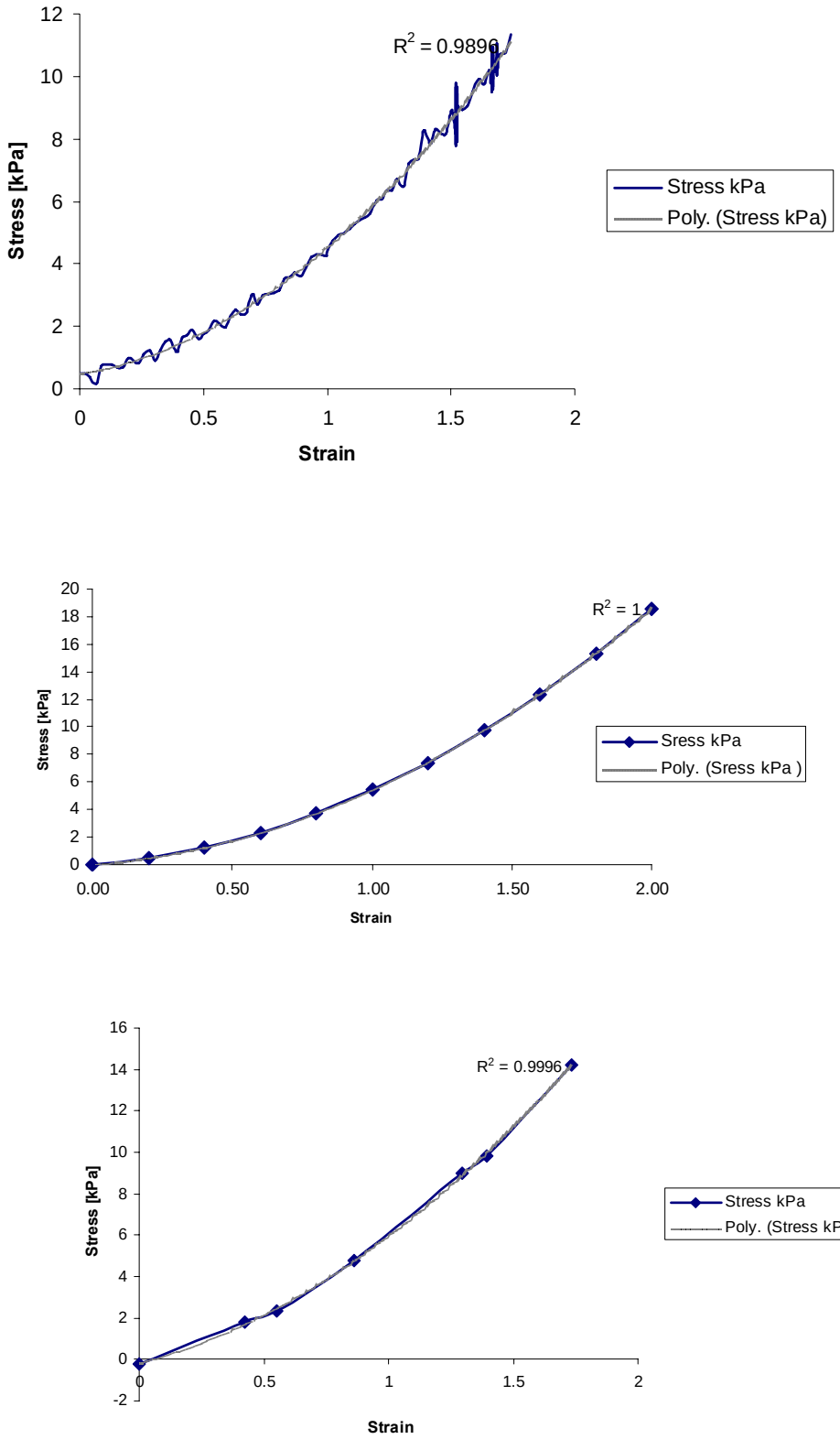

Figure 5.3 Stress-Strain relationship for 0.05, 0.5 mm/s and 1 mm/s indentation speed and 6 mm indentation diameter

The results showed in these experiments are significant. For a given velocity, all force curves showed a very similar trend, independently of the position, where needle was applied or of the orientation of the position. The result has been compared with Estes-McElthaney's (1970) experimental result. As the sample size (cylindrical vs. whole brain), loading condition (0.508 mm/s vs. 0.5 mm/s) and boundary condition were fundamentally different in two sources of experimental, differences in stress-stain relationship were observed though in both the cases tissue showed nonlinear, viscoelastic characteristics. Researchers found the properties can vary over 10-fold depending on the different testing methods and parameters, location, orientation and preparation of samples, interspecies differences, developmental age, and importantly, on postmortem conditions etc. (Gefen and Margulies, 2004). The difficulty was further compounded by obvious biological influences on material properties of test specimens and difference in indentor diameters, loading rates, and strain magnitudes. Postmortem alterations in neurofilament proteins (while brain tissue begins to deteriorate and at room temperature, 23 deg C), detectable 6 hours after death, are likely to affect the stiffness of cerebral tissue (Fountoulakis et al., 2001) but the course and extent of these changes are not yet clear. Comparing to Estes-McElthaney's cylindrical samples, the stiffness of the tissue of the whole brain was found considerably much lower. For example, stress observed at the indentation depth of about 3 mm, was found about 60% lower (Figure 5.4).

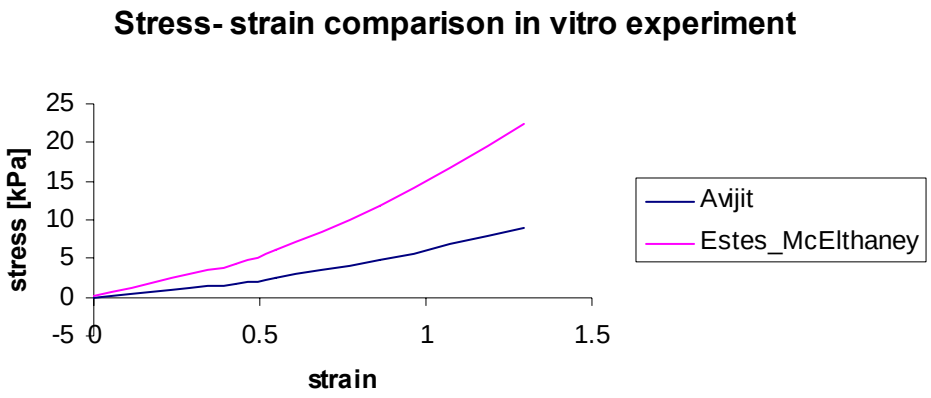

Figure 5.4 Stress comparison in vitro experiment

But how to use the in-vitro experimental results in more realistic in-vivo experiment remains a challenging task. Prange and Margulies (2002) showed that in vitro shear moduli of fresh porcine gray matter are fairly close (29% greater) to those of fresh human brain specimens with same harvest and test mode criteria, and both were an order of magnitude lower than properties measured in human cadavers after autopsy (Shuck and Advani, 1972). It has also been hypothesized that the pressurized vasculature of the brain plays an important role in determining its mechanical properties in vivo, and some researchers simulated and demonstrated that the presence of a pressurized vessel in a tissue specimen might be expected to increase apparent tissue stiffness (Bilston, 2002). The result of our in-vitro experiment has been compared to the in-vivo experimentation of Miller et al (2000). Miller and his collaborators performed one of such indentation experiment on the exposed living pig brain, and presented properties that were of the same order as properties obtained in vitro. In our in-vitro experiment we noticed a significant difference in stiffness of tissue in comparison to the result obtained by Miller's in-vivo experiment (Figure 5.5).

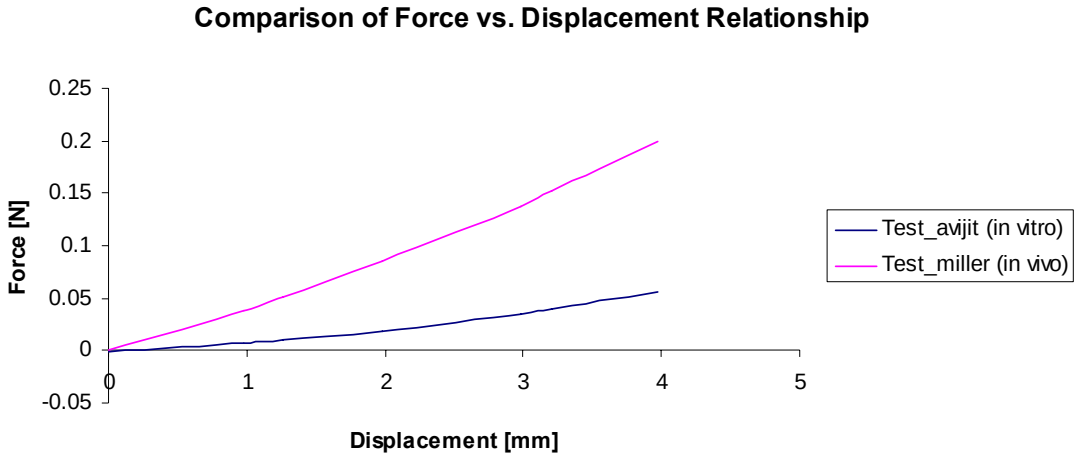

Figure 5.5 Comparison of force vs. displacement relationship in vivo and vitro experiment

We, therefore conclude that the present experimental data confirm the assumption of Bilston (2002) that claims to have apparent higher tissue stiffness in-vivo environment. The findings of the indentation experiment are summarized below:

Table 5-1 Summary of the indentation experiment at NUS

Criteria	**Observation and Result**
Specimen used	Porcine (pig) brain
Sample size	5
Test location	Biomechanics Laboratory E3-05-05 Division of Bioengineering National University of Singapore
Test date	September 29, 2005
Test type	Indentation (compression) experiment
Indentor speed (predefined)	0.05, 0.5 and 1 mm/sec
Testing apparatus	Instron Microtester (model no: 5848)
Indentation diameter	6 mm

Criteria	Observation and Result
Indentor tip geometry	flat
Boundary condition	Bottom part did not move, the other faces were left free to deform.
Maximum displacement (predefined)	4 mm
Maximum load (observed)	0.05633809 N
Maximum compressive stress (observed)	14.20712 kPa
Tissue Characteristics: Nonlinearity	High (hyperviscoelastic)
Tissue Characteristics: Incompressibility	High
Tissue Characteristics: Homogeneity	Inhomogeneous
Tissue Characteristics: Isotropy	Anisotropic (small scale)
Other observation	Stiffness increases with the increase of indentation speed

In author's opinion, more experimental work is required to verify the validity of such claims as the results in related study (Ommaya, 1968; Galford and McElhaney, 1970; Shuck and Advani, 1972; Mendis et al., 1995; Bilston et al., 2001; Miller and Chinzei, 1997, 2002, Prange et al, 2002) show differences over an order of magnitude in reported properties. Some of the contradictory reports (especially on stiffness of gray matter and white matter) are mentioned in chapter 3 (section 3.3.4). Such contradictory reports by researchers rather demand further close experimentation on the matter. No matter whether gray or white matter is stiffer, the researchers at least concluded that heterogeneity exists between differing regions of the brain (Coats and Margulies et al 2005), thus in author's opinion generic assumption of homogeneity of the brain should be carefully considered in future finite element brain models.

5.4 Summary of the Chapter

This chapter focuses on the indentation experiment on brain tissue to investigate the properties of brain. A portion of work described in this chapter has been accepted for publication in Roy et al (2006b).The next chapter will be discussing on construction of an automated mesh generator that will be helpful to visualize the meshed atlas in a Java platform.

Chapter 6

MESHED ATLAS TOOLKIT FOR VISUALIZATION AND CAD COLLABORATION

6.1 Background

For biological soft tissues mesh generation has always been a challenging issue due to high variability of in human anatomies and intricate morphological details. The widely used solid modelers and commercial FEM software (ABAQUS, ANSYS, CosmosWorks etc) have not made modeling of biological soft tissue any easier. Most of these FEM packages were initially built for solving various problems related to mechanical and civil engineering, not for dealing human anatomy. An additional difficulty is the anatomy often revealed in the form of atlas, MRI or CT image in medical science. There is no software available[35] that can produce CAD model for FE analysis from these images automatically. Moreover, modeling and design of complex anatomical organ such as brain needs excellent domain knowledge from various expertise and demands effective collaboration. The traditional stand-alone CAD and FEM packages do not address these prime issues. Thus demand for building a fully automated, knowledge-based, collaborative mesh generator for dealing soft tissue has always been a crying need. Today advancement in computer and information technology, appearance of various visualization and simulation technique including VR, various platform independent and object-oriented programming languages

[35] Materialize software MIMICS is a notable exception in this field; however it mainly focuses on scanner and MRI data, have not handled any atlas data till date.

including Java™ have been advanced in a dramatic speed opening numerous possibilities which can be used to build a quality meshed visualization toolkit. In this chapter of the dissertation a framework for developing a meshed atlas visualization toolkit, MAVT has been proposed that would

1. Build a virtual anatomy meshed models from atlas data automatically.
2. Incorporate domain knowledge of geographically dispersed users through effective collaboration.

In addition to solving various constitutive (biomechanical) problems with MAVT, it is expected the toolkit would also provide a sense of highly realistic representation of anatomy structures, which is very important for anatomical understanding for the students to solve various clinical problems (Dev et al, 1992; Warrick et al., 1996). It will also open avenues for research into brain biomechanics for investigating diseases (e.g., tumor growth, hydrocephalus), intraoperative support (e.g., registration), and surgical simulation for specific applications such as electrode insertion simulators for Deep Brian Stimulation (DBS) and computer assisted surgery planning (CASP) etc.

We have developed a multi-structured 3D biomechanical virtual anatomy CAD model using the *Cerefy* Brain Atlas database (see chapter 1 – chapter 4). The subcortical structures are first extracted from the atlas, forming feature points. The feature points of the individual structures are used to form point clouds in a CAD platform where the entire surface model is built. The data has been uploaded in Meshed Atlas Visualization Toolkit (MAVT) for the visualization in Java platform.

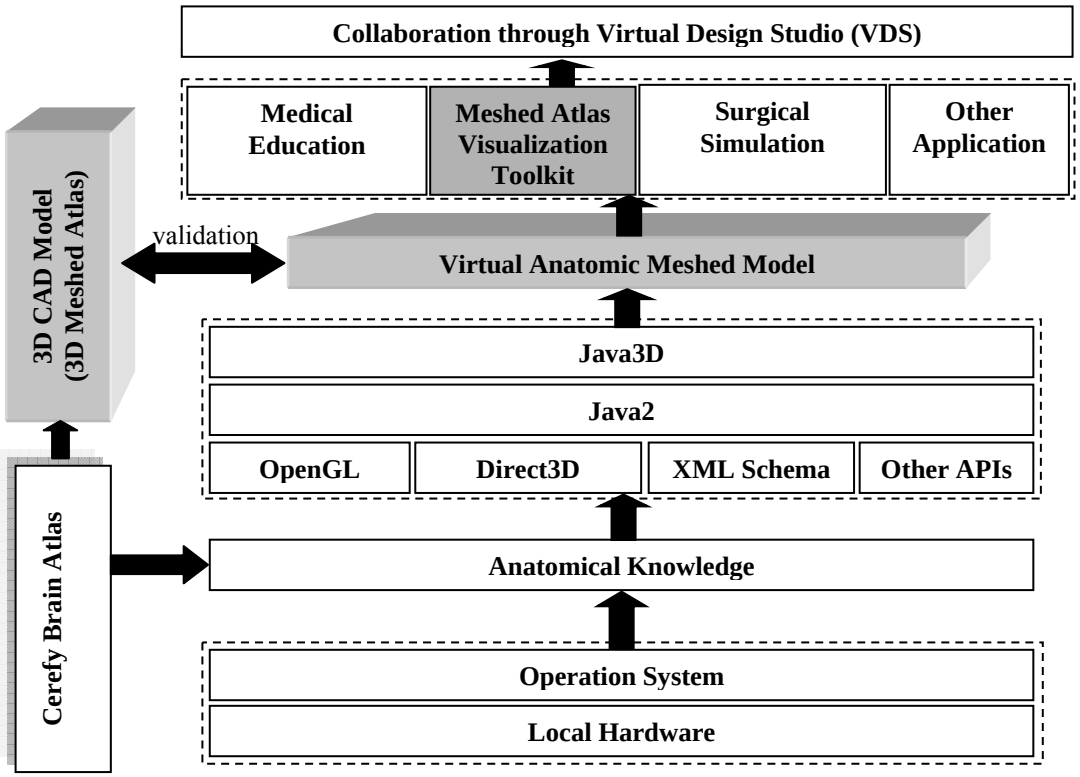

Figure 6.1 The architecture of the virtual anatomic modeling environment

Virtual anatomic models are quite complex and difficult to be presented by most of the existing 3D modeling language. One of the shortcomings of the existing modeling languages is that they are unable to store and present the anatomic information, as well as special anatomic structures (for example, tubular anatomical structures). They are also not flexible enough to meet the requirement of advanced education and simulation in terms of visualization and interaction. Hence our objective is to build a framework which defines a suitable data schema for presenting virtual anatomy models and meanwhile builds an interactive modeling environment for direct manipulation of the virtual anatomic models. Figure 6.1 shows the architecture diagram of this framework.

This environment will serve two purposes, first for building virtual anatomic models interactively; and second to be used for prototyping of medical educational or simulation applications.

Depending on the application methodology of the anatomy models, their organization may vary quite significantly. In addition, during the procedure of simulation for education, the organization might be required to change from time to time. Therefore, the function to interactively re-organizing and re-structuring is useful and important. Both the foundation data structure and the GUI take into account this requirement. On the other hand, depending on the objective and interaction conducted in simulations, models of different modality may be invoked simultaneously or individually and modified now and then to get a better understanding of the anatomy relationship and realistic simulation. That means the visibility and appearance property of any sub-models of individual structures or different modalities need to be manipulated by users easily.

Collaborative product development (CPD) of various kinds has recently emerged as an effective means for the enterprises to remain competitive in today's global market. The progress in information technologies, especially through the advancement of Internet enables efficient cooperation, communication, and coordination in CPD involving geographically dispersed users (Roy, 2000; Tay and Roy, 2003). There has been a significant growth in collaboration software products and services, which perform a variety of tasks, from scheduling, teleconferencing, project management, to data management, information exchange, and applications integration. Various kinds of collaborative computing software have been built to facilitating the commerce

activities in procurement and logistics that involves sophisticated interactions among product designers as well as with end customers (Chu, 2006). However, the technology of the Internet-based product design so far has been more concerned with collaborative CAD tools (Tay and Roy, 2003; Li et al, 2005; Chu et al, 2006) and the Web-based PDM systems (Roy and Kodkani, 1999). Currently there are also few software available that can generate FE meshes from patient specific radiological images, nevertheless, no *collaborative mesh generator* has been built yet. MIMICS (Meterialise, Ann Arbor, MI), for example seems to have an automated method to translate CT or MRI data into full 3D CAD and Finite Element meshes; however it is still confined to stand-alone system. Some in-house semi-automated and fully automated methods for model generation have been investigated; Ferrant et al. (2000), Miga et al. (1998), and Hartmann and Kruggel (1999) have written their own mesh generator, however no collaborative feature has been included so far. In this chapter development of a framework of a collaborative mesh generator has been described that has borrowed the concept of a previously developed collaborative CAD system, CyberCAD (Tay and Roy, 2003) and modified for the purpose of distribution and collaboration through Meshed Atlas Visualization Toolkit (MAVT). It focuses on the distribution of 3D Brain model (CAD data) among geographically dispersed users and expands them to support remote design activities.

This chapter mainly focuses on two aspects 1) Visualization of 3D brain model (meshed atlas) and 2) Distribution of the developed model through synchronous and dynamic collaboration between geographically dispersed users. To visualize virtual anatomic models we have built a framework that can be used in standard Computer-Aided Design (CAD) platform as well as in Java platform. This framework includes

the foundation data structure as well as an interactive environment for manipulation of the anatomical models. The foundation data structure is designed for presenting structural and topological anatomy with multi-modal data models. Anatomical knowledge has been incorporated in the model schema design especially building intracranial structures. The interactive environment is designed to manipulate the virtual anatomy in the way that medical education and simulation required. Recently, the aspects of modeling issues involve various advanced technologies, thus design and distribution is more fuelled and successful because of the current development of IT, such as introduction of Java, .Net, Web, XML and Web service technologies. We have developed a Java-based co-design CAD system can effectively support co-modeling and co-modification functions and can distribute it among the geographically dispersed designers. Thus, in addition to creating an interactive 3D simulating environment, the developed VR tool can also distribute the entire design work to various geographically dispersed users depending upon their domain knowledge.

6.2 Modeling Operation and Visualization in CAD Platform

CAD system has been viewed as a tool only for mechanical or civil engineers. Early CAD/CAM systems focused only on improving the productivity of draftsman (Roy, 2000). But from last three or four decades, they are compelled to focus on modeling objects. *SolidWorks*™ has become the standard CAD software for medical device manufacturers since long. Yet, constructing a complete brain model using SolidWorks was a major challenge for us. We decided to develop a Physics-based model using Solidwoks as its ease of use and intuitive nature that allow designing rapidly and modifying parts and assemblies. The model was created mainly using a tool called *loft* (the detailed description of the construction of 3D model is given in

chapter 4). The concept is later successfully implemented in MAVT module (see Appendix IV). In addition to the *loft*, several other operations have been performed for the construction of the model; four of these important operations that have been used in Meshed Atlas visualization toolkit are stated below:

- **Intersection:** The purpose of the operation is to obtain the intersection part of two input shapes. For example shape A intersects with shape B to obtain shape C is denoted as : $C = \mathrm{A} \cap \mathrm{B}$
- **Cut (subtraction):** The purpose of the cut is to obtain the subtraction part of the original shape subtracted by the destination shape. For example, shape A is subtracted by shape B to obtain shape C is denoted as $C = \mathrm{A} - \mathrm{B}$
- **Difference:** The purpose of difference is to get the resulting shape that does not intersect with any of two shapes. For example, when shape A differences B to obtain shape C, the result denoted as $C = \mathrm{A} \cup \mathrm{B} - \mathrm{A} \cap \mathrm{B}$
- **Combination:** The purpose of combination is to obtain the sum of two shapes, which can be denoted as: $C = \mathrm{A} \cup \mathrm{B}$

Figure 6.2 shows one of the processes for the construction of 3D model that involves subtraction operation. Figure 6.2(a) represents a model with initial contours of the solid part that has to be subtracted. Figure 6.2(b) shows a solid part that has been formed (shown in green color) using the contours. In Figure 6.2(c), the subtracted 3D solid model has been shown.

a) b)

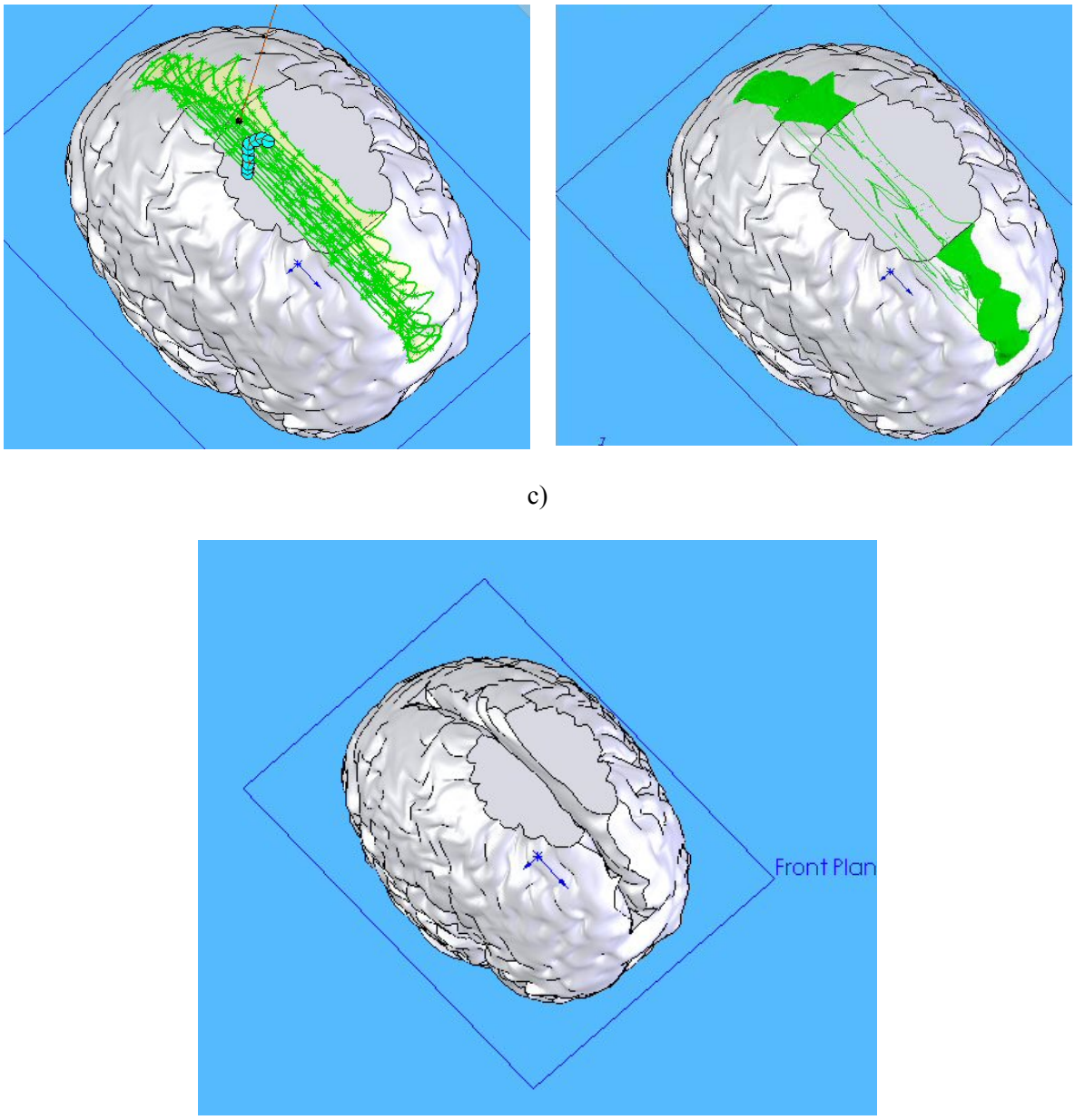

c)

Figure 6.2 Cut (subtraction) operation for constructing a 3D model

The solid modeling is one of the most important and attractive modules in today's CAD based application. The feature provides a high-level function layer module based on many basic modules. It also provides the necessary modeling functionality to the users such as Extrusion, Protrusion, Sweep, Revolve and Fillet etc. In addition, the solid modeling module provides the user with 3D Boolean operations like intersection,

subtraction and difference in order to enable the users to create some complex objects. In addition to the 3D Boolean operation, basic 3D primitives are developed with Dynamic 3D Sketching methodology in order to let the users access the CAD 3D functionality easily and quickly. Many design activities require the design of complex object beside the primitives and the models extracted from 2D shape. A common way to get this complex object is through Boolean operations, whereby the final complex object is obtained from the combination of two or more objects. *Anti-Solid Algorithm* (ASA)[36] is specially designed and is used in Boolean operations on 3D models. This solves a common problem in Anti-Solid is subtraction. In handling the specific problem, the subtracting solid is called the Anti-Solid. Figure 6.3 illustrates an example for subtracting.

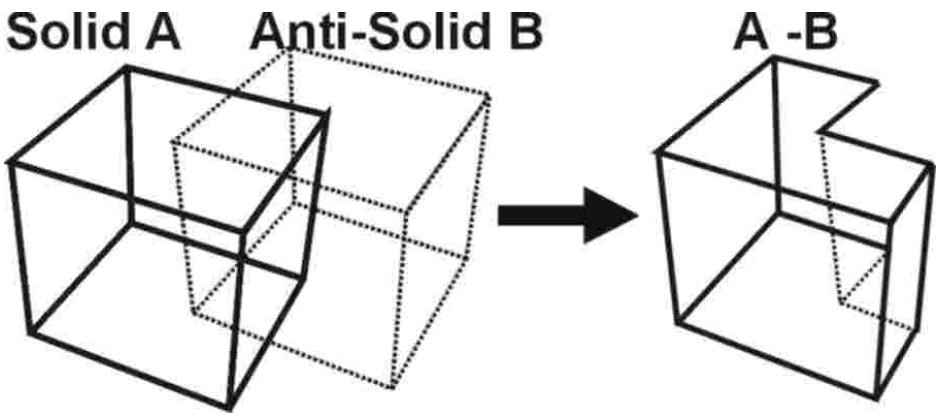

Figure 6.3 Example of Anti-Solid algorithm (ASA) technique

[36] The anti-solid algorithm is derived from the concept of antimatter in physics. In particle physics, antimatter is matter that is composed of the antiparticles of those that constitute normal matter. If a particle and its antiparticle come into contact with each other, the two annihilate (Roy, 2005a). Similarly when solid and anti-solid objects interact they annihilate to give a cut out surface, for example as a residue.

In the operation like cutting hole, subtraction, intersection and union, there are two kinds of object in the process, one is acting object called anti-solid, and another is target object called solid. Target object information is inherited from previous operation and it is the real result existing in the memory. In contrast, the acting object sometimes does not have the full data information. For a cutting hole, all that is needed is the 2D shape of the hole and the length and direction of the hole. What ASA does is that it fulfils the acting object data information and shifts the position between target object and acting object to obtain the final result. The solution for Anti-Solid algorithm depends on the detection of the relationship between faces of two objects. Figure 6.4 gives the flow chart for the procedures in the Anti-Solid algorithm (also see Appendix III for the implementation of ASA).

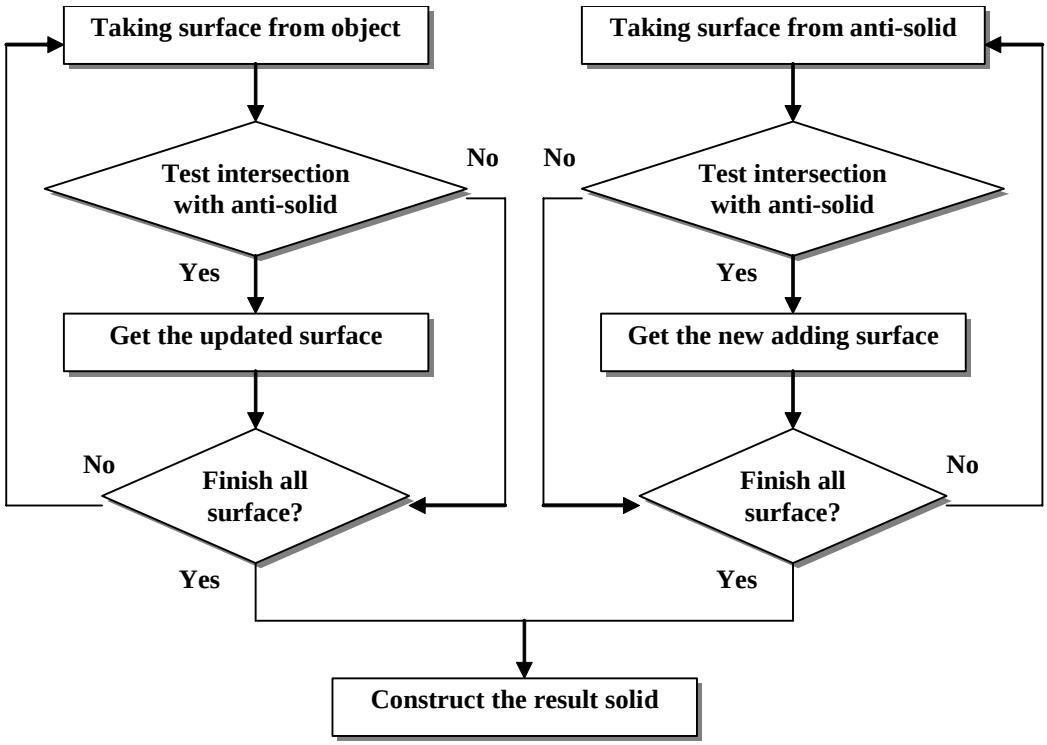

Figure 6.4 The flow chart of Anti-Solid algorithm

6.3 Building Meshed Atlas Visualization Toolkit on Java Platform

Meshed Atlas Visualization Toolkit (MAVT) has been developed based on JAVA™ and its 3D API JAVA3D™. Java3D has a rich set of APIs, which provides powerful and flexible interactive functions useful for building educational and simulation systems. In addition, the other advantages of using Java are multitudinous such as its object oriented mechanism, platform independency, Interactivity of Module Behavior etc. VRML, OpenInventer, etc were also other contestants that can be used for the visualization purposes. For e.g, VRML could be one of the prime candidates as it is recognized as the first international standard for the description of 3D scene data (Jang, 2000). VRML is a pure modeling language which leaves the visualization functions to the VRML browsers. It is easier to be used by model designers in certain sense. However, the disadvantage of VRML is, it is not flexible enough in terms of defining new model paradigms. Another shortcoming of VRML as mentioned before, is its inability to store anatomic information. In addition, it has less control on its rendering effects and it is not very convenient in describing advanced interactions. Java3D and OpenInventer are programming library packages for building visualization applications. Solid software design and programming background are required to use these packages. They are more flexible in building specific interaction functions. They also provide more prosperous rendering functions.

In the case of constructing MAVT, OpenGL, Direct3D, XML, and Java3D has been used to build static and dynamic properties including highlights, mapping textures, lighting, shading, motion constraints, logical judging and animation effects, etc. However, it is worth to mention that professional knowledge on visualization is always required to make use of the advanced features of Java3D to build models and

interactions. Some comprehensive and abstract objects need to be design and developed in order to present the multi-modal anatomy model. Data structure for building foundation of virtual anatomy models for biomedical simulation and education has been designed as an enhancement of the scene graph, which gives a more abstraction and simplification in general biomedical information models. The data structure is an enhancement of the scene graph concept. It is an abstraction of general anatomical models.

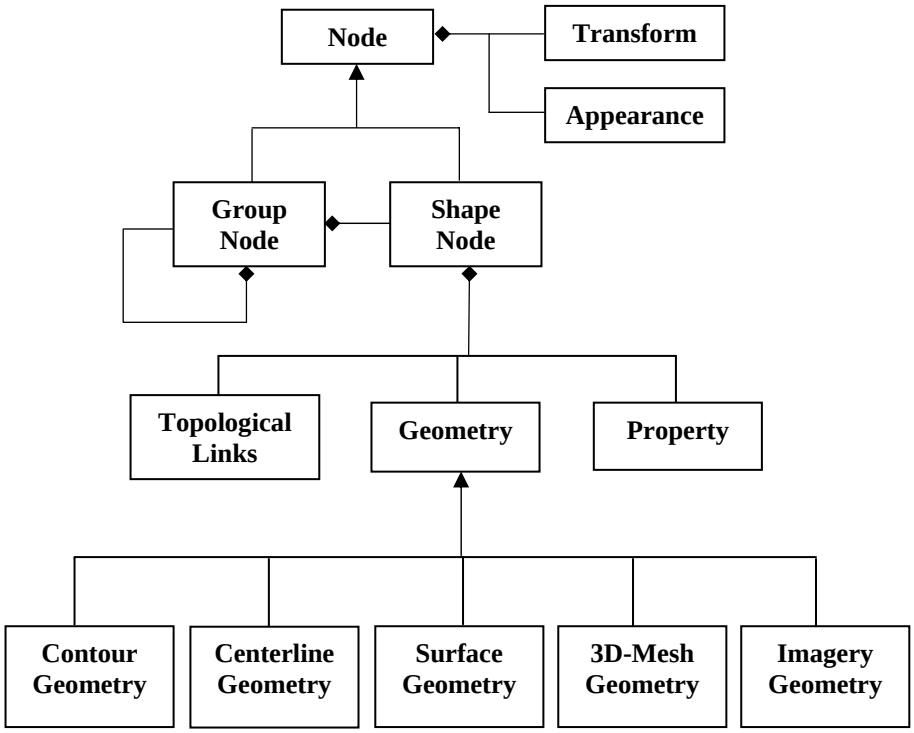

Figure 6.5 The UML model of the foundation data structure designed for virtual anatomy models

The foundation class is the basic class that acts as the interface between MAVT and the Java and Java 3D API. The most important foundation class is *SimulatorApp* that extends *App* class and contains *SimulatorUniverse* inside. Since the picture rendered with Java3D are called *scenes*, MAVT core framework is based on a scene-graph programming model. The *SimulatorUniverse* can be broken into following

components: geometry, GUI, behavior, mathematics, transform, model and appearance.

A comprehensive data structure significantly simplify scene models used for medical education and simulation purposes, and hence also simplify and enhanced the operations for construction of virtual anatomic models. At the center stage of MAVT framework is the SceneGraph object, which is encapsulated inside *Simulator*. Each section can be divided into several subsections. For example, Geometry is further subdivided into contour geometry, surface geometry, mesh geometry etc. Mesh geometry includes an important public class called MeshMaker that extends basic Object class and responsible for creation of meshed model.

Figure 6.5 shows the foundation data structure of the multi-modal anatomy model in UML (Unified Modeling Language) diagram. The group node is similar to a Java3D scene graph transform group node, except it always attached a switch group, which allows the visibility of sub-models being manipulated easily. The geometry nodes are composted by the geometry node in Java3D with some functions needed by more complex modal data.

6.4 Collaboration in Virtual Design Studio

Development of an Atlas Visualization Toolkit in a virtual design studio (VDS) facilitates successful collaboration. Computer supported collaborative work is a field of research that is concerned with understanding the way people work in groups and the enabling technologies of computer hardware, software and networks. MAVT aims to develop a collaborative virtual environment to overcome geographical constraints,

shorten product development time and cost through the Internet. The design activities have been studied and Java™ RMI and Java™ Media Framework has been implemented in the virtual design studio (see Appendix II) to enable effective and efficient collaborative design. As mentioned before, the brain is very complex in structures; it might be a good idea to distribute the entire design work to various users depending upon their domain knowledge. It is possible that some structures of the brain are designed in a computer residing Japan, where as some other parts are developed in Singapore. Finally they all are combined in a user's computer residing USA. Such aspect of collaboration is becoming more practical day after day. The main purpose is to address existing group design processes and the methods to utilize computer technologies to distribute them. Thus a design environment must be established to make full use of all the related domain expertise, technologies and resources available in the world to achieve the common goal. The roles of MAVT in the VDS and the way it facilitates to interact with other parties participating in a particular design activity needs to be described.

In this section we will present how MAVT can implement *Synchronous* and *Asynchronous* collaborative design and virtual environment over the Internet according to the various design perspectives. *Synchronous* designing occurs when the computer and the designed objects are used as interactive tools by more than one designer. At the lowest end of the complexity spectrum is the electronic white-board where the designers draw on a common electronic document. At a higher level of complexity, designers could be working on a 3D model simultaneously in real-time. This becomes real time multi-user designing. *Asynchronous* designing occurs when the computer is used by a group of designers that do not see each other's changes instantaneously and

are not constrained by other's actions. If a design starts from a common state and proceeds asynchronously, then multiple versions are produced. When all the versions are brought together, then discrete actions (i.e. changes) are serialized and made into a unified model. This is serialized or multi-version modeling.

In order to enable *Synchronous* and *Asynchronous* collaborative design in VDS, MAVT uses a Uni-Server to meet the requirements of design activities. By Uni-server it means that no matter the designer's choice for design, he or she has to connect to the same server. This is basically an advancement of previous work (Roy 2000, Roy and Tay, 2003) where we were able to transmit 2D and 3D CAD data over the internet to facilitate collaborative design implementing Java™ Remote Method Invocation (RMI) and Java™ Media Framework (JMF). Such distributed application can be extended to MAVT too to facilitate effective design and collaboration between geographically dispersed users. Distributed applications developed for this module are mainly focused on collaborative design in virtual environment. In order to overcome geographical and time constraints, one fast and easy solution is the utilization of the Internet. Right from the concept analysis stage, integrated networking capability was considered as a major feature of such application. An integrated networking capability also strongly supports the cause of platform independence because it does not rely on the operating system network communication module (also see Appendix II).

The various concepts of groupware that are reviewed and analyzed meticulously and later attempted to implement for developing VDS for synchronous collaboration through a mapping window (same time–different place collaboration) and for asynchronous collaboration by saving an image files in the local system (for same

place–different time collaboration) and then transmitting the image to remote users using electronic mailing system (different time–different place collaboration). The success in this issue opens a new arena in future collaborative groupware research.

Figure 6.6 illustrates the basic structure of a Uni-Server of VDS built for basic collaboration purpose. The Uni-Server holds the MAVT application and it has a storage system and a fixed IP address for clients to access. One thread of application is representative of one project. Multi-threads are allowed for the parallel CAD environment. Parallel projects can be performed concurrently. Designers can connect to server as clients and a particular designer can access different data storages depending on the project group that he is logged into. Once the designer is logged onto the server, the current server, Simulation-Universe, will display on the client's machine the relevant design components.

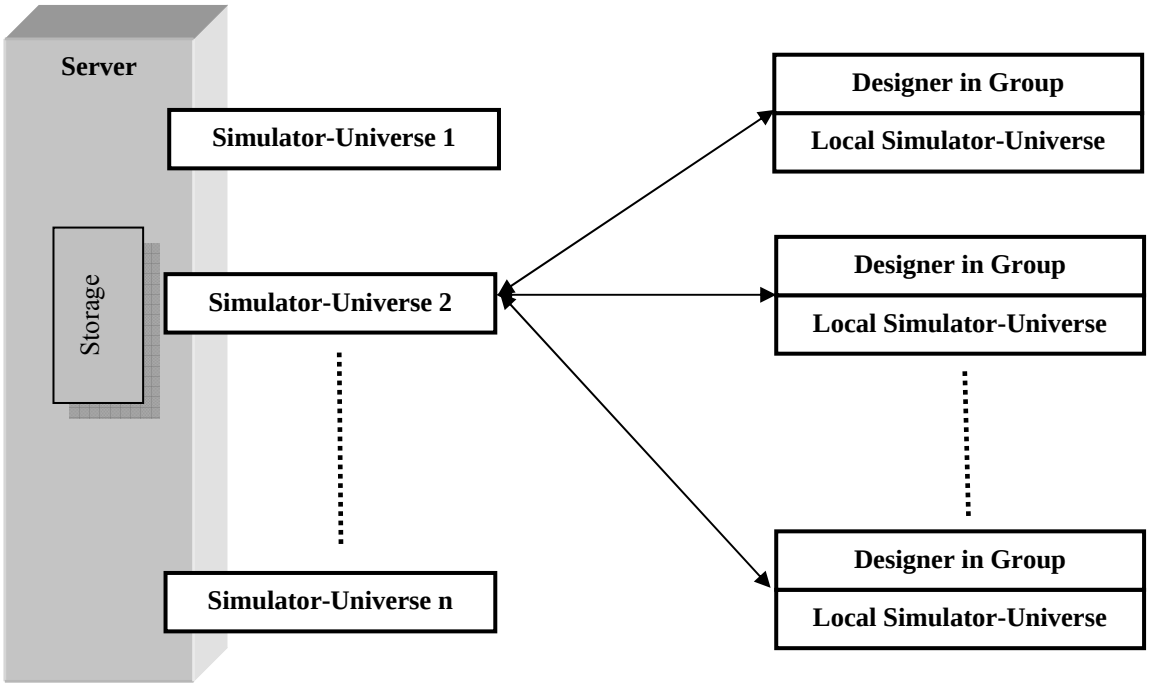

Figure 6.6 The structure of VDS

We choose XML to present virtual anatomic model definition because of its exceedingly extensibility. We created an XML schema that complies with the data definition as shown in Figure 6.5. The XML schema is designed to handle more complex anatomy models, for example, centerline tubular model data, etc. that cannot be easily handled by other visualization modeling languages. The implementation of the system uses the MVC (model-view-controller) paradigm to increase the reusability of the code developed. The appropriate design patterns (Liseikin, 1999) are used as much as possible wherever they are applicable. Java's rich network classes also enable remote file transfer, remote drag and drop and other real time interactions within MAVT so that distant participants can collaborate comfortably with each other. The designer can freely obtain the design components from the Server Simulation-Universe to Local Simulation-Universe to do the modification using the Drag & Drop functionality (Tay and Roy, 2003). As a security measure, VDS also enables the designer to lock the particular design on the server side when he is in the process of modifying it. Upon completion of the modifications (or creations), the designer can then update the design component from the client to the server side. The finished component is then stored on the server awaiting feedback from other designers, the project manager and other involved parties (such as marketing and manufacturing). In short, design creation and modification is carried out on the local client side while storage and display is carried out on the server side.

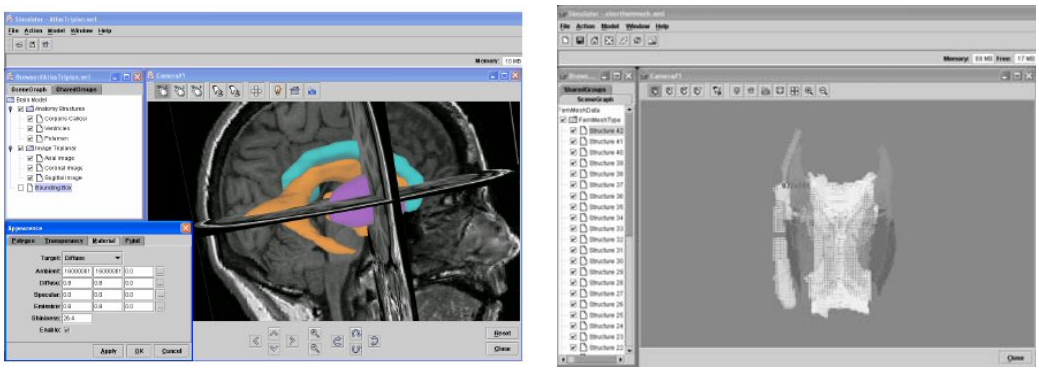

Figure 6.7 The GUI of MAVT

A centralized system keeps a single copy of the shared application on a central server and the GUI part is shared among several clients over the network. The application used direct manipulation GUI which has been proved to be suitable for education and simulation (Schneiderman, 1998). The GUI components are designed to achieve the direct manipulation functionalities including direct manipulation of visual effects (such as lighting, model appearance etc.), functions for association of topology and anatomy information, manipulation of anatomy structure with multi-modal data models, simulation of geometric modeling and physical modeling etc. The GUI of virtual anatomy model in MAVT has been shown in Figure 6.7.

When the large volume of information is to be shared, a centralized architecture may give very efficient result. On the other hand, a replicated architecture can also be used based on executing a copy of the application for each user. MAVT uses this replicated structure because, if a large amount of user transaction is necessary, which is the MAVT case, a replicated architecture will be more beneficial. Similarly, there are several kinds of protocols to resolve interpersonal conflicts (Roy, 2000). MAVT team used a protocol called controller/viewer protocol, which is actually a combination of both the master–slave protocol and token-based protocol (Roy, 2000; Tay and Roy,

2003). The controller/viewer protocol enables the multiple users to work in a parallel way and thus speed up the entire design process. The network connection was maintained through TCP/IP. TCP/IP is chosen as reliability is critical to the successful transfer of information in such applications.

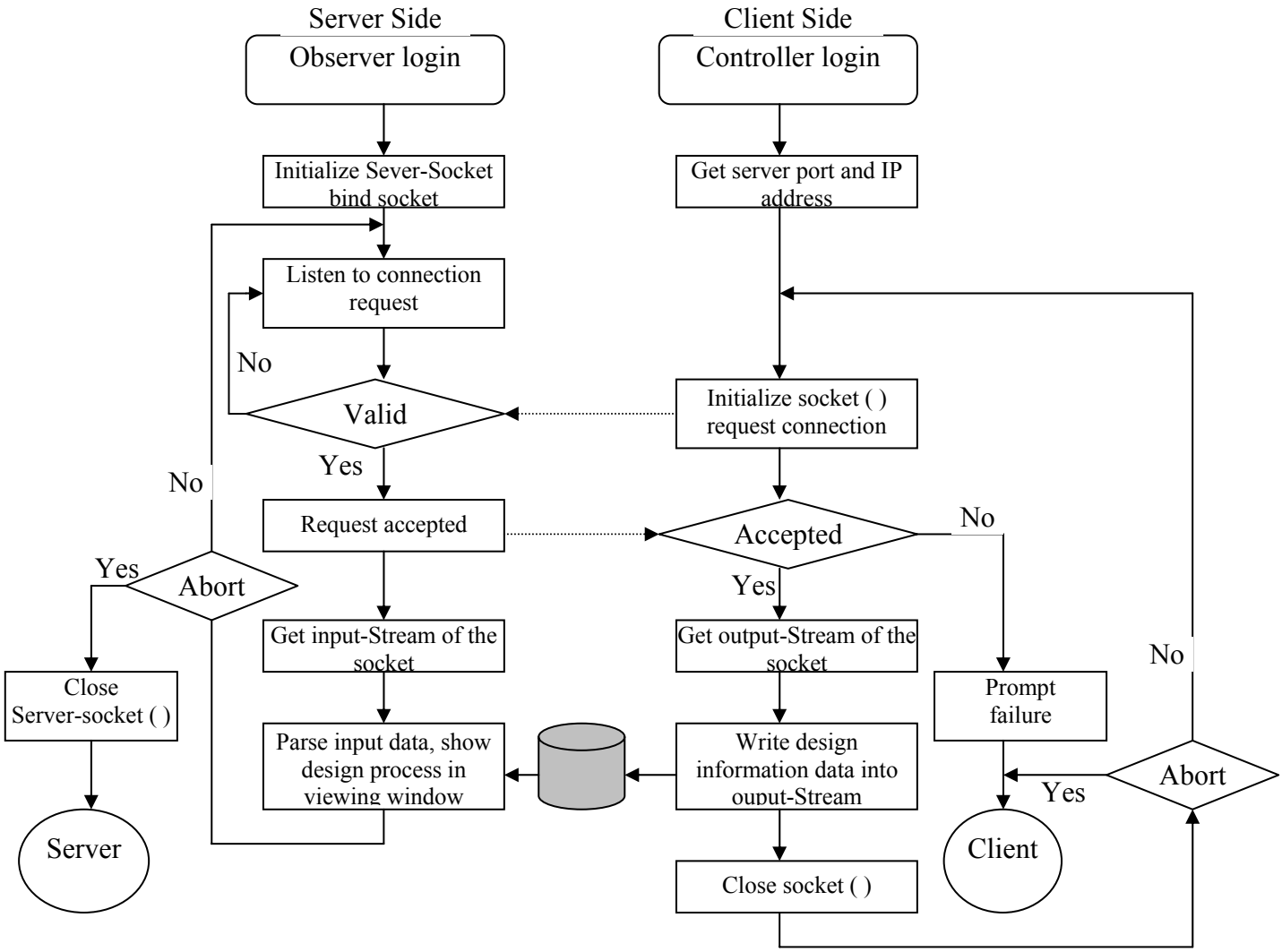

Figure 6.8 The flowchart of communication between server and client in VDS

It provides a point-to point channel to connect computers with one another over the Internet. In addition, it guarantees that data sent from one end of the connection actually gets to the other end failing which, error messages will be reported. As a result, we adopt a socket to write client-server program that is embedded into MATV

for Uni-Universe collaboration model. The controller is at the client side while the observer is at the server side of a client/server pair. To establish a connection between a client program and a server using TCP, each program needs to bind a socket to its end of the connection. Two classes (Socket and Server-Socket) provided in the java.net package are used to implement the client and server side of the connection respectively.

When a collaborative design project uses VDS as the design tool, the first validated login design partner will create the Virtual Universe. This Virtual Universe remains active in the server until it is closed. Using a user ID and password as registration data, any valid designer is able to login to that Virtual Universe to collaborate with other designers. After logging into the system, an observer may open a Server-Socket (on the server side) that is bound to a specific port number if he wishes to help another person in design. The server just waits, "listening" to the socket for a client to make a connection request. On the client-side, the client controller has to know the hostname of the server and the port number to which the server is connected. To make a connection request, the client has to rendezvous with the server on the server's machine and port. For a successful connection, the server has to first accept the connection. Upon acceptance, a new socket bound to a different port is enabled on the server side. This new socket (consequently a different port number) is needed so that the server can continue to listen to the original socket while tending to the needs of the connected client. On the client side, if the connection is accepted, a socket is successfully created and the client can use the socket to communicate with the server. Note that the socket on the client side is not bound to the port number used to rendezvous with the server. Rather, the client is assigned a port number local to the machine on which the client is

running. The client and server can now communicate by writing to or reading from their sockets. Figure 6.8 shows the flowchart describing the communication between server and client in VDS.

6.5 Computational Results

We have developed a framework to build a few multi-modal virtual anatomy models, suitable for their usage in medical education and simulation. Figure 6.9 shows a multi-modal virtual brain anatomy model. Figure 6.9(a) and (b) show the brain model consisting of triplanar images and surface models organized together and grouped by their modalities. The grouping operations can be done interactively using the browser window shown in Figure 6.7.

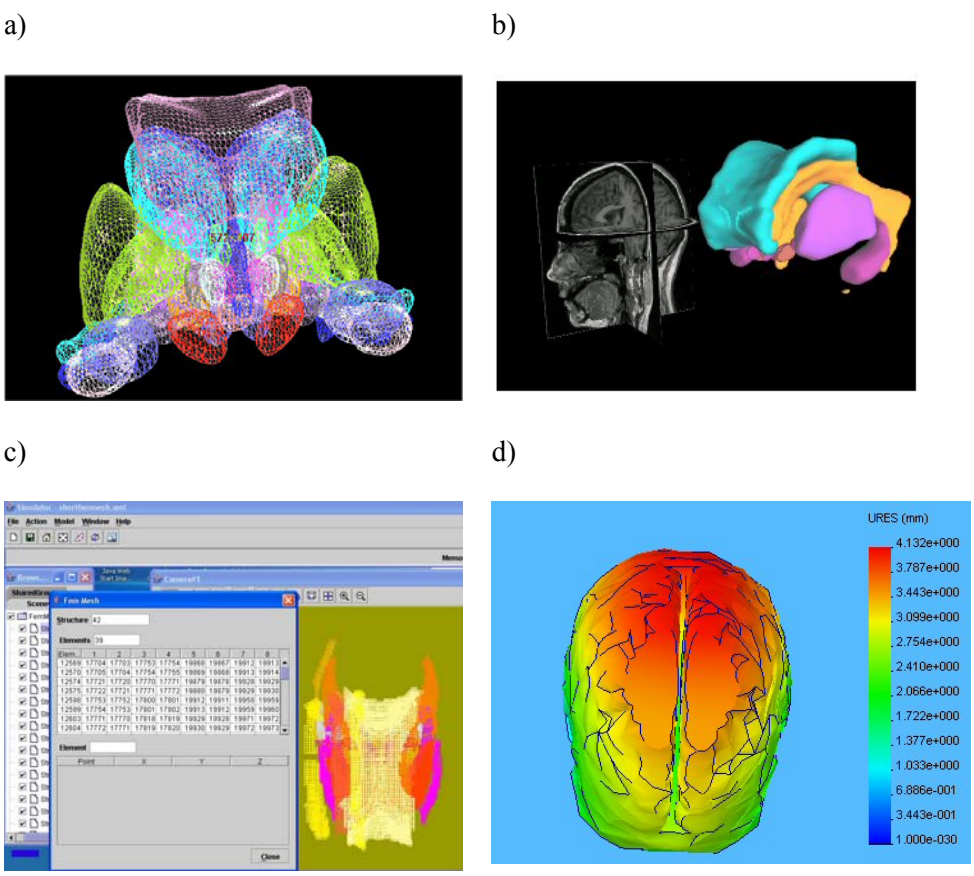

Figure 6.9 Visualization of 3D brain model in java-based MAVT platform

Figure 6.9(a) and (b) show the brain model consisting of triplanar images and surface models organized together and grouped by their modalities. The grouping operations can be done interactively using the browser window shown in Figure 6.7. Users can group anatomy models by systematic anatomy or regional anatomy or modality on the fly whenever they like. This will be very useful in medical education for the students to gain anatomy knowledge. Figure 6.9(c) shows the FEM meshed model in MAVT. Figure 6.9(d) shows a FEM analysis of a brain using the meshed atlas data. Medical students, radiologists, bioengineers and surgeons will be able to manipulate such models for learning the spatial position of the anatomy structures, and for simulating and planning complex surgeries. The direct manipulation GUI allows users to manipulate and control the virtual model easily and efficiently. By manipulating individual objects or individual modality data in these models or by manipulating the combination of these data models, this environment can be used as prototypes of various visualization-based or virtual reality-based medical applications. These models greatly reduce development complexity enabling the user to comfortably collaborate with distant participants.

6.6 Summary of the Chapter

We have proposed a framework for developing a meshed atlas visualization toolkit, MAVT that can be used for medical study, simulation purposes and other virtual reality applications. The concept is published in Roy et al (2006b). A multi-purpose GUI has been designed and developed which can be used for constructing virtual anatomy models that facilitates successful collaboration between geographically dispersed users. The concept of *collaborative CAD system* has been promulgated in one journal (Tay and Roy, 2003) whereas concepts and result of

collaborative *mesh generator* through a *virtual design studio* has been submitted for another publication (Roy et al, 2006c).

Chapter 7

FUTURE RECOMMENDATION AND CONCLUSION

In this thesis a Physics-based Atlas (PBA) has been proposed that contains fully meshed 43 major anatomical structures, cortical regions and brain connections; and possesses the highest anatomical parcellation. This is the novelty of the work over other existing models. The PBA is built upon axial plates of an electronic brain atlas named *Cerefy* that was able to provide the detailed anatomical information of the brain. For the construction of the PBA a well established physical theory of continuum mechanics is applied and for the discretization and to obtain the solution of problems, *finite element method* has been used. The PBA provides a useful mechanism for the modeling of tissue properties, characterizing and visualizing the changes and deformation of the structures and organs. This newly developed meshed atlas has also indicated the possibility to analyze the biomechanical deformations of the brain including its subcortical structures and showed potential to analyze some structural diseases such as tumor growth etc.

7.1 Future Work

The success of newly developed PBA is highly dependent on the favorable outcome of the future research on the proper investigation of material properties of individual structures and accurate boundary conditions of the entire system. Since the material property always plays an important role in such physics-based modeling, a comprehensive literature study was done on this subject. Besides this, we conducted our own indentation experiment in Biomechanics Lab of National University of

Singapore on porcine brains to determine the important material parameters and characteristics and to learn tissue behavior under uniaxial compression. Yet the material properties of all the structures are grossly unknown and still fall in the active area of research; nevertheless the developed physics-based atlas as a first step in this direction that addressed the necessity of a multistructured biomechanical brain model. As soon as various gaps and uncertainties related to material properties get resolved in course of time the PBA will mark its importance for research in brain biomechanics and bioimaging; and for diagnosis, surgical planning and surgical guidance in future.

Besides material properties another significant challenge, which needs to be fully addressed in future for the accurate solution from PBA, is how boundary conditions can most effectively be applied to these biomechanical models. By adopting boundary conditions more precisely (based on current knowledge), we can at least reduce our dependency on a complete knowledge of the mechanical properties of an organ, which, based on current technical limitation will be almost impossible to attain. This field is also still in its infancy and major challenges remain. In author's opinion, the research on boundary conditions is as important as research on material properties and construction of precise geometrical model of the brain.

As an illustration of the usefulness of the PBA, two specific biomechanical situations (specifying constitutive laws and boundary conditions) are simulated in the thesis. One is for simulating a neurosurgical condition, i.e. brain deformation due to the forces acting on the top of the brain by surgical tools. Another is simulating a macroscopic, primary brain tumor growth (tumor is meshed from real pathological data) incorporating the biological and biochemical factors that can affect the meshed model.

Besides these, the newly developed physics-based atlas can make a valuable impact in future research on bioimaging, biomechanics, characterizing material parameters and properties, registration and other atlas based applications. As a framework, one of the potential future applications of PBA i.e image-guided surgery is described below (Figure 7.1).

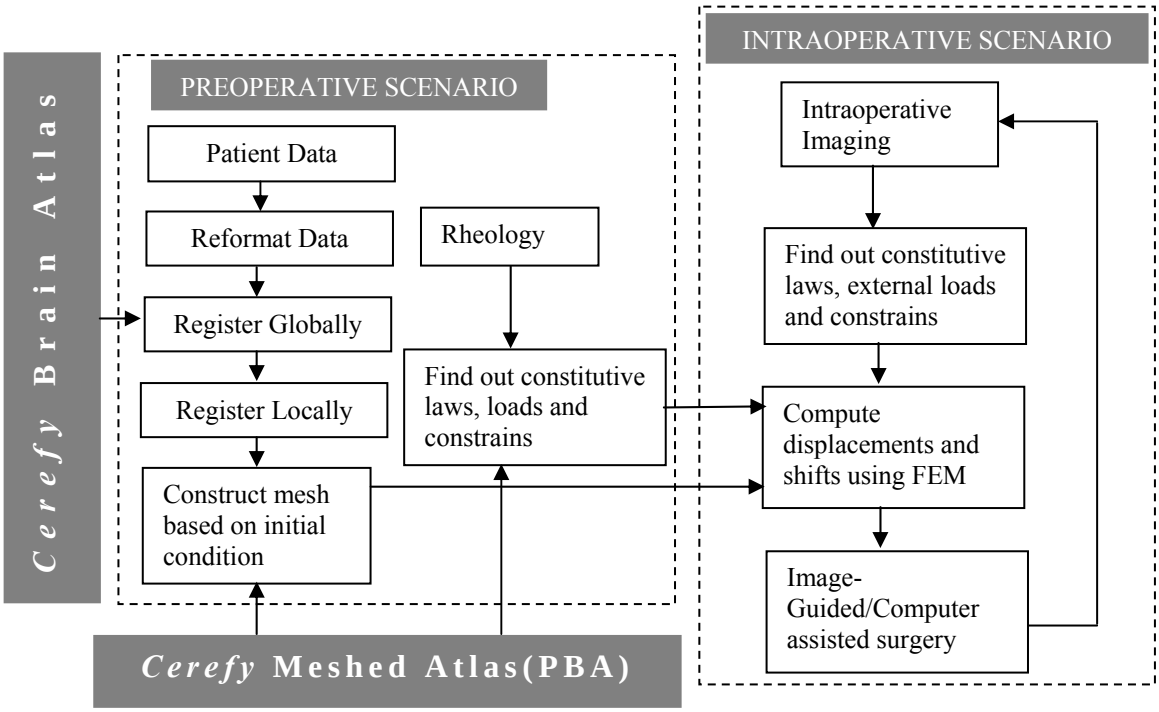

Figure 7.1 The framework to use the PBA for image guided surgery

For image-guided surgery, one has to consider nonrigid registration as when using a rigid-body transformation gives unacceptable result for many surgical applications. One possible solution to this problem is to use biomechanical models (like PBA has provided) as a means of applying additional information to constrain a non-rigid registration. This technique can be designed to allow the warping of one anatomical structure onto another and that also can be a special interest for making PBA involved in future direction of research. As the challenges of soft tissue modeling for image-

guided surgery are solved, we can expect to see procedures becoming less invasive, the information from more modalities being incorporated into the model and a much wider range of applications developed.

Despite our efforts, the developed Physics-based Atlas using the *Cerefy* database has some limitation. Firstly, an accurate solution of the model needs the accurate biomechanical material properties of tissues of each structure to be known, which still falls under active area of research. For physical investigation of tissue properties, we have developed a system to test on an adult pig brain in Bioengineering Lab of National University of Singapore (NUS) assuming that material properties of pig brain is very close to that of human. However, how much realistic the assumption is could always be under dispute. Our FEM analysis shows human brain is about 32-35% stiffer compared to porcine which agrees with the current result. The atlas does not have bone, vessels, cerebellum and the complete brainstem; so an accurate and exact state has not been reflected in our model. Also, more research is needed to have the adequate knowledge about the interface between brain and skull to formulate the proper boundary conditions for the development of correct mathematical modeling. In fact in author's opinion, meticulous research on determining correct boundary condition of brain is as important as investigating tissue properties. As for other future work, various anatomical and physiological constraints can be included in meshed atlas model and combine together. Future directions of research with PBA can be enlisted as:

- Development of complete and as-precise-as-possible biomechanical model of human head (brain with skull) and neck that reflects maximal physical realism.

- Modeling the collision and friction between skull and brain.
- Inclusion of anisotropy and fibers orientation of brain tissues in the mechanical comportment of our finite element model. Additionally as a second step an integration of anisotropic material behavior arising from arteries, veins or variations of cell densities.

In addition to include major anatomical structures and constraints, we wish to introduce the following physiological constraints in the model:

- Blood pressure.
- CSF pressure
- Osmotic pressure.
- Cerebral perfusion pressure etc.

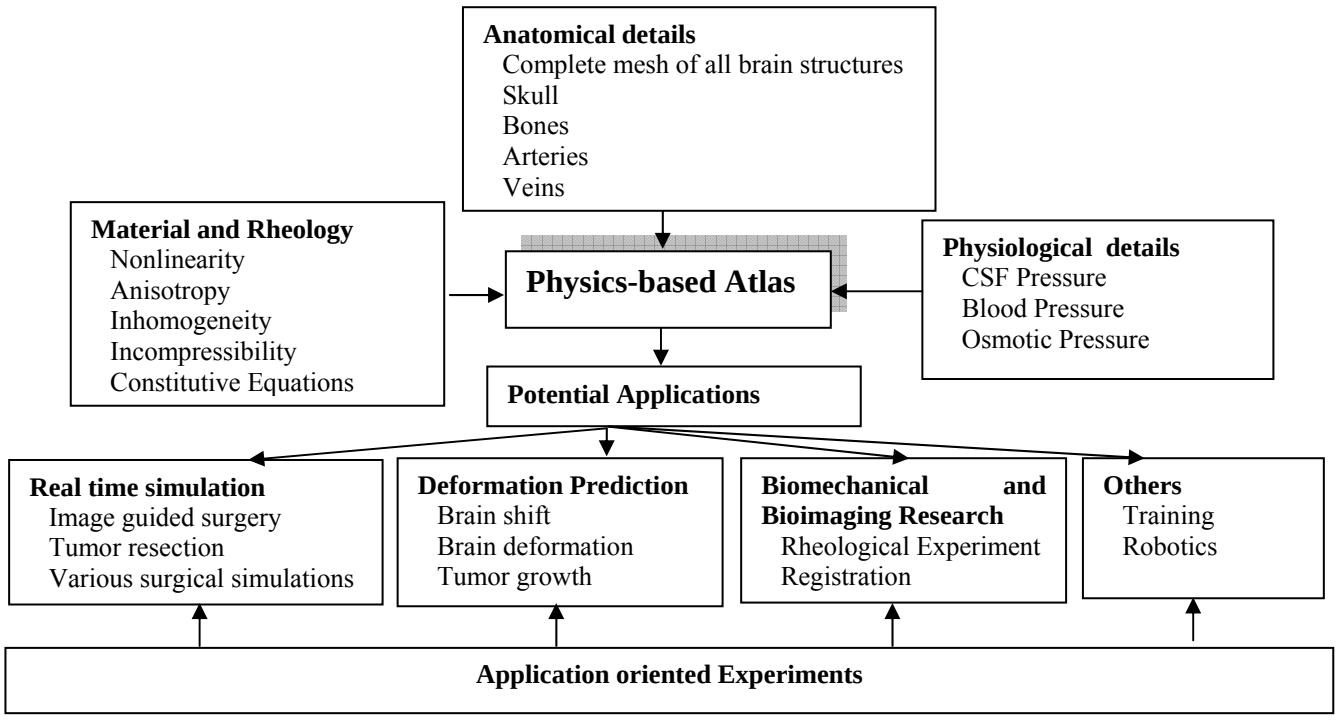

Figure 7.2 Physics-based atlas and its potential applications

Such a full-featured biomechanical model should allow us to explore new research tracks, including the developed deformation model. However, such inclusion and extension of above features will require the derivation of new *constitutive equations* which always remains as a challenging and complex task. Construction of PBA is the first attempt of constructing a full-featured 3D meshed atlas, and the methodical approach and result presented should be useful in the future direction of research and development in biomechanics. The complete physics-based atlas with its potential applications can be summarized in Figure 7.2.

7.2 Conclusion

The human brain is so complex that sometimes its complexities are compared with the model of the whole universe. The human brain consists of about 100 billion neurons and 100 trillion synapses with so many complicated structures just as our universe contains billions of stars, planets and galaxies and complex formation of the nebula, solar system etc. To demystify the various complexities, the brain has been widely studied for centuries by various groups such as anatomists, physiologists, biochemists, geneticists, surgeons, neurologists, psychologists, human brain mappers, bioengineers, biologists, philosophers and many others. Nevertheless, no physics-based atlas is constructed yet. For the first time a finite element biomechanical modeling approach has been proposed to construct a complete 3D physics-based atlas (PBA) that contains fully meshed 43 major anatomical structures and brain connections. The original contribution and the novelty of the work over the other existing model has been described throughout the dissertation. The proposed model has shown the ability to simulate the deformation for the whole brain as well as individual sub-cortical structures during neurosurgical procedures (the strain rate between 0.001s-1 – 1.0s-1).

The limiting stress relaxation for infinitesimally small loading has also been obtained (the shear modulus reaching 194.62 Pa) exhibiting similarity with a hydrocephalic condition. In addition, a macroscopic, primary brain tumor growth is simulated incorporating the biological and biochemical factors that affect the meshed model. The geometrical and experimental validations have also been incorporated.

This dissertation also illustrates a framework of useful an automated mesh generator, MAVT that can successfully construct and visualize the virtual anatomical meshed model. One of the important features MAVT provides is 'collaboration opportunity' among the geographically dispersed users. To enable such *Synchronous* & *Asynchronous* collaborative design over a network, VDS module has been incorporated as an important feature. This makes MAVT a distributed application focusing on collaborative design in a virtual environment. The implementation of the system uses the MVC paradigm to increase the reusability of the code developed. The appropriate design patterns are used as much as possible wherever they are applicable. Its rich network classes also enable remote file transfer, remote drag and drop and other real time interactions within MAVT so that distant participants can collaborate comfortably with each other. Till date MAVT is the first mesh generator with distributed and collaborative features, thus it is expected to play an important role in developing an effective collaboration design architecture based on the available IT infrastructures. The work also ensures effective team organization, coordination and negotiation that are the keys to the success of a collaboration process and we hope that this work will extend the scope of brain atlases for research and clinical applications as well. This atlas has a potential to predict brain deformation in surgical loading and in future may be well-incorporated into image-guided or computer-assisted surgery. Its

other potential benefits include increased accuracy of modeling, visualization and surgical simulation, intraoperative computations, patient specific operation planning or prognosis of various structural diseases. The newly developed PBA can also be incorporated in various education or training programs.

REFERENCES

ABAQUS/Standard, Version 6.4, 2001, Hibbit, Karlsson & Sorenson, Inc.

Adams V and Askenazi A, 1998, Building Better Products with Finite Element Analysis, High Mountain Press.

Akkas, N, 1979, Continuum modeling of head injury, Progress in Biomechanics ed: N.Akkas, NATO Advanced Study Institutes Series E: Applied Science No.32, Sijthoff and Noordhoff, The Netherlands, 297-331.

Al-Bsharat AS, Hardy WN, Yang KH., Khalil TB, Tashman S, and King AI, 1999. Brain/skull relative displacement magnitude due to blunt head impacts: new experimental data and model. SAE Technical Paper 99SC22. In Fortythird Stapp Car Crash Conference Proceedings (P-350), 321-332. Warrendale, PA: Society of Automotive Engineers, Inc.

ANSYS Release 9.0 Documentation, 2004, ANSYS, Inc.

Arbogast KB, Prange MT, Meaney, DF, and Margulies, S.S. 1997. Properties of Cerebral Gray and White Matter Undergoing Large Deformation, in: Prevention Through Biomechanics, Symposium Proceedings, Wayne State University, 33-39.

Azar FS, Metaxas DN, Schnall MD, 2001, A deformable finite element model of the breast for predicting mechanical deformations under external perturbations. *Journal of Academic Radiology*, Vol. 8, 965–75.

Baggaley A. (editor), 2001, Human Body, Dorling Kindersley (UK), 1st US edition, New York.

Bajcsy R., Kovacic, S., 1989, Multi-resolution Elastic Matching, *Computer Vision, Graphics, and Image Processing,* Vol. 46, 1-21.

Barr AH, 1984, Global and local deformations of solid primitives. In Proceedings of SIGGRAPH'84

Bartels R, Beatty J, and Barsk B, 1987, An Introduction to Splines for use in Computer Graphics and Geometric Modeling, Morgan Kaufmann, Los Altos

Basser PJ, Interstitial pressure, volume, and flow during infusion into brain tissue., 1992, Microvascular Research., Vol 44, Issue 2, 143-65.

Bathe, K.-J., 1996. Finite Element Procedures in Engineering Analysis. Prentice-Hall, Inc, Englewood Cliffs, NJ.

Begun P. I. and Shukeilo. J. A., 2000, *Biomechanics (in russian).* Polytechnika. ISBN 5732503095, St.Petersburg.

Bilston L E., Liu Z, and Phan-Thien N, 1997, Linear viscoelastic properties of bovine brain tissue in shear, *Journal of Biorheology*, Vol. 34, Issue 6, 377-385

Bilston, L.E., 2002. The effect of perfusion on soft tissue mechanical properties: a computational model. *Computer Methods in Biomechanics and Biomedical Engineering*, Vol 5, 283–290.

Blacker, Ted D and Myers RJ, 1993, Seams and Wedges in Plastering: A 3D Hexahedral Mesh Generation Algorithm, *Engineering with Computers*, Vol. 2, 83-93

Bookstein FL, 1989, Principal warps: Thin-plate splines and the decomposition of deformations. IEEE Transactions on Pattern Analysis and Machine Intelligence, Vol. 11, Issue 6, :567-585

Brands DWA., Peters GWM. and Bovendeerd PHM., 2004, Design and numerical implementation of a 3-D nonlinear viscoelastic constitutive model for brain tissue during impact, *Journal of Biomechanics*, Vol 37, Issue 1, 127-134.

Brands D, Bovendeerd P, Peters G, Wisman J., Paas M., and Bree Jv., 1999, Comparison of the Dynamic Behavior of Brain Tissue and Two Model Materials, Proceedings of 43rd Stapp Car Crash Conference.

Brebbia CA, Telles JCF, Wrobel LC, 1984, Boundary element techniques, Theory and applications in engineering, Berlin: Springer.

Brezinski C, Zaglia MR, 1991, Extrapolation Methods. Theory and Practice, North-Holland.

Broit C, 1981. Optimal Registration of Deformed Images. PhD dissertation, Computer and Information Science Department, University of Pennsylvania, PA,

Bro-Nielsen, M., 1997. Fast finite elements for surgery simulation. In: Proc. Medicine Meets Virtual Reality V (MMVR).

Bro-Nielsen, M., Gramkow, C., 1996. Fast Fluid Registration of Medical Images. In: Visualization in Biomedical Computing (VBC).

Bucholz RD, Yeh DD, Trobaugh J, McDurmont LL, Sturm C, Baumann C., Henderson J. M, Levy A, Kessman P, 1997, The correction of stereotactic inaccuracy caused by brain shift using an intraoperative ultrasound device, Computer vision, virtual reality and Robotics in Medicine and Medical robotics and Computer-Assisted Surgery (CVRMedMRCAS'97), Vol. 1205 (Springer-Verlag, France), 459–466.

Bylski DI, Kriewall TJ, Akkas N, and Melvin JW, 1986, Mechanical behavior of fetal dura mater under large deformation biaxial tension, *Journal of Biomechanics*, Vol. 19, 19-26

Canann SA., Tristano JR. and Staten ML., 1998, An approach to combined Laplacian and optimization-based smoothing for triangular, quadrilateral and quad-dominant meshes, Proc. 7th International Meshing Roundtable, 479-494.

Carter TJ, Sermesant M, Cash DM, Barratt DC, Tanner C, Hawkes DJ, 2005, Application of soft tissue modeling to image-guided surgery, *Medical Engineering & Physics*, Vol. 27, 893–909.

Castellano-Smith AD, Hartkens T, Schnabel JA, Hose R, Liu HY, Hall W, et al., 2002. A registration based mesh construction technique for finite element models of brains.

In: Medical Imaging 2002: Image Processing, Vol. 1–3, vol. 4684, Proceedings of the Society of Photo-Optical Instrumentation Engineers (SP1E); 538–49.

Chang Y and Rockwood AP, 1994, A generalized de casteljau approach to 3D free-form deformation. In Proceedings of SIGGRAPH'94 Conference.

Christensen, G., Aug. 1994. Deformable shape models for anatomy. Ph.D. dissertation, Dept. Elect. Eng., Sever Institute of Technology, Washington University, St. Louis, MO.

Chu CH, Cheng CY, Wu CW, 2006, Applications of the Web-based collaborative visualization in distributed product development, *Computers in Industry*, Vol. 57, 272–282.

Clatz O, Delingette H, Bardinet E, Dormont D, Ayache N. 2003, Patient specific biomechanical model of the brain: application to Parkinson's disease procedure, in: Proceedings of the Surgery Simulation and Soft Tissue Modeling, vol. 2673, Lecture notes in computer science, 321–31.

Coats B, and Margulies SS, 2005, Material properties of porcine parietal cortex, In Press, Corrected Proof, Available online (http://www.sciencedirect.com).

Cook WA and Oakes WR., 1982 Mapping Methods for Generating Three-Dimensional Meshes, *Computers in Mechanical Engineering*, 67-72

Coquillart S, 1990, Extended free-form deformation: A sculpturing tool for 3D geometric modeling. In Proceedings of SIGGRAPH'90 Conference.

CosmosWorks (Introducing CosmosWorks: Design Analysis made easy), Documentation, 2004: CWMISENG0703, COSMOS™

Cover SA., Ezquerra, NF, O'Brien, JF, Rowe, R., Gadacz, T., Palm, E., 1993. Interactively deformable models for surgery simulation. IEEE Computer Graphics and Applications 13 (6), 68–75.

Dalhousie University, Department of Anatomy and Neurobiology, 2004, Meninges and blood supply of the central nervous system. http://www.anatomy.dal.ca/Human%20Neuroanatomy/Labs/Lab1.html

Darvish, Kurosh K, Characterization of Nonlinear Viscoelastic Properties of Brain Tissue Using Forced Vibrations, PhD dissertation, University of Virginia, 2000.

Davatzikos, C., Prince, J., 1995. An active contour model for mapping the cortex. *IEEE Transactions on Medical Imaging*, Vol. 14, Issue 1, 65-80.

DeArmond S. J., Fusco MM, Dewey MM, 1989, Structure of the Human Brain. A Photographics Atlas (3rd ed). Oxford University Press, New York.

Delaunay BN, 1934, Sur la Sphere, Vide. Izvestia Akademia Nauk SSSr, vII Sena, Otdelenie Matematichekkii I Estestvennyka Nauk, 17, 793-800.

Delingette H and Ayache N, 2004, Soft tissue modeling for surgery simulation, In: Ayache N, editor. Computational models for the human body, vol. XII, Handbook of numerical analysis. Amsterdam, The Netherlands: Elsevier BV, 453–545.

Delinguette, H., March 1998. Toward Realistic Soft-tissue Modeling in Medical Simulation. *Proceedings of the IEEE*, Vol. 86, Issue 3, 512-523.

Dev P, Friedman C, Dafoe B, Felciano R, 1992, Testing spatial understanding of anatomy, Proceedings - the Annual Symposium on Computer Applications in Medical Care, 804-5.

Donnelly BR, Medige L. Shear properties of human brain tissue, 1997, Transaction of *ASME Journal of Biomechanical Engineering*,119:423–32.

Duvernoy HM, 1988, The Human Hippocampus: an Atlas of Applied Anatomy. Bergman, Munch.

Estes, M.S., McElhaney, J.H., 1970. Response of brain tissue of compressive loading. *American Society of Mechanical Engineers,* 70-BHF-13, 1-4,

Farshad M, Barbezat M, Flüeler P, Schmidlin F, Graber P and Niederer P., 1999, Material characterization of the pig kidney in relation with the biomechanical analysis of renal trauma, Journal of Biomechanics, Vol. 32, Issue 4, 417-425.

Ferrant M, 2001b, Physics-based Deformable Modeling of Volumes and Surface for Medical Image Registration, Segmentation and Visualization, PhD dissertation, Louvain, Belgium: Universite Catholique de Louvain.

Ferrant, M, Warfield SK, Guttman CRG, Mulkern RV, Jolesz FA., and Kikinis R., 1999, 3D Image Matching Using a Finite Element Based Elastic Deformation Model. In C. Taylor and A. Colchester, editors, MICCAI 99: Second International Conference on Medical Image Computing and Computer-Assisted Intervention; Cambridge, England., pages 202–209.

Ferrant M, Nabavi A., Macq B., Black P., Jolesz F., Kikinis R., Warfield S., 2001a. Serial registration of intraoperative MR images of the brain. Medical Image Analysis, Vol. 6, 337-359

Field, D, 1988, Laplacian smoothing and Delaunay triangulations, *Communications in Numerical Methods in Engineering*, Vol. 4, 709-712.

Freitag L., Ollivier-Gooch C., 1996. A comparison of tetrahedral mesh improvement techniques. In: Proceedings of the Fifth International Meshing Roundtable.

Fung Y, 1993. Biomechanics: Mechanical Properties of Living Tissues. Springer-Verlag, Berlin, Germany.

Galford JE., McElhaney, J.H., 1970. A viscoelastic study of scalp, brain, and dura. *Journal of Biomechanics*, Vol 3, 211-221.

Gardner ED, Gray DJ, & O'rahilly R, Anatomy: A Regional Study of Human Structure, W. B. Saunders Co., London, 1960.

Gee J., Reivich M., Bajcsy R., 1993. Elastically deforming 3D atlas to match anatomical brain images. *Journal of Computer Assisted Tomography* 17 (2), 225-236.

Gefen, A., Margulies S.S., 2004. Are in vivo and in situ brain tissues mechanically similar? *Journal of Biomechanics*, Vol. 37, 1339–1352.

Gibson, S., 1997. 3D Chainmail: a Fast Algorithm for Deforming Volumetric Objects. In: Symposium on Interactive 3D Graphics, ACM SIGGRAPH.

Gillespie, J and Jackson A, 2000, *MRI and CT of the Brain*, Hodder Arnold, UK

Gladilin E, Biomechanical Modeling of Soft Tissue and Facial Expressions for Craniofacial Surgery Planning, PhD dissertation, Free University Berlin, 2003.

Goldsmith, W., 1972, Biomechanics of head injury. in Biomechanics: Its foundation and objectives. Fung, Y.C., Perrone, N., and Anliker, M (eds)., Prentice-Hall, Inc., NJ.

Guillaume A, Osmont D, Gaffie D, Sarron, JC, Quandieu P, 1997, Effects of perfusion on the mechanical behavior of the brain-exposed to hypergravity, *Journal of Biomechanics*, Vol. 30, Issue 4, 383-9

Haber, E., Metaxas, D., Axel, L., October 1998. Motion Analysis of the Right Ventricle from MR images. In: MICCAI 98: First International Conference on Medical Image Computing and Computer-Assisted Intervention; 1998 Vol. 11, Issue 13; Boston, USA. Springer.

Hagemann, A., 2001, A Biomechanical Model of the Human Head with Variable Material Properties for Intraoperative Image Correction. PHD dissertation, Logos Verlag Berlin, ISBN 3-89722-665-0.

Hagemann, A., Rohr, K., Stiehl, H. S., Spetzger, U. and Gilsbach, J. M., 1999. Biomechanical Modeling of the Human Head for Physically Based, Non- Rigid Image Registration. *IEEE Transactions on Medical Imaging*, Vol. 18, 875-884

Hartmann U and Kruggel F, 1999, Transient analysis of the biomechanics of the human head with a high-resolution 3D finite element model. *Computer Methods in Biomechanics and Biomedical Engineering,* Vol 2, Issue 1 (1999) 49–64

Hartog JPD, 1952, Advanced Strength of Materials. McGraw Hill, USA.

Horgan TJ & Gilchrist, MD., 2003, The creation of three-dimensional finite element models for simulating head impact biomechanics, *International Journal of Crashworthiness*, Vol 8, Issue 4, 353–366.

Horgan TJ & Gilchrist, MD., 2004, Influence of FE model variability in predicting brain motion and intracranial pressure changes in head impact simulations, *International Journal of Crashworthiness*, Vol 9, Issue 4, 401–418.

Jang E.S, 2000, 3D animation coding: its history and framework, in: Proc. IEEE International Conference on Multimedia and Expo, 2000, Vol. 2, 1119–1122.

Kaczmarek, M., Subramaniam, R.P., Neff, S.R., 1997. The hydromechanics of hydrocephalus: steady-state solutions for cylindrical geometry. Bulletin of Mathematical Biology, Vol 59, Issue 2, 295-323.

Kauer M., 2001, Inverse Finite Element Charecterization of Soft Tissues with Aspiration Experiments, PhD dissertation, ETHZ

King AI, Ruan JS, Zhou C, Hardy WN, Khalil TB, 1995, Recent advances in biomechanics of brain injury research: a review. *Journal of Neurotrauma*, Vol. 12, Issue 4, 651-658.

Kleiven, S., 2002. Finite Element Modeling of the Human Head. PhD dissertation, , Department of Aeronautics, Royal Institute of Technology, Stockholm, Sweden.

Kraus G E ,Bailey G J, 1994, Microsurgical Anatomy of the Brain. A Stereo Atlas. Wiliams & Wilkins, Baltimore.

Kriewall TJ, Akkas N, Bylski DI, Melvin JW and Work BA, 1983, Mechanical behavior of fetal dura mater under large axisymmetric inflation, *Journal of Biomechanical Engineering*, Vol. 105, 71-76

Kyriacou, S. K. and Davatzikos, C.A., 1998, A biomechanical model of soft tissue deformation, with applications to non-rigid registration of brain images with tumor pathology, Medical Image Computing and Computer-Assisted Intervention-MICCAI'98, Lecture notes in computer science, Vol. 1496, pp 531-538.

Kyriacou, S., Davatzikos, C., Zinreich, S., Bryan, R., July 1999. Nonlinear elastic registration of brain images with tumor pathology using a biomechanical model. *IEEE Transactions on Medical Imaging*, Vol. 18, Issue 7, 580-592.

Kyriacou, S.K., Mohamed, A., Miller, K. and Neff, S., 2002. Brain Mechanics For Neurosurgery: Modeling Issues., Biomechanics and Modeling in Mechanobiology, 1:2, pp 151-164

Lai-Fook, S.J., Wilson, T.A., Hyatt, R.E., Rodarte, J.R., 1976. Elastic constants of inflated lobes of dog lungs. *Journal of Applied Physiology* Vol. 40, 508–513.

Lawson, CL, 1977, Software for C1 Surface Interpolation, *Mathematical Software III*, 161-194

Lee Y, Terzopoulos D, Waters K., 1995. Realistic modeling for facial animation., Proc. SIGGRAPH'95, Los Angeles, USA, 6– 11 August 1995, 55–62.

Li WD., Lu W.F., Fuh J.Y.H., Wong Y.S., Collaborative computer-aided design: research and development status, Computer-Aided Design 37 (9) (2005), 931–940.

Liseikin, VD., 1999, Grid Generation Methods Springer, Berlin.

Liu B, Zhang L and Gao H, 2006, Poisson ratio can play a crucial role in mechanical properties of biocomposites, *Mechanics of Materials*, In Press, Corrected Proof, Available online at http://www.sciencedirect.com from 23 March 2006.

Liu Z, Bilston L, 2000, On the viscoelastic character of liver tissue: experiments and modeling of the linear behavior. Biorheology; Vol. 37,191–201.

Liu Z, Bilston L, 2002, Large deformation shear properties of liver tissue, Biorheology; Vol. 39, 735–742.

Lo, SH, 1991, Volume Discretization into Tetrahedra - II. 3D Triangulation by Advancing Front Approach, *Computers and Structures*, Vol. 39, Issue 5, 501-511

Lohner, R., 1996, Progress in Grid Generation via the Advancing Front Technique, Engineering with Computers, Vol. 12, 186-210

Manduca A., Oliphant TE, Dresner M.A, Mahowald JL, Kruse SA., Amromin E.; Felmlee, JP., Greenleaf, JF.; Ehman, R.L., 2001, Magnetic resonance elastography: non-invasive mapping of tissue elasticity. *Journal of Medical Image Analysis*, Vol. 5, Issue 4, 237-54

Margulies SS, 1987, *Biomechanics of traumatic coma in primate*, PhD dissertation, University of Pennsylvania, USA

Maurel W., Wu Y., Thalmann N. M. T. D, Biomechanical Models for Soft Tissue Simulation. Springer, Berlin, 1998.

Maurer, C.R., Jr, D.L.G.Hill, A.J.Martin, H Liu, M. McCue, D.R. Rueckert, D.Lloret, W.A. Hall, D.J. Hawkes, C.L.Truwit, 1998. Investigation of intraoperative brain deformation using a 1.5T interventional MR system: Preliminary Results. *IEEE Transactions on Medical Imaging*, Vol. 17, Issue 5, 817-825.

McElhaney JH, Fogle JL, Melvin JW, Haynes RR, Roberts V.L, Alem N.M, 1970. Mechanical properties of cranial bone, *Journal of Biomechanics*. Vol 3, 495 -511.

McElhaney JH., Roberts, VL., Hilyard, JF. 1976. Properties of human tissues and components: nervous tissues. In Handbook of human tolerance, Automobile Research Institute Inc., Tokyo, Japan, p. 143.

McMinn RMH, Hutchings RT and Logan B, 1994, Color Atlas of Head and Neck Anatomy, Mosby; 2nd Rev Ed edition.

Melvin JW., 1970. Development of a Mechanical Model of the Human Head Determination of Tissue Properties and Synthetic Substitute Materials. 14th Stapp Car Crash Conf, Society of Automotive Engineers, SAE Paper No. 700903.

Mendis K, 1992, Finite Element Modeling of the Brain to Establish Diffuse Axonal Injury Criteria, PhD dissertation, The Ohio State University.

Mendis, KK., Stainaker, R. L.; and Advani, S. H.; 1995, A Constitutive Relationship for Large Deformation Finite Element Modeling of Brain Tissue, *Journal of Biomedical Engineering*, Vol. 117, pp 279-285.

Metaxas DN., 1997, Physics-based deformable models. Kluwer Academic Publishers, Boston.

Metaxas D., 1997. Physics-Based Deformable Models: Applications to Computer Vision, Graphics and Medical Imaging. Kluwer Academic Publishers.

Metz H., McElhaney, J., Ommaya, A.K., 1970. A comparison of the elasticity of live, dead, and "fixed brain tissue. *Journal of Bio-mechanics,* Vol. 3, 453-458

Miga MI, Paulsen KD, Kennedy FE, Hoopes PJ, Hartov A, Roberts DW, 1998, Modeling surgical loads to account for subsurface tissue deformation during stereotactic neurosurgery. *IEEE SPIE Proceedings of laser-tissue interaction* IX, Part B: Soft tissue modeling 3254, 501-11

Miga, M. I., Sinha, T. K., Cash, D. M., Galloway, R. L. and Weil, R. J., 2003, Cortical surface registration for image-guided neurosurgery using laser-range scanning. *IEEE Transactions on Medical Imaging*, Vol. 22, 973-985

Miga, M., Paulsen, K., F.E., K., Hartov, A., Roberts, D., 1999a. Modelupdated image-guided neurosurgery using the finite element method: Incorporation of the falx cerebri. In: Taylor, C., Colchester, A. (Eds.), MICCAI 99: Second International Conference on Medical Image Computing and Computer-Assisted Intervention; October 1999; Cambridge, England. Springer.

Miga, M., Paulsen, K., Hoopes, P., Kennedy, F., Hartov, A., Roberts, D., February 2000a. In vivo quantication of a homogeneous brain deformation model for updating preoperative images during surgery. *IEEE Transactions on Medical Imaging*, Vol.47, Issue 2, 266-273.

Miga,M., Paulsen K., Lemery J., Eisner SD., Hartov A., Kennedy F., Roberts, D., October 1999b. Model-updated image guidance: Initial clinical experiences with gravity-induced brain deformation. *IEEE Transactions on Medical Imaging*, Vol. 18, Issue 10, 866-874.

Miga M, Staubert A., Paulsen K., Kennedy F., Tronnier V., Roberts D., Hartov A., Platenik, L., Lunn, K., 2000b. Model-Updated Image- Guided Neurosurgery : Preliminary Analysis Using Intraoperative MRI. In: S.L. Delp, D. G. A., Jaramaz, B. (Eds.), MICCAI 2000: Third International Conference on Medical Robotics, Imaging And Computer Assisted Surgery; 2000 Oct 11{14; Pittsburgh, USA. Springer Verlag.

Miller K, 2005b, Method of testing very soft biological tissues in compression, Journal of Biomechanics, Vol. 38, 153–158.

Miller K, Taylor Z, Nowinski W. L., 2005a, Towards computing brain deformations for diagnosis, prognosis and neurosurgical simulation. *Journal of Mechanics and Medicine and Biology*, Vol. 5, Issue 1, 105–121.

Miller K, 1999. Constitutive model of brain tissue suitable for finite element analysis of surgical procedures. *Journal of Biomechanics* 32, 531- 537.

Miller K, 2002a, Biomechanics of Brain for Computer Integrated Surgery. Warsaw: Publishing House of Warsaw University of Technology

Miller, K., Chinzei, K., 2002b, Mechanical properties of brain tissue in tension. *Journal of Biomechanics*, Vol. 35, Issue 4, 483–490.

Miller K., Chinzei K., Orssengo G and Bednardz B, 2000. Mechanical properties of Brain tissue in vivo: Experiment and computer simulation. *Journal of Biomechanics* Vol. 33, Issue 11, 1369- 1376.

Miller K., Reassessment of brain elasticity for analysis of biomechanisms of hydrocephalus, Journal of Biomechanics, Vol 37 Issue 8, 2004, pp 1263-1269.

Moes N, Dolbow J, Belytschko T. 1999, A finite element method, for crack growth without remeshing. *International Journal for Numerical Methods in Engineering*, Vol. 46, 131–150.

Montemurro DG and Bruni JE, 1981, The Human Brain in Dissection, Oxford University Press, USA

Nabavi A, Black P., Gering D., Westin C., Mehta V., Pergolizzi R., Ferrant M., Wareld, S., Hata, N., Schwartz, R., Wells, W., Kikinis, R., Jolesz, F., April 2001. Serial intraoperative mr imaging of brain shift. Neurosurgery 48, 787{798, to appear.

Nagashima T, Tada Y, Hamano S, Skakakura M, Masaoka K, Tamaki N, Matsumoto S., 1990; The finite element analysis of brain oedema associated with intracranial meningiomas., Acta Neurochir Suppl (Wien)., 51:155-7.

Nagashima T, Tamaki N, Matsumoto S, Horwitz B, Seguchi Y., 1987, Biomechanics of hydrocephalus: a new theoretical model., Journal of Neurosurgery, Vol. 21, Issue 6, 898-904.

Nagashima T., Skirakuni, T., Rapoport, S.T., 1990. A two-dimensional, finite element analysis of vasogenic endema. Neurologica Medica Chirugica 30, 1-9.

Nagashima T., Tamaki N., Matsumoto S., Horwitz, B., Seguchi, Y. 1987 Biomechanics of hydrocephalus: a new theoretical model. Neurosurgery 21 (6), 898–904.

Nasseri S., Bilston L., Tanner R., 2003. Lubricating squeezing flow: a useful method for measuring the viscoelastic properties of soft tissues. Biorheology, Vol. 40, 545–551.

Netter F H, 1991 The CIBA Collection of Medical Illustrations. Vol. 1 Nervous System. CIBA

Nielson, G. M., Hamann, B., 1991. The asymptotic decider : Resolving the ambiguity in marching cubes. In: Visualization '91. IEEE.

Nowinski WL, 1998a, Brain atlas: geometrical models. Thieme, New York/KRDL, Singapore (BAGM specification is available from www.cerefy.com)

Nowinski WL, 1998c, Anatomical targeting in functional neurosurgery by the simultaneous use of multiple Schaltenbrand-Wahren brain atlas microseries. Stereotactic and Functional Neurosurgery,71, 103-116.

Nowinski WL, 2001b, Modified Talairach Landmarks, *Acta. Neurochirurgica*, Vol. 143, Issue 10, 1045-1057.

Nowinski WL, 2001c, Computerized brain atlases for surgery of movement disorders. Seminars in Neurosurgery, Vol. 12, Issue 2, 183-194.

Nowinski WL, 2002a, Electronic brain atlases: features and applications. In: 3D Image Processing: Techniques and Clinical Applications (eds. Caramella D., Bartolozzi C.). Medical Radiology series, Springer-Verlag,:79-93.

Nowinski WL, 2002b, Computer-aided brain surgery: present and future. In: 3D Image Processing: Techniques and Clinical Applications (eds. Caramella D, Bartolozzi C). Medical Radiology series Springer-Verlag, 299-309

Nowinski WL, 2003a, From research to clinical practice: a Cerefy brain atlas story; International Congress Series, 1256, CARS2003, 75-81

Nowinski WL, 2004, Thirunavuukarasuu A., The Cerefy Clinical Brain Atlas (on CD ROM), Thieme Medical Publishers, Inc, (EBAL specification is available from www.cerefy.com)

Nowinski WL, A Thirunavuukarasuu, Volkau I, Baimuratov R, Hu Q, Aziz A, Huang S, 2005, Three-dimensional brain atlas of anatomy and vasculature. Radiographics, Vol. 25, 263-271.

Nowinski WL, Belov D, 2003b, The Cerefy Neuroradiology Atlas: A Talairach-Tournoux atlas-based tool for analysis of neuroimages. Neuroimage, Vol. 20, Issue 1, 50-57

Nowinski WL, Belov D, 2005, Toward Atlas-Assisted Automatic Interpretation of MRI Morphological Brain Scans in the Presence of Tumor, Academic Radiology, Vol. 12, Issue 8, 1049-1057

Nowinski WL, Belov D, Benabid AL, 2003c, An algorithm for rapid calculation of a probabilistic functional atlas of subcortical structures from electrophysiological data collected during functional neurosurgery procedures. Journal of NeuroImage, Vol. 18, Issue 1, 143-155.

Nowinski WL, Benabid AL, 2001a, New directions in atlas-assisted stereotactic functional neurosurgery. In: Advanced Techniques in Image-Guided Brain and Spine Surgery (ed Germano IM), Thieme, New York.

Nowinski WL, Bryan RN, Raghavan R, 1997 The electronic clinical brain atlas: Multiplaner navigation of the human brain, Thieme, New York, Stuttgart.

Nowinski WL, Bryan RN, Thirunavuukarasuu A, 2001b Cerefy student brain atlas. KRDL, Singapore

Nowinski WL, Thirunavuukarasuu A, 1998b Electronic brain atlas library. Thieme, New York/KRDL, Singapore (EBAL speci. cation is available from www.cerefy.com)

Ommaya AK, 1968, Mechanical properties of tissues of the nervous system, *Journal of Biomechanics*, 1:127-138.

Ono M, Kubik S, 1990, Abernathey CD: Atlas of the Cerebral Sulci. Georg Thieme Verlag/Thieme Medical Publishers, Stuttgart - New York.

Ottosen NS, Petersson (eds.), 1992, *Introduction to the Finite Element Method*, Prentice Hall, Europe.

Owen, S., 1998. A survey of unstructured mesh generation technology. Tech. rep., Department of Civil and Environmental Engineering, Carnegie Mellon University, Pittsburgh, PA15213 - USA, http://www.andrew.cmu.edu/user/sowen/survey/index.html

Ozawa, H., Matsumoto, T., Ohashi, T., Sato, M., Kokubun, S., 2001., Comparison of spinal cord gray matter and white matter softness: measurement by pipette aspiration method. Journal of Neurosurgery, 95 (2), 221–224.

Ozkaya N and Nordin M., 1999, Fundamentals of Biomechanics. Springer, Berlin.

Pamidi M. R. and Advani S. H. , 1978, Nonlinear constitutive Relations for Human brain Tissue, Trans. ASME, *Journal of Biomechanical Engineering*, Vol 100, 44-48.

Papademetris, X., Shi, P., Dione, D., Sinusas, A., Constable, R., Duncan, J., 1999a. Recovery of soft tissue object deformation from 3d image sequences using biomechanical models. Tech. rep., Image Processing and Analysis Laboratory, Yale University, New Haven, CT.

Papademetris, X., Sinusas, A., Dione, D., Duncan, J., September 1999b. 3D Cardiac Deformation from Ultrasound Images. In: MICCAI 99: Second International Conference on Medical Image Computing and Computer- Assisted Intervention; October 1999; Cambridge, England. Springer.

Park, J., Metaxas, D., Axel, L., 1996. Analysis of left ventricular wall motion based on volumetric deformable models and MRI-SPAMM. Medical Image Analysis 1 (1), 53-71.

Parthasarathy, VN, Graichen, C., Hathaway, A., 1993. A comparison of tetrahedron quality measures. Finite Element Analysis and Design 15, 255-261.

Paulsen, K.D., Miga, M., Kennedy, F., Hoopes, P., Hartov, A., Roberts, D., February 1999. A Computational Model for Tracking Subsurface Tissue Deformation During Stereotactic Neurosurgery. IEEE Transactions on Biomedical Engineering, Vol. 46, Issue 2, 213-225.

Pena, A., 1999, Effects of Brain Ventricular Shape on Periventricular Biomechanics: A Finite-element Analysis., Journal of Neurosurgery. Vol. 45, Issue 1, 107-109.

Perez V, 2003, Laminated Reference Guide: A complete, labeled illustrations of the parts of the brain in nine different views and sections, BarCharts Inc., Boca Raton, FL, ISBN: 9781572225176

Prange M.T and Margulies S.S. 2002, Regional, directional and age-dependent properties of brain undergoing large deformation. Trans. ASME, *Journal of Biomechanical Engineering*, Vol, 124, 244-252.

Prange M.T, Meaney D.F, Margulies S.S., 2000. Defining Brain Mechanical Properties: Effects of Region, Direction, and Species, SAE Paper No. 2000-01-SC15, in: 44th Stapp Car Crash Conf., Society of Automotive Engineers.

Prange, M., Margulies, SS., 2002, Regional, directional, and age dependent properties of brain undergoing large deformation, Journal of Biomechanical Engineering, Vol. 124, 244–252.

Robert Schneiders, Mesh generation on the web, www-users.informatik.rwth-aachen.de/~roberts/meshgeneration.html

Rohr K, 1996. Point-based elastic registration of medical image data using approximating thin-plate splines. In Proc. of VBC '96 Conference, volume 1131 of Lecture Notes in Computer Science, pages 297-306, Hamburg, Springer.

Romano N. C., Numamaker J. F. Jr., Brigg R. O, 1997, User Driven Design of a Web-Based Group Support System. System Sciences, 1997, Proc Thirtieth Hwaii International Conference on 2, 366 -375

Roy A, 2005a, *Alo Hate Choliyache A(n)dharer Jatri*, (in Bangla), 2nd ed., Ankur Prakashani, ISBN : 984 464 124 1.

Roy A, Nowinski WL, Tay FEH, 2005b, FEM Analysis of a Detailed Anatomical Human Brain Model According to Cerefy Brain Atlas, Proc. 1st International Conference on Complex Medical Engineering: CME2005, Japan, May 15-18, 947-951.

Roy A, Tay F. E. H, Huang S, Nowinski W.L, 2006c, A Java-based Meshed Atlas Toolkit for Visualization and CAD Collaboration, *Journal of Computerized Medical Imaging and Graphics* (submitted for the publication).

Roy A, Tay F. E. H, Nowinski W.L, 2006b, A Meshed Atlas Visualization Toolkit in a Java-based CAD Platform, *Daffodil International University Journal of Science and Technology* , ISSN 1818-5878, Vol. 1, Issue 1, 11-20.

Roy A, Tay FEH, Nowinski WL, 2004a, An Atlas-Based Approach for Prediction and Analysis of the Brain Deformation, Proc. IASTED International Conference on Biomechanics, Honolulu, Hawaii, USA, 162-166.

Roy A, Tay FEH, Nowinski WL, 2004b, Finite Element Analysis of Brain for Neurosurgical Procedure, Proc. IBEC2004b, 1st International Bioengineering conference, Singapore, 247-250.

Roy A, Tay FEH, Nowinski WL, 2006a, Construction of Physics-Based Atlas and its application in Brain Deformation Analysis, International Mems Conference 2006, May 9–12, Singapore, Singapore Journal of Physics: Conference Series 34, 2006, 752–756.

Roy U., Kodkani SS., 1999, Product modeling within the framework of the World Wide Web, IIE Transactions, Vol. 31, 667–677.

Roy, A, 2000. CyberCAD—A Java™-based Synchronized Collaborative CAD System, Master of Engineering dissertation, National University of Singapore.

Ruan JS, Impact Biomechanics of Head Injury by Mathematical Modeling, 1994, PhD dissertation, Wayne State University, USA

Ruan JS, Khalil T, King AI. 1994, Dynamic response of the human head to impact by three-dimensional finite element analysis. *Journal of Biomechanical Engineering*, Vol. 116, Issue 1, 44-50.

Rueckert, D., L.I.Sonoda, C.Hayes, D.L.G.Hill, M.O.Leach, D.J.Hawkes. 1999. Non-rigid registration using free-form deformations: Application to breast MR images. IEEE Transactions on Medical Imaging, Vol. 18, Issue 8, 712-721

Sahay KB, Mehrotra R, Sachdeva U, and Banerji AK, 1992, Elastome-chanical characterization of brain tissues. *Journal of Biomechanics*, Vol. 25, Issue 3, 319-326.

Sahay, K.B., Mehrotra, R., Sachdeva, U., Banerji, A.K., 1992. Elastomechanical Characterization of Brain Tissues, *Journal of Biomechanics*, Vol. 25, 319–326.

Samani A, Bishop J, Yaffe MJ, Plewes DB. 2001, Biomechanical 3-D finite element modeling of the human breast using MRI data, *IEEE Transaction on Medical Imaging*, Vol. 20, 271–9.

Sarron JC, Blondeau C; Guillaume A, Osmont D, 2000, Identification of linear viscoelastic constitutive models. *Journal of Biomechanics*.

Sarti A, Gori A, and Lamberti C, 1999 A physically based model to simulate maxillo-facial surgery from 3D CT images. Future Generation Computer Systems (FGCS), 15:217-221.

Schaltenbrand G, Wahren W, 1977, Atlas for Stereotaxy of the Human Brain. Georg Thieme Verlag, Stuttgart.

Schettini A. and E. K. Walsh, 1988, Brain tissue elastic behavior and experimental brain compression, Volume 305, Issue 1, 2 July 1984, Pages 141-143.

Schmidlin FR, Schmid P, Kurtyka T, Iselin CE, Graber P, 1996, Force transmission and stress distribution in a computer-simulated model of the kidney: an analysis of the injury mechanisms in renal trauma., Journal of Trauma, Vol. 40, Issue 5, 791-6.

Schnabel JA, Tanner C, Castellano-Smith AD, Degenhard A, Leach MO, Hose DR., 2003, Validation of nonrigid image registration using finite-element methods: application to breast MR images. *IEEE Transactions on Medical Imaging*, Vol. 22, 238–247.

Schneiderman B, Designing the user interface : strategies for effective human-computer-interaction, Reading, MA: Addison-Wesley: 1998

Schneiders, RA, 1996, Grid-Based Algorithm for the Generation of Hexahedral Element Meshes, *Engineering With Computers*, Vol. 12, 168-177

Schwartz, J-M, Denningger M, Rancourt D, Moisan C, Laurendeau, D., 2005, Modelling liver tissue properties using a nonlinear visco-elastic model for surgery simulation, Medical Image Analysis, Vol. 9, 103-112

Shephard, MS and Marcel KG, 1991, Three-Dimensional Mesh Generation by Finite Octree Technique, *International Journal for Numerical Methods in Engineering*, Vol. 32, 709-749

Shuck, L.Z., Advani, S.H., 1972. Rheological response of human brain tissue in shear. J. Basic Engineering, Trans. ASME, Dec., pp. 905-911.

Skrinjar, O., C. Studholme, A. Nabavi, and J. S. Duncan. 2001, Steps Toward a Stereo-Camera-Guided Biomechanical Model for Brain Shift Compensation. In Information Processing in Medical Imaging (IPMI 2001), Davis, CA, USA, pages 183–189, 2001.

Skrinjar, O., Duncan, J., 1999. Real time 3d brain shift compensation. In: A. Kuba, M. Smal, A. T.-P. (Ed.), IPMI '99 : 16th International Conference on Information Processing in Medical Imaging. Vol. 1613. Springer.

Stalnaker, R.L., 1969, Mechanical properties of the head, Ph.D. dissertation, West Virginia University.

Steve Owen, Meshing Research Corner, Online resource www.andrew.cmu.edu/user/sowen/mesh.html

Su H, Lin C, Aziz A, Ivanov N, Nowinski WL, 2004, Multiplanar Editor for Segmentation of Three Dimensional Objects on Radiology Images, RSNA 2004, http://rsna2004.rsna.org/rsna2004/V2004/conference/event_display.cfm?id=66601&p_navID=272&em_id=4412841

Subramaniam, R. P.; Neff, S. R. and Rahulkumar, P. A, 1995, numerical study of the biomechanics of structural neurologic diseases, in Proc. High Performance Computing-Grand Challenges in Computer Simulation Society for Computer Simulations, A. Tentner, Ed., San Diego, CA, pp. 552--560.

Sullivan JM. Jr. 1997, A Three Dimensional Mesh Generator for Arbitrary Multiple Material Domains, Journal of Finite Element Analysis and Design, Vol. 25, Issue 2, pp.219-241

Szikla G, Bouvier G, Hori T, Petrov V, 1977, Angiography of the Human Brain Cortex: Atlas of Vascular Patterns and Stereotactic Localization. Springer-Verlag, Berlin.

Tada Y, Nagashima T, and Takada M, 1994, Biomechanics of Brain Tissue (Simulation of Cerebrospinal Fluid Flow). *JSME International Journa*l, Series A (Mechanics and Material Engineering), Vol. 37, Issue 2, 188-194.

Takizawa H, Sugiura K, Baba M, Miller JD., 1994, Analysis of intracerebral hematoma shapes by numerical computer simulation using the finite element method., Neurol Med Chir (Tokyo), Vol 34, Issue 2, pp 65-69.

Talairach J, Tournoux P, 1993, Referentially Oriented Cerebral MRI Anatomy. Atlas of Stereotaxic Anatomical Correlations for Gray and White Matter. Georg Thieme Verlag/Thieme Medical Publishers, Stuttgart - New York.

Talairach J, Tournoux P,1988, Co-Planar Stereotactic Atlas of the Human Brain, Georg Thieme Verlag/Thieme Medical Publishers, Stuttgart - New York.

Tautges, TJ., Blacker T and Mitchell S, 1996, The Whisker-Weaving Algorithm: A Connectivity Based Method for Constructing All-Hexahedral Finite Element Meshes, *International Journal for Numerical Methods in Engineering*, Vol. 39, 3327-3349

Tay, EHF and A. Roy, CyberCAD, October 2003.: A collaborative approach in 3D-CAD technology in a multimedia-supported environment, *International Journal of Computers in Industry*, Volume 52, Issue 2, Pages 127-145

Tay, EHF and A. Roy, 2000, An Intelligent triangular Algorithm for the Development of Web-based CAD. The International Conference of Manufacturing ICM2000, 24 – 26 February, Bangladesh.

Tay, F. E .H and A. Roy. 2000, 3D Solid Modelling Techniques using CyberCAD for Web-based CAD Application. Proc. 5th International Conference on Computer Integrated Manufacturing, 28 –30 March, Singapore.

Tenti, G. , Drake, J. M., Sivaloganathan, S., 2000, Brain biomechanics: mathematical modeling of hydrocephalus, Neurological Research 22: 19-24.

Terzaghi K., 1942, Theoretical soil mechanics. New York, Wiley.

Terzopoulos D., Platt J., Barr A., Fleischer, K., 1987. Elastically deformable models. In Proceedings of SIGGRAPH '87, Anaheim, USA, 27–31, 205–214.

Thibault K., and Margulies S., 1998, Age-Dependent Material Properties of the Porcine Cerebrum: Effect on Pediatric Inertial Head Injury Criteria, *Journal of Biomechanics*, Vol. 31, 1119–1126.

Thompson, JF, Bharat KS, Nigel P. Weatherill Eds., 1999, Handbook of Grid Generation, CRC Press.

Thompson, P., Toga, A., 1996. A Surface-Based Technique for Warping Three-Dimensional Images of the Brain. *IEEE Transactions on Medical Imaging,* Vol. 15, Issue 4, 402-417.

Ting, T., 1996. Anisotropic elasticity: theory and Applications. Oxford University Press.

Truex, RC, and Kellner, 1948, CE, Detailed Atlas of the Head and Neck, Oxford University Press, New York, USA.

Trusdell, C., and Noll, W., 1965, The nonlinear field theories of mechanics, Encyclopedia of Physics, Vol. 3, Springer Verlag, New York.

Vannah, W.M, Childress, D.S., 1996. Indentor tests and finite element modeling of bulk muscular tissue in vivo. Journal of Rehabilitation Research and Development, Vol. 33, 239–252.

Vigneron LM, Verly JG, Warfield SK, 2004, Modeling surgical cuts, retractions, and resections via extended finite element method. In: Proceedings of Medical Image Computing And Computer-Assisted Intervention (MICCAI), vol. 2, 311–318.

Voo, L., Kumaresan, S., Pintar, F. A., Yoganandan, N., Sances, Jr. A., 1996, Finite-element models of the human head, *Medical Biology in Engineering and Computers*, Vol 34, 375-381.

Walsh, E., Schettini, A., 1984. Calculation of brain elastic parameters in vivo. American journal of physiology, 274:693-700.

Walsh, E., Schettini, A., 1990. Brain tissue elasticity and CSF elastance. Neurolog. Research 12, 123-127.

Wang, H.C.; Wineman A.S.; 1972, A mathematical model for the determination of viscoelastic behavior of brain in vivo. II. Relaxation response, *Journal of Biomechanical Engineering*, Vol 5, Issue 2, 571-80.

Wang, H., Ateshian, G.A., 1997. The normal stress effect and equilibrium friction coefficient of articular cartilage under steady frictional shear. *Journal of Biomechanics* Vol. 30, Issue 8, 771–776.

Wang, Y., Staib, L., 2000. Physical model-based non-rigid registration incorporating statistical shape information. Medical Image Analysis 4, 7- 20.

Warfield, S. K., Talos, F., Tei, A., Bharatha, A., Nabavi, A., Ferrant, M., Black, P. McL., Jolesz, FA. and Kikinis, R, 2002, Real-time registration of volumetric brain MRI by biomechanical simulation of deformation during image guided surgery. Computing and Visualization in Science, Vol. 5, 3-11

Warrick PA, Funnell WRJ, VRML: 1996, A tool for visualizing anatomy in medical education, Proc. 22nd Can. Med. & Biol. Eng. Conf., Charlottetown, 18-19

Wittek A, Miller K, Kikinis R, Warfield SK, 2006, Patient-Specific Model Of Brain Deformation: Application To Medical Image Registration, *Journal of Biomechanics*, In Press, Corrected Proof, Available online (http://www.sciencedirect.com).

Wittek A, Miller K, Laporte J, Warfield S, Kikinis R, 2004, Computing reaction forces on surgical tools for robotic neurosurgery and surgical simulation. Presented at Australasian Conference on Robotics and Automation ACRA, Canberra, Australia.

Wu, JZ., Dong, R.G., Schopper, A.W., Analysis of effects of friction on the deformation behavior of soft tissues in unconfined compression tests. *Journal of Biomechanics*, Vol 37, Issue 1, 2004, 147–155.

Xu MH, Nowinski WL, 2001, Talairach-Tournoux brain atlas registration using a metalforming principle-based finite element method. Journal of Medical Image Analysis; Vol. 5, 271–279.

Yeo TT, Nowinski WL, 1997, Functional neurosurgery aided by use of an electronic brain atlas. Acta Neurochirurgica, Suppl 68:93-99. (Also in: Ostertag et al. (eds.) Advances in Functional and Stereotactic Neurosurgery 12).

Yerry, MA and Shephard MS, 1984, Three-Dimensional Mesh Generation by Modified Octree Technique, *International Journal for Numerical Methods in Engineering*, Vol. 20, 1965-1990

Zahavi E and Barlam D, 2000, Nonlinear Problems in Machine Design, CRC Press, LLC.

Zahavi E, The Finite element method in Machine Design, 1993, A Solomon Pres Book, Prentice Hall, Englewood Cliffs.

Zhivoderov NN, Zavalishin NN, Neniukov AK. 1983, Mechanical properties of the dura mater of the human brain, *Sud Med Ekspert,* Vol. 26, Issue 1, 36-37.

Zhou C, Finite Element Modeling of Impact Response of an Inhomogeneous Brain, 1995, PhD dissertation, Wayne State University, USA

Zhou, C., Khalil, T. B., and King, A. I., 1996. Viscoelastic response of the human brain to sagittal and lateral rotational acceleration by finite element analysis. In Proceedings of the International IRCOBI Conference on the Biomechanics of Impacts, 35-48. Bron: International Research Committee on Biomechanics of Impact.

Zienkiewicz, O., Taylor R., 1987. *The Finite Element Method*, 4th Edition. McGraw Hill Book Co., New York

APPENDICES

Appendix I. PBA: The Color Code, Number of Nodes and Elements

The 43 subcortical structures have been successfully meshed for proposed Physics-based atlas (PBA). The RGB code, node and element numbers of the individual structures are enlisted below:

Structure Name	Surface Mesh		Volumetric Mesh		RGB (decimal)		
	No of Triangles	No of Vertex	No of Element	No of nodes			
Corpus callosum	14336	7170	9492	15927	130	75	130
Corpus geniculatum laterale	700	354	8088	14203	90	81	76
Corpus geniculatum mediale	580	294	8219	14540	86	42	54
Corpus mamillaris	324	164	8486	15289	100	100	200
Cortical areas	10232	5119	2672	5867	0	49	134
Cuneus	358	184	8449	15177	126	0	255
Fornix	250	130	8554	15494	17	73	219
Globus pallidus lateralis	3448	1728	4510	8072	0	161	91
Globus pallidus medialis	1672	840	6248	10167	0	200	91
Hippocampal gyrus	315	162	8491	15303	182	171	154
Hippocampus	3976	1992	4998	8211	179	147	179
Hypothalamus: POL	572	290	8228	14562	198	185	160
Hypothalamus: SO	580	296	8215	14528	69	61	59
Hypothalamus: VM	288	148	8518	15383	80	249	80
Hypothalamus: LAT	484	246	8320	14813	149	24	149
Inferior frontal gyrus	453	232	8352	14901	0	255	126
Inferior occipital gyrus	320	164	8486	15288	63	63	63
Inferior temporal	312	160	8494	15311	214	189	148
Insula	356	182	8451	15183	239	206	90
Lingual gyrus	483	246	8321	14815	249	119	0
Medial frontal gyrus	421	215	8385	14994	226	175	0
Middle frontal gyrus	330	169	8476	15259	105	77	89
Middle occipital gyrus	310	159	8496	15317	184	38	131
Middle temporal guyrus	455	232	8350	14896	17	12	242
Nucleus accumbens septi	484	246	8320	14812	80	131	80
Nucleus caudate	10844	5426	4079	7443	255	239	0
Nucleus ruber (bottom)	856	430	7916	13785	186	58	77
Nucleus ruber (top)	540	274	8262	14653	154	89	107
Nucleus subthalami	856	432	7911	13774	0	103	174
Putamen	6736	3372	1586	4705	0	135	91
Substantia nigra	1268	638	8468	13696	0	0	255
Thalamus: Others	3712	1862	4169	7635	223	112	151
Thalamus: Anterior	1080	544	7645	13175	214	51	86
Thalamus: Centromedianum	768	388	8012	14015	151	93	131

Structure Name	Surface Mesh		Volumetric Mesh		RGB (decimal)		
	No of Triangles	No of Vertex	No of Element	No of nodes			
Thalamus: Dorso medial	1996	1000	6467	10944	198	73	117
Thalamus: Lateral dorsal	512	260	8291	14733	131	31	63
Thalamus: Lateral posterior	1128	568	7587	13049	207	43	100
Thalamus: Pulvinar	3964	1986	3865	7257	189	93	154
Thalamus: Ventral anterior	968	488	7780	13472	228	24	253
Thalamus: Ventral lateral	2448	1228	5848	9953	161	63	126
Thalamus: Ventral posterior lateral	1380	694	7272	12405	195	207	49
Thalamus: Ventral posteromedial	816	412	7957	13883	172	38	86
Ventriculus	13448	6728	9215	18256	200	0	0
White matter	24532	12268	9413	22442	219	193	161

Appendix II. Virtual Design Studio: Collaboration in MAVT

A. Use of RMI in MAVT for Collaboration

The networking function in the module of MAVT has been implemented using Java™ Distributed Object Architectures-RMI. RMI is an object-oriented implementation for distributed Java™ applications. It enables an application to call procedures that exist on another machine. This system is a network abstraction that gives the impression that one is calling standard procedures in a local application. In a RMI system, the client interacts with a remote object through a defined interface. This has been implemented in a specific module of MAVT to develop virtual design studio (VDS). Collaboration has been created to contain all socket classes implementation.

The MAVT RMI server and client are constructed inside the MAVT Network package with the necessary functionality. A naming service, the RMI Registry, is provided to connect the MAVT server and the MAVT client together using a URL-style of names (such as rmi://host.port/name) A MAVT client asks for the remote objects and the MAVT server returns the stub objects to the MAVT client. The MAVT system will

use the rmic compiler to generate the matching stub and skeleton classes for a certain remote object.

With RMI, an object, B, residing on the MAVT server may be manipulated by another object, A, on a remote machine, which is a MAVT client. Object B does not really exist on the MAVT server, rather an alternative object is used as a kind of virtual object. This stub- or proxy-object provides the same interface as the real object B, but under the covers it uses the RMI services to pass method requests over the network to the real object B. Object A therefore does not need to know whether object B is local or remote as denoted in above Fig A-1.

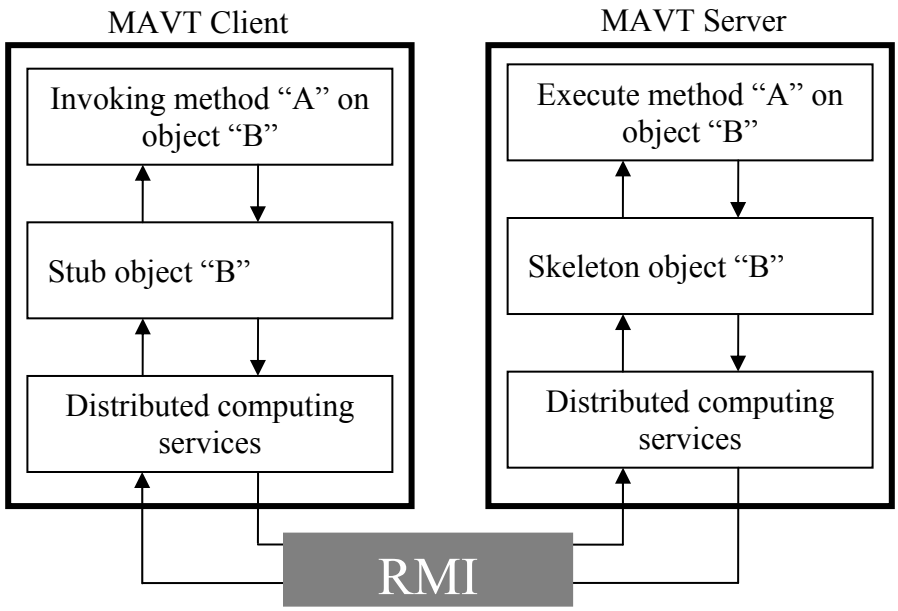

Figure A-1. Method invoking with RMI between MAVT server and MAVT client.

If another object, C, needs to be passed between the MAVT client and the MAVT server (for instance as a parameter for a method), RMI uses a technique called object serialization to "flatten" the object, turning it into a stream of bytes. These are sent to

the RMI system on the remote machine, which rebuilds the object C and passes it into the method call. Return values from methods are handled in the same way. With this method, 3D object data in MAVT can be transferred over the Internet to other remote machines with subsequent rebuilding of the object in the local side for rendering and displaying as well as modification.

B. CAD Data Transferring Over the Internet in MAVT

In MAVT, there are three methods to transfer 3D object data across the Internet. They are instruction transferring, middle-layer geometrical data transferring, and serialized objects and files transferring.

To transfer serialized object across the Internet, the most common and standard way is using RMI to transfer data. In MAVT, most objects including the transformation matrix of the *SimulationUniverse* are transferred over the Internet using this method as described in following:

```
...
synchronized public void broadcastTransform(ClientInterface
sendingClient, SimulationMatrix cm) throws RemoteException{
    for(int i = 0; i <clientVector.size(); i++ ){
      ClientInterface ci = (ClientInterface).elementAt(i);
      if(! ci.getCoworkWindowTitle().equals(
        sendingClient.getCoworkWindowTitle()) ){
        ci.getTransformMatrix(sendingClient, cm);
      }
    }
  }
}
...
```

As shown in the above code segment, the matrix object for *SimulationUniverse* transformation, which is the *SimulationMatrix*, is serialized and transferred over the

Internet to other clients. As a result, the other clients rebuild the *SimulationMatrix* object after obtaining it and use it for its corresponding *SimulationUniverse* transformation in a synchronized way.

C. Collaboration functionality in MAVT

To establish the collaboration in MAVT (through VDS), the MAVT server must be initialized first. The server program is a stand-alone GUI that is independent of the MAVT kernel application. After running the server program, the server GUI will be displayed. The user needs to press "Set up Server" button to initialize the MAVT server. The server application will automatically search the IP address of the machine where the server application resides. In addition, the server starting time will be displayed as well. After the successful initialization of the MAVT RMI server, an indication message will be given upon the finishing of the server initialization. If the initialization is failed due to network malfunction, an error message will be shown on the server main text area as follows:

```
...
StatusArea ta = new StatusArea();
try{
  ta.append("\nTrying to set up RMI server at
  "+MAVT.Network.RMIUtility.IPAddress()+"......");
  serverImplement = new ServerImplement(this);
  Naming.rebind("MAVTRMIServer", serverImplement);

  ta.append("Set up RMI server succeeded!");
  ta.append("The server set up at: " +
  MAVT.Network.RMIUtility.rightNowTime());
  closeButton.setEnabled(true);
  sysAdminButton.setEnabled(true);
  setupButton.setEnabled(false);
}
catch(Exception e){
  ta.append("Exception: "+e+"\n");
  ta.append("Set up RMI server failed!\n");
}
...
```

A GUI-based window is used by observer at the server side during collaboration design. It is also a container that integrates tools needed in collaboration session. It extends the AWT dialog class, and recorded by the MAVT main window. The

fragment of source code is shown below, which include the definition, constructor and main methods of the class, CoWorkWindow.

```
package MAVT.Collaboration; // VDS module.
import java.lang.*;
import java.awt.*;
import java.awt.event.*;
import java.applet.*;


public class CoWorkWindow extends Dialog
{
  Button  bList[] = new Button[6];
  public SimulationUniverse SimulationUniverse;
  MAVTMainWindow mavt_mw;
  public ServerThread serverThread = null;

  public CoWorkWindow(MAVTMainWindow mavt_mw){//constructor
    super(mavt_mw,"Collaborative observer");
    this.mavt_mw = mavt_mw;
    open = true;
    init();
  }
  private void init(){// the GUI of the window, omitted
    SimulationUniverse=new SimulationUniverse(null);
    add("Center", SimulationUniverse);
    addWindowListener(new WndAdapter(this));
  }//end init
}
```

Appendix III. Implementation of Anti-Solid Algorithm (ASA)

To perform solid modeling operation such as cutting hole, subtraction, intersection, union etc. in MAVT, two kinds of objects are created; one is *acting object* called anti-solid, and another is *target object* called solid. Target object information is inherited from previous operation and it is the real result existing in the memory. In contrast, the acting object sometimes does not have the full data information. What Anti-Solid algorithm does is that it fulfils the acting object data information and shifts the position between target object and acting object to obtain the final result. Every surface of original object is taken out to test for intersection with the Anti-Solid; the intersected surface is then calculated to determine the remaining part. Here is a chunk of code of ASA that has successfully been implemented in MAVT:

```
// Take out every surface from solid
SimulationSurface[] ss=solid.getSimulationSurface();
// take out every surface from anti-solid
SimulationSurface[] as=SolidModeller.getAntiSolidSurface(...)
// Intersection test
Vector
pointpair=Plane_IntersectionJudge.Plane_Intersection(Q,P);
...
// Get the result of intersection
surf=buildSimulationSurFaceTempold.buildSimulationSurFaceVect
or(Point);
...
// Get updated surface
SurfaceRep[]  csarr1=combine.combine_HoleInCS();
```

- Every surface of Anti-Solid is taken out to test for intersection with the original object, new surfaces to be added is determined here.

```
// Get the new adding surface
SurfaceRep[] cinter=inter.getIntersectPart();
```

- At the end, the resulting array of surfaces will be reconstructed to build the resulting object.

```
// construct the result object
SimulationSurface[] rs=new SimulationSurface[vrn];
SimulationFreeFormSurface CFS[0]=new
SimulationFreeFormSurface(rfs, cu, app);
SimulationSolid csd=new SimulationSolid(rs, CFS);
cu.Solids.addChild(csd);
```

...

The test of one surface intersecting with the Anti-solid will be performed between the original surface and every surface of Anti-Solid. To do so following steps are followed.

- First at all, one surface of the Anti-Solid is taken out to test whether it is parallel with the original surface. The mathematical representation of these two surfaces will be retrieved from the coordinates of the surface to test for parallelism.

```
// Retrive the equation for the surface fromt the coordinates
EquationofPlane plane1 = new EquationofPlane(p[0],p[1],p[2]);
EquationofPlane plane2 = new EquationofPlane(c[0],c[1],c[2]);
// Test parallel
if (SimulationMath3d.isParallelPlane(plane1,plane2)==true)
...
```

- An infinite intersection line is calculated from the mathematical equation of two surfaces if two surfaces are not parallel to each other.

```
EquationofIntersectionLine IntersectionLine = new
EquationofIntersectionLine(plane1, plane2);
```

- This intersection line is used to get the exact intersection points on the original surface by the line-line intersection method. These intersection points are put in an array for calculation.

```
// Test every edge
for (int i=0; i< (p.length-1); i++)
{
  // Calculate the intersection point
  if ( (x =
MyintersectOfLine_Line(p[i],p[i+1],plane1.VectorofFace,

IntersectionLine.IntersectionofLine,
IntersectionLine.VectorofLine) ) != null)
    ...
    // Test validity of the intersection point
    if (Math.abs((x.distance(p[i])+x.distance(p[i+1])) -
p[i].distance(p[i+1]))<=1.0e-9 ||
                ((x.distance(p[i]) <p[i].distance(p[i+1]))
&&(x.distance(p[i+1]) <p[i].distance(p[i+1]))))
       ...
       // put valid intersection point into result array
       pointpair.addElement(x);
       ...
```

- The above steps are repeated until all the surfaces of the Anti-Solid are tested. The intersection points array is then used to construct the intersection face from the resulting surfaces and solid. If the intersection face is on the same plane as the original surface, a 2D Boolean on the same plane is performed to get the desired surface.

Appendix IV. Loft Overview

The basic model was created in this work using a SolidWorks™ tool called loft. Loft uses cross sections to extrapolate along a curve. It lets user create complex 3D shapes by interpolating multiple 2D cross-sections of various size. Loft connectors define how models profiles align.

Loft creates a feature by making transitions between profiles. A loft can be a base, boss, cut, or surface. It can maintain the connectivity by controlling the tangency at the starting and ending profiles. Fig. A-2 shows a basic illustration of loft.

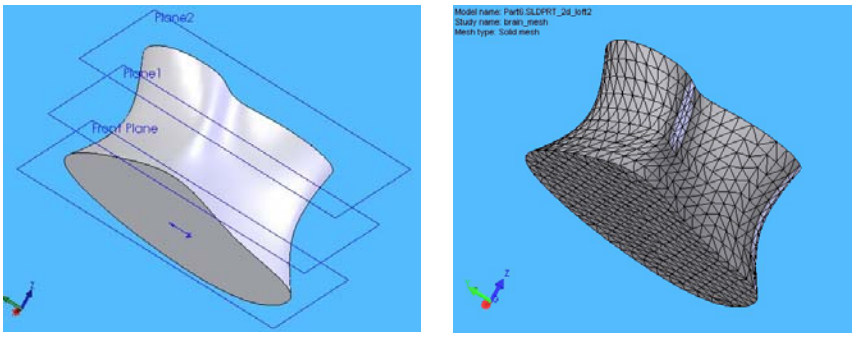

Figure A-2. Illustration of loft: a) three irregular cross sections have been joined through *loft* and b) then meshed.

MAVT module applies a tangency constraint based on a selected entity used as a direction vector. The user has to select the Direction Vector by selecting a plane or a linear edge or axis to define the Direction Vector. It applies a tangency constraint normal to the start or end profile. Here is the chunk of code used by the MAVT module:

```
public class PickSurfaceToLoft extends PickAnySurface
{
  SimulationUniverse cu;
  public PickSurfaceToLoft(SimulationUniverse cu){
  super(cu);
  this.cu=cu;
  System.out.println("Inside PickSurfaceToExtrude
constructor.");
  }

  public void performOperation(SimulationSurface cs){

      Color3f black = new Color3f(0.0f, 0.0f, 0.0f);
      Color3f white = new Color3f(1.0f, 1.0f, 1.0f);

      Appearance app;
      app = ColorTemplate.returnAppearance(new
Material(ColorTemplate.BLACK, ColorTemplate.BLACK,
ColorTemplate.SURFACECOLOR,ColorTemplate.WHITE, 100.0f));

      Point3d[] P=(Point3d[])cs.returnCoordinates();
      int sizep=P.length;
```

```
  Vector VCS=new Vector();
  int times=16;
  Point3d PQT = new Point3d(0.0, 0.0, 0.0);
  Vector3d V=new Vector3d();
  double R[]=new double[sizep];
  double L[]=new double[sizep];
  Point3d Q[]=new Point3d[sizep];
  for (int k=0; k<sizep; k++)
       {
R[k]=P[k].x;
L[k]=Math.sqrt(2*R[k]*R[k]*(1-Math.cos(Math.PI*2/times)));
       }
  for(int t=0; t<times; t++)
       {
  V.x=-Math.sin((Math.PI/times)+(Math.PI*2*t/times));
  V.y=0.0f;
  V.z=-Math.cos((Math.PI/times)+(Math.PI*2*t/times));
  V.normalize();


      for( int k=0; k<sizep; k++)
          {
          Q[k]=new Point3d();

          };

      for (int k=0; k<sizep; k++)
          {

      Q[k].x=P[k].x+L[k]*V.x;
      Q[k].y=P[k].y+L[k]*V.y;
      Q[k].z=P[k].z+L[k]*V.z;

          };
```

Appendix V. Macro to Interact with SolidWorks Interface

SolidWorks (ver. 2005) cannot create a lofted surface or solid from point cloud data stored in a text file directly. After extracting the point clouds from the plates of Cerefy atlas, those were stored in text files. An interface was needed to allow SolidWorks to draw the points, sketches and splines from stored data directly. To provide such facility, a macro (in VB script) is written to interact with SolidWorks interface. The macro allows reading 3D point cloud data from a text file and then automatically placing the points into CAD system. Here is the chunk of code:

```
Public Function CreateSketch(n As String, flat As Boolean) As
SldWorks.sketch
        Set CreateSketch = part.GetActiveSketch

            If flat Then part.InsertSketch
            Else part.Insert3DSketch
            Set CreateSketch = part.GetActiveSketch2
        End If
        If CreateSketch Is Nothing Then
```

```
                Call point_in_SW.SendMsgToUser2("Could not create
        Sketch. Please select a face or plane and retry", 3, 1)
                Else
                    CreateSketch.name = n
                    part.SetAddToDB (True) ' faster, and needed to
        avoid auto constraints
                End If
        End Function


Public Function Spline(c As Collection, name As String) As
SldWorks.feature

    Dim sketches As New Collection
    Dim closed As Boolean

    Dim i As Integer
    For i = 1 To c.Count
        If i = c.Count And IsSame(c(1), c(c.Count)) Then closed =
True
        If closed = False Or i = 1 Then
            Dim sk As SldWorks.sketch
            Set sk = CreateSketch(name + "-" + Str(i), False)
            If sk Is Nothing Then Exit Function
            Call CreateSegment(c(i), UserForm1.Volume)
            part.InsertSketch ' close the sketch
            sketches.Add sk
        End If
    Next i

    Dim g() As Double
    ReDim g(3 * c.Count - 1)
    i = 0
    While IsDegenerate(g) ' skip poles
        Dim j As Integer
        For j = 1 To c.Count ' copy the ith point of each spline in c
            g(j * 3 - 3) = c(j)(i * 3)
            g(j * 3 - 2) = c(j)(i * 3 + 1)
            g(j * 3 - 1) = c(j)(i * 3 + 2)
        Next j
        i = i + 1
    Wend

    Dim guide As SldWorks.sketch
    Set guide = CreateSketch(name + "-guide", False)
    If guide Is Nothing Then Exit Function
    Call part.CreateSpline(g)
    part.InsertSketch ' close the sketch

    part.SetAddToDB (False) ' faster, and needed to avoid auto
constraints
    part.Rebuild 1 ' all

    part.ClearSelection
    Dim s As Variant
    For Each s In sketches
        Call s.Select2(True, 1)
    Next s
    Call guide.Select2(True, 2)

    point_in_SW.AllowFailedFeatureCreation True
    If UserForm1.Volume Then
        Call part.InsertProtrusionBlend4(closed, 0, 0, 1, 0, 0, 0, 0,
0, 0)
    Else
        Call part.InsertSplineRefSurface2(closed, False, False, True,
0, 0)
    End If
```

```
    Dim swSelMgr As SldWorks.SelectionMgr
    Set swSelMgr = part.SelectionManager
    On Error Resume Next
    Set Spline = swSelMgr.GetSelectedObject3(1)
    If Spline.GetErrorCode <> 0 Then ' it did not work
        ' delete everything
        part.DeleteSelection False
        Set Spline = Nothing
        For Each s In sketches
            Call s.Select2(True, 1)
        Next s
        Call guide.Select2(True, 2)
        part.DeleteSelection False
        If c.Count > 2 Then ' try splitting
            Dim c1 As New Collection
            j = (c.Count + 1) / 2
            For i = 1 To j
                c1.Add (c(i))
            Next i
            If Not Spline(c1, name + "/1") Is Nothing Then '2nd half
                Dim c2 As New Collection
                For i = j To c.Count
                    c2.Add (c(i))
                Next i
                Set Spline = Spline(c2, name + "/2")
            End If
        End If
    End If
    point_in_SW.AllowFailedFeatureCreation False
End Function
```

Appendix VI. The meshed structures of PBA

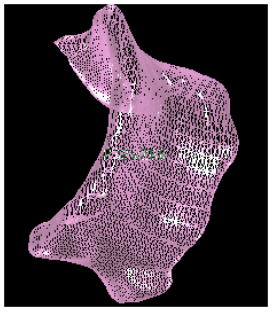

Corpus callosum

Corpus geniculatum laterale

Corpus geniculatum mediale

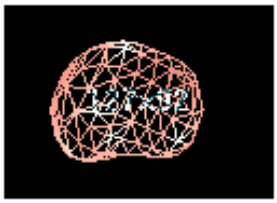

Corpus mamillaris

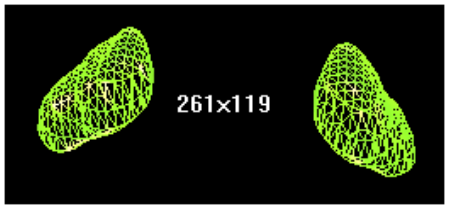

Globus pallidus medialis

Hippocampus

Hypothalamus: POL

Hypothalamus: SO

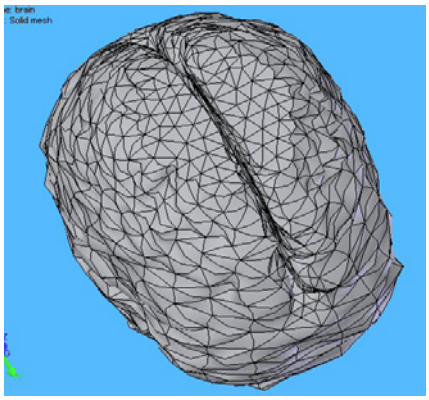

The whole meshed brain

Hypothalamus: LAT

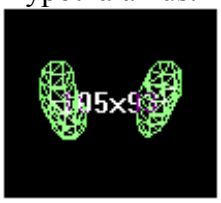

Hypothalamus: VM

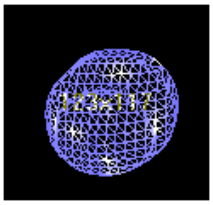

Corpus amygdaloideum

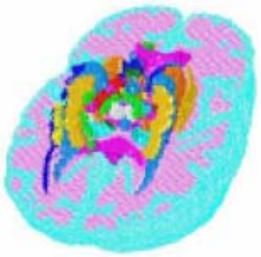

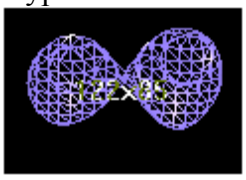

Nucleus rubber: B

Nucleus subthalami

The whole brain with various parts

Nucleus rubber: T

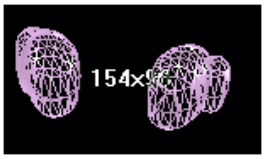

Thalamus: Anterior

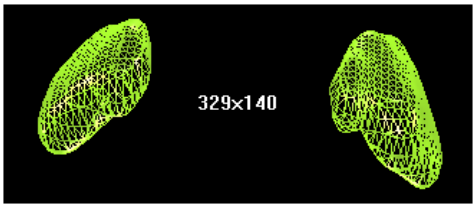

Globus pallidus lateralis

Thalamus: Centromedianum

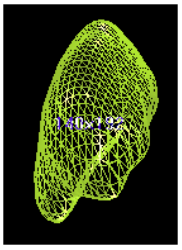

Putamen

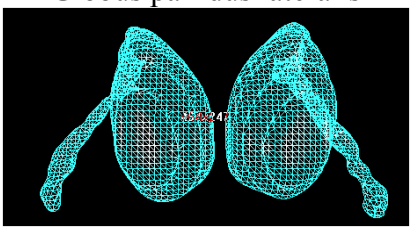

Nucleus caudatus

Thalamus: Lateral posterior

Thalamus: Dorso medial

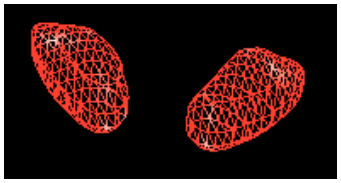

Substantia nigra

Thalamus: Ventral anterior

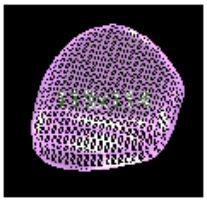

Thalamus: Pulvinar

Thalamus: Lateral dorsal

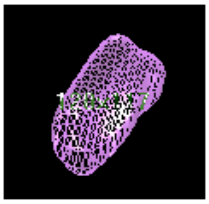

Thalamus: Ventral

Thalamus: Ventral posterior lateral

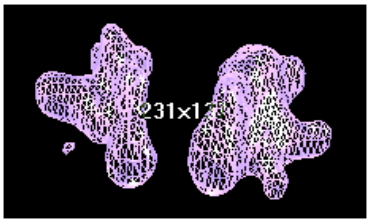

Thalamus: Others

lateral

Thalamus: Ventral posteromedial

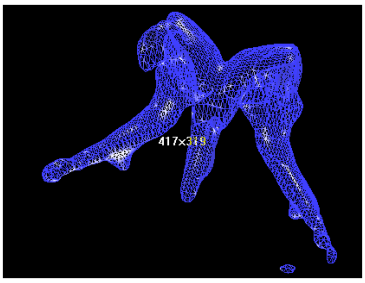

Ventriculus